arXiv:1504.05274v1 [hep-lat] 21 Apr 2015

THERMODYNAMICS OF STRONG-INTERACTION MATTER FROM LATTICE QCD

Heng-Tong Ding

Key Laboratory of Quark & Lepton Physics (MOE), Institute of Particle Physics, Central China Normal University, Wuhan, 430079, China

Frithjof Karsch

Physics Department, Brookhaven National Laboratory, Upton, NY 11973, USA
and
Fakultät für Physik, Universität Bielefeld, D-33615 Bielefeld, Germany

Swagato Mukherjee

Physics Department, Brookhaven National Laboratory, Upton, NY 11973, USA

We review results from lattice QCD calculations on the thermodynamics of strong-interaction matter with emphasis on input these calculations can provide to the exploration of the phase diagram and properties of hot and dense matter created in heavy ion experiments. This review is organized as follows:

1) Introduction
2) QCD thermodynamics on the lattice
3) QCD phase diagram at high temperature
4) Bulk thermodynamics
5) Fluctuations of conserved charges
6) Transport properties
7) Open heavy flavors and heavy quarkonia
8) QCD in external magnetic fields
9) Summary

1. Introduction

It has long been recognized that under extreme conditions of high temperature or densities matter interacting through the strong force – strong-interaction matter – cannot exist in the form of nuclear matter formed from hadrons. The copious production of new resonances[1] and the intrinsic size of the nucleons put a natural

limit on the range of validity of hadron physics.[2,3] In the context of thermodynamics of strong-interaction matter this found its expression in the formulation of the hadron resonance gas model[1,4] which led to the postulate of a limiting temperature – Hagedorn temperature – for the thermodynamics of ordinary nuclear matter.

With the formulation of Quantum Chromodynamics (QCD)[5,6] as the fundamental theory of strong interactions it has soon been realized that matter formed from strongly interacting particles may be converted into a new form of matter[7,8] –the quark-gluon plasma[9] – in which the dominant degrees of freedom are the constituents of hadrons, i.e. quarks and gluons. At low temperatures and densities they are confined in hadrons. However, at high temperature and densities they can move "freely" over macroscopic distances in bulk strong-interaction matter.

It has been speculated that the transition from confined to deconfined matter, like in condensed matter systems, goes along[10] with the restoration of global symmetries of the underlying microscopic theory describing the interaction among constituents of strong-interaction matter, i.e. QCD. The analysis of these symmetries led to the phenomenology of a complex phase structure of strong-interaction matter, leading to homogeneous and inhomogeneous as well as color-superconducting phases. This bears many analogies to phase structures known in condensed matter

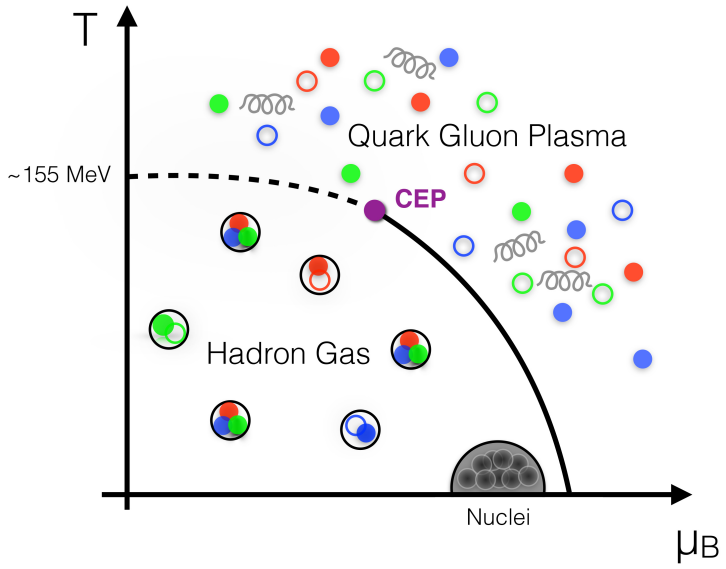


Fig. 1. QCD phase diagram in the temperature (T) and baryon chemical potential (μ_B) plane. At vanishing μ_B lattice QCD calculations show that the transition is not a phase transition but a continuous crossover, reflecting pseudo-critical behavior in the vicinity of the true chiral transition. At $\mu_B > 0$ a second order critical end point (CEP) may exist, which would be followed by a line of first order transitions at larger values of μ_B. Constraints on the location of a CEP will come from lattice QCD calculations.

systems.[11,12] Only little of this complex structure is verified through first principle lattice QCD calculations. In Fig. 1 we show a sketch of the QCD phase diagram that only highlights those aspects that we believe can be addressed at present through lattice QCD calculations. We will discuss the phase diagram in detail in Section 3.

Phase transitions as well as properties of matter close to such transitions arise from complex long range interactions in multi-particle systems on multiple length scales and at the same time often develop simple universal behavior. Their analysis requires non-perturbative techniques. With the formulation of lattice QCD, i.e. the introduction of a discrete space-time lattice as regulator for quantum field theories like QCD[13] a framework for new non-perturbative approaches to the study of strong-interaction matter had been established. It became possible to perform first-principle numerical calculations – lattice QCD simulations[14] – by which a systematic study of the phase structure and basic bulk properties of strong-interaction matter[15–17] could be performed for the first time. We will give a brief introduction to lattice QCD in Section 2. Today these calculations are highly advanced and continuum extrapolated results for the QCD transition temperature and the equation of state exist at vanishing net baryon number density. We will review these results and report on the status of the lattice QCD program that aims at an extension of these calculations to non-zero net baryon number density or equivalently non-zero baryon chemical potential in Section 4.

Properties of strong-interaction matter are studied intensively in large experimental programs at the Relativistic Heavy Ion Collider (RHIC) at Brookhaven National Laboratory (BNL), USA, and the Large Hadron Collider (LHC) as well as the Super Proton Synchrotron (SPS) at the European Research Center (CERN). Experiments at these accelerators are devoted to the exploration of the properties of hot and dense matter created in collisions of ultra-relativistic heavy ions. Through the variation of beam energies at RHIC, i.e. the beam energy scan (BES), it also became possible to explore systematically the phase structure of strong-interaction matter at non-zero net baryon number density. This allows to search systematically for the chiral critical point or critical end point (CEP) in the QCD phase diagram. The CEP is a postulated second order phase transition point which is expected to mark the endpoint of a line of first order phase transitions that separates the low temperature, low density hadronic phase from a low temperature, large baryon number quark-gluon plasma phase (also the existence of this first order line at present is not confirmed through lattice QCD calculations). The existence of a CEP in the QCD phase diagram is imprinted in the properties of fluctuations of conserved charges, e.g. net baryon number, electric charge or strangeness fluctuations. These conserved charge fluctuations can be calculated in lattice QCD at vanishing baryon chemical potential and the calculations can be extended to non-zero values of the chemical potential using Taylor expansions of thermodynamic observables. They can directly be compared to experimental measurements of conserved charge fluctuations performed at the LHC and the BES at RHIC and may provide insight into

the existence and location of a CEP in the QCD phase diagram. We will report in Section 5 on the status of lattice QCD calculations of conserved charge fluctuations and their usage to analyze freeze-out conditions in heavy ion experiments.

Heavy ion experiments at RHIC provided striking evidence for the highly correlated, non-perturbative structure of strong-interaction matter in the high temperature phase. In particular, the observation of strong elliptic flow and very efficient energy loss of high momentum quarks traversing through the medium (jet quenching) paved the way for a picture of a strongly interacting medium that has been called an 'almost perfect liquid'. These measurements suggest that strong-interaction matter at temperatures close to but above the transition temperature has quite unique transport properties, (i) a small shear viscosity to entropy ratio that may be close to the conformal limit value $\eta/s = 1/4\pi$ calculated in conformal field theories (AdS/CFT limit), (ii) a large bulk viscosity that may diverge in the massless QCD limit at the chiral phase transition temperature, (iii) small electrical conductivity and diffusion coefficients. These transport properties can systematically be analyzed in lattice QCD, although this requires the reconstruction of continuous spectral functions from a finite set of observables, which is in general an ill-posed problem. The calculation of transport properties in lattice QCD will provide crucial input to the modeling of the hydrodynamic expansion of hot and dense matter formed in heavy ion collisions. Spectral functions also carry information on in-medium modifications of hadrons. The dissociation of heavy quark bound states has long been advocated as one of the striking signatures for the formation of a deconfined color screened medium[18] while the melting of light quark bound states is intimately related with the restoration of chiral symmetry.[19] We will report on the status of calculations of transport coefficients and in-medium hadron properties in Sections 6 and 7.

Finally, in Section 8 we will briefly review a relatively new but very exciting field of QCD thermodynamics that addresses the behavior of strong-interaction matter in strong external magnetic fields. Strong, static magnetic fields will certainly influence the thermodynamics and lead to modifications of the transition temperature as well as the equation of state. Strong fields are generated in the early phase of heavy ion collisions[20,21] but weaken rapidly during the subsequent expansion phase. While lattice QCD calculations will allow to understand basic effects that occur in matter exposed to strong fields it is at present not clear to what extent equilibrium lattice QCD calculations can contribute to a quantitative analysis of experimental data.

2. QCD thermodynamics on the lattice

2.1. *Path integral formulation of QCD thermodynamics*

The equilibrium thermodynamics of elementary particles interacting only through the strong force is controlled by the QCD partition function which can be expressed in terms of a Euclidean path integral. The grand canonical partition function,

$Z(T,V,\vec{\mu})$, is given as an integral over the fundamental quark ($\bar{\psi}$, ψ) and gluon (A_ν) fields. In addition to its dependence on volume (V), temperature (T) and a set of N_f chemical potentials, $\vec{\mu} \equiv (\mu_u, \mu_d, \mu_s, ...)$ the partition function implicitly depends on the masses, $\vec{m} \equiv (m_u, m_d, m_s, ...)$, of the N_f different quark flavors. In this review we will most of the time discuss the thermodynamics of QCD with 2 light quarks (u,d) which are assumed to have degenerate masses, $m_u = m_d$, and a heavier strange quark (s), with mass m_s. This often is referred to as (2+1)-flavor QCD, or $N_f = 2+1$.

In Euclidean space-time, which is obtained from the Minkowski formulation by substituting $t \to -i\tau$ with $\tau \in \mathbb{R}$, the QCD Lagrangian is given by

$$\begin{aligned} \mathcal{L}^E_{QCD} &= \mathcal{L}^E_{gluon} + \mathcal{L}^E_{fermion} \\ &= -\frac{1}{4} F^{\mu\nu}_a(x) F^a_{\mu\nu} - \sum_{f=u,d,s...} \bar{\psi}^\alpha_f(x) \left(\not{D}^E_{\alpha\beta} + m_f \delta_{\alpha\beta} \right) \psi^\beta_f(x) \,, \end{aligned} \tag{1}$$

where Greek letters are spinor indices, $a = 1, .., N_c^2 - 1$ is the color index, N_c is the number of colors ($N_c = 3$ for QCD) and m_f is the mass of quarks with flavor f. The covariant derivative $\not{D}^E$ and the field strength tensor $F^a_{\mu\nu}$ are given by

$$\not{D}^E = \gamma^E_\mu D^E_\mu = \left(\partial_\mu + ig \frac{\lambda_a}{2} A^a_\mu \right) \gamma^E_\mu \,, \tag{2}$$

$$F^a_{\mu\nu} = \partial_\mu A^a_\nu - \partial_\nu A^a_\mu - g f^{abc} A^b_\mu A^c_\nu \,. \tag{3}$$

Here A^a_μ are the gauge fields, ψ^α_f ($\bar{\psi}^\alpha_f$) are the quark (anti-quark) fields, λ^a are the generators of SU(N_c), f_{abc} are the corresponding structure constants, γ^E_μ are the Euclidean Dirac matrices obeying $\{\gamma^E_\mu, \gamma^E_\nu\} = 2\delta_{\mu\nu}$, and g is the bare coupling constant.

In the Euclidean path-integral formalism the partition function of QCD is then given by

$$\mathcal{Z}(T,V,\vec{\mu}) = \int \prod_\mu \mathcal{D}A_\mu \prod_{f=u,d,s...} \mathcal{D}\psi_f \mathcal{D}\bar{\psi}_f \; \mathrm{e}^{-S_E(T,V,\vec{\mu})} \,, \tag{4}$$

with the Euclidean action

$$S_E(T,V,\vec{\mu}) \equiv - \int_0^{1/T} \mathrm{d}x_0 \int_V \mathrm{d}^3\mathbf{x} \; \mathcal{L}^E(\vec{\mu}) \,. \tag{5}$$

Here we have suppressed the dependence of the Euclidean Lagrangian and action on the fields $(A_\mu, \bar{\psi}_f, \psi_f)$ but have stressed explicitly their dependence on the various quark chemical potentials that couple to the conserved quark number currents

$$\mathcal{L}^E(\vec{\mu}) = \mathcal{L}^E_{QCD} + \sum_{f=u,d,s..} \mu_f \bar{\psi}_f \gamma_0 \psi_f \,. \tag{6}$$

The thermal expectation value of physical observables $\mathcal{O}$ can be obtained through

$$\langle \mathcal{O} \rangle = \frac{1}{Z(T,V,\vec{\mu})} \int \prod_{\mu} \mathcal{D}A_\mu \prod_f \mathcal{D}\psi_f \mathcal{D}\bar{\psi}_f \, \mathcal{O} \, \mathrm{e}^{-S_E(T,V,\vec{\mu})} \; . \tag{7}$$

Basic thermodynamic quantities like the pressure (P), energy density (ϵ) or net-quark number density n_f can be obtained from the logarithm of the partition function using standard thermodynamic relations,

$$\frac{P}{T^4} = \frac{1}{VT^3} \ln Z(T,V,\vec{\mu}) \; , \tag{8}$$

$$\frac{\epsilon}{T^4} = -\frac{1}{VT^4} \left. \frac{\partial \ln Z(T,V,\vec{\mu})}{\partial 1/T} \right|_{\vec{\mu}/T \text{ fixed}} \; , \tag{9}$$

$$\frac{n_f}{T^3} = \frac{1}{VT^3} \frac{\partial \ln Z(T,V,\vec{\mu})}{\partial \hat{\mu}_f} \; , \tag{10}$$

where we introduced the chemical potentials in units of temperature, $\hat{\mu}_f = \mu_f/T$. In fact, the QCD partition function depends on chemical potentials only through these dimensionless combinations, which are the logarithms of the fugacities, $z_f \equiv \exp(\mu_f/T)$.

As will become clear in the next subsection, the numerical analysis of thermodynamic observables at non-vanishing chemical potential, $\vec{\mu} \neq 0$, is difficult in lattice regularized QCD. A viable approach that circumvents the so-called sign-problem in lattice QCD at $\vec{\mu} \neq 0$, suitable for moderate values of the chemical potentials, is to consider Taylor expansions for thermodynamic observables. The starting point for such an analysis is the Taylor expansion of the pressure. In (2+1)-flavor QCD it reads

$$\frac{P}{T^4} = \sum_{i,j,k} \frac{1}{i!j!k!} \chi^{uds}_{ijk}(T) \left(\frac{\mu_u}{T}\right)^i \left(\frac{\mu_d}{T}\right)^j \left(\frac{\mu_s}{T}\right)^k \; , \tag{11}$$

where the expansion coefficients are dimensionless, generalized susceptibilities that can be evaluated at $\vec{\mu} = 0$,

$$\chi^{uds}_{ijk}(T) = \left. \frac{\partial^{i+j+k} P/T^4}{\partial \hat{\mu}_u^i \partial \hat{\mu}_d^j \partial \hat{\mu}_s^k} \right|_{\vec{\mu}=0} \; . \tag{12}$$

We will present results from Taylor expansions of QCD thermodynamics in several chapters of this review. Other thermodynamic observables and expressions more suitable for the calculation of P/T^4 and ϵ/T^4 in lattice regularized QCD will be introduced in later sections where they appear.

2.1.1. *The high temperature, ideal gas limit*

At very high temperatures, all quark masses are small on the scale of the temperature and massless QCD becomes a good approximation. Furthermore, because

of asymptotic freedom also interactions among quarks and gluons become small at high temperature. QCD thermodynamics thus approaches that of a non-interacting, massless quark-gluon gas. In the temperature range accessible to heavy ion collisions the massless limit of 3-flavor QCD is most relevant ($N_f = 3$). In this limit the pressure is given by

$$\left(\frac{P}{T^4}\right)_{\rm ideal} = \frac{8\pi^2}{45} + \sum_{f=u,d,s}\left[\frac{7\pi^2}{60} + \frac{1}{2}\left(\frac{\mu_f}{T}\right)^2 + \frac{1}{4\pi^2}\left(\frac{\mu_f}{T}\right)^4\right] \quad , \tag{13}$$

where the first term gives the contribution of gluons and the sum yields the contribution of quarks with different flavor degrees of freedom.

The thermodynamics of QCD at high temperatures can be systematically analyzed in perturbation theory. This, however, becomes complicated beyond $\mathcal{O}(g^2)$ due to the appearance of non-perturbative length scales of $\mathcal{O}(gT)$ and $\mathcal{O}(g^2T)$ reflecting electric and magnetic screening lengths,[22] which require the resummation of diagrams leading to the so-called hard thermal loop perturbation theory,[23,24] or the explicit integration over hard scales leading to the dimensional reduction scheme.[25,26]

2.1.2. *The low temperature hadron resonance gas approximation*

At low temperature quarks and gluons are confined in colorless hadrons, i.e. baryons and mesons are the relevant degrees of freedom. In fact, it turns out that even at temperatures close to the transition region from hadronic matter to the high temperature quark-gluon plasma phase a non-interacting gas constructed from all experimentally known resonances does provide quite a good description of QCD thermodynamics. This had been anticipated by R. Hagedorn when he formulated the hadron resonance gas (HRG)[1,4] model prior to QCD.

In an HRG model the pressure and other thermodynamic observables are easily obtained from the logarithm of the partition function,

$$\ln \mathcal{Z}_{HRG}(T,V,\vec{\mu}) = \sum_{i\in\, mesons} \ln \mathcal{Z}^M_{m_i}(T,V,\vec{\mu}) + \sum_{i\in\, baryons} \ln \mathcal{Z}^B_{m_i}(T,V,\vec{\mu}) \; , \tag{14}$$

where $\vec{\mu} = (\mu_B,\, \mu_Q,\, \mu_S)$ is the set of baryon number, electric charge and strangeness chemical potentials, respectively. The partition functions for mesons (M) or baryons (B) are given by

$$\ln \mathcal{Z}^{M/B}_{m_i}(T,V,\vec{\mu}) = \mp \frac{V}{2\pi^2}\int_0^\infty dk\, k^2\, \ln(1 \mp z_i e^{-\varepsilon_i/T}) \quad , \tag{15}$$

with energies $\varepsilon_i^2 = k^2 + m_i^2$ and fugacities

$$z_i = \exp\left((B_i\mu_B + Q_i\mu_Q + S_i\mu_S)/T\right) \quad . \tag{16}$$

Of course, $B_i = 0$ for all mesons and $B_i = \pm 1$ for baryons. The set of hadron chemical potentials, related to conserved quantum numbers, and the set of quark

flavor chemical potentials are easily related to each other,

$$\begin{aligned}\mu_u &= \frac{1}{3}\mu_B + \frac{2}{3}\mu_Q \ , \\ \mu_d &= \frac{1}{3}\mu_B - \frac{1}{3}\mu_Q \ , \\ \mu_s &= \frac{1}{3}\mu_B - \frac{1}{3}\mu_Q - \mu_S \ . \end{aligned} \tag{17}$$

With this it is straightforward to rewrite the Taylor series given in Eq. 11 in terms of quark chemical potentials, also in terms of baryon number, electric charge and strangeness chemical potentials,

$$\frac{P}{T^4} = \sum_{i,j,k} \frac{1}{i!j!k!} \chi^{BQS}_{ijk}(T) \left(\frac{\mu_B}{T}\right)^i \left(\frac{\mu_Q}{T}\right)^j \left(\frac{\mu_S}{T}\right)^k \ , \tag{18}$$

where the expansion coefficients[a] χ^{BQS}_{ijk} can again be evaluated at $\vec{\mu} = 0$,

$$\chi^{BQS}_{ijk}(T) = \left. \frac{\partial^{i+j+k} P/T^4}{\partial \hat{\mu}_B^i \partial \hat{\mu}_Q^j \partial \hat{\mu}_S^k} \right|_{\vec{\mu}=0} \ . \tag{19}$$

2.2. *Lattice Regularization and Continuum Limit*

Lattice gauge theory suggested by K. G. Wilson in 1974[13] is based on the Euclidean path integral formalism and provides a particular regularization scheme for QCD by introducing a finite lattice spacing as cut-off. In this way space-time is discretized and the path integral becomes a finite, yet high dimensional integral over the gauge and fermion field variables. The discretization of space and time introduces a systematic cut-off dependence in all observables, which vanishes when the lattice spacing is taken to zero, i.e. in the continuum limit. Many theoretical and technical details can be found in excellent textbooks such as Ref. 27–30. Here we will only give a brief introduction that may help to make this review self-contained.

By introducing a hyper-cubic lattice of size $N_\sigma^3 \times N_\tau$ with a small but finite lattice spacing a the calculation of observables given by Eq. 7 reduces to the evaluation of finite, but high dimensional integrals. Rather than calculating the partition function directly one usually is concerned with the calculation of expectation values, Eq. 7. This can be done by exploiting well-known Monte Carlo simulation techniques.[14] In order to preserve gauge invariance of the discretized action one introduces the gauge degrees of freedom as variables living on links between neighboring sites of the lattice, $U_{x,\hat{\mu}} \equiv \exp(iagA_\mu(x))$, while the fermionic degrees of freedom, $\bar{\psi}_x$ and ψ_x, are defined on the sites of the lattice. The latter are anti-commuting Grassmann variables and the former are $N_c \times N_c$ matrices that are elements of the $SU(N_c)$ color group.

[a]We will in general suppress super- and subscripts of the generalized susceptibilities, if a subscript is zero, i.e. $\chi^{BQS}_{102} \equiv \chi^{BS}_{12}$ or $\chi^{BQS}_{200} \equiv \chi^{B}_{2}$.

The volume V and the temperature T are related to the spatial and temporal extents of the lattice, respectively,

$$V = (aN_\sigma)^3, \qquad T = \frac{1}{aN_\tau} \; . \tag{20}$$

Here N_σ and N_τ are the number of sites in spatial and temporal directions. A consequence of introducing a discrete space-time lattice is that aside from Lorentz symmetry also some of the symmetries of QCD get explicitly broken by the finite lattice cut-off. They will be recovered in the continuum limit, $a \to 0$ at fixed V and T. Asymptotically, for small values of the bare gauge coupling g this is controlled by the QCD β-function

$$a\Lambda_L = \left(\frac{1}{b_0 g^2}\right)^{b_1/2b_0^2} \mathrm{e}^{-1/2b_0 g^2} \; , \tag{21}$$

with $b_0 = \left(\frac{11}{3}N_c - \frac{2}{3}N_f\right)/16\pi^2$ and $b_1 = \left(\frac{34}{3}N_c^2 - \left(\frac{10}{3}N_c + \frac{N_c^2-1}{N_c}\right)N_f\right)/(16\pi^2)^2$.

Keeping physical observables constant when approaching the continuum limit also requires a proper tuning of the bare quark masses. In the discretized version of QCD (lattice QCD) all quark masses are naturally expressed in units of the lattice spacing, $\hat{m}_f \equiv m_f a$. Taking the continuum limit thus requires to take the limit, $g^2 \to 0$ and $\hat{m}_f \to 0$ while keeping some physical observables, i.e. one per flavor degree of freedom, constant. This defines "lines of constant physics" (LCP) in the space of quark masses and the gauge coupling. In the case of (2+1)-flavor QCD with degenerate light quark masses, $m_u = m_d$, one thus can determine the bare quark mass parameters $\hat{m}_l \equiv \hat{m}_u$ and the strange quark mass $\hat{m}_s$ using two physical observables. An often used approach is to fix the strange quark mass using the (fictitious) $\eta_{s\bar{s}}$ meson mass, which only contains strange quarks and is quite insensitive to light quark mass values. This mass is matched to the lowest order chiral perturbation theory estimate $m_{\eta_{s\bar{s}}} = \sqrt{2m_K^2 - m_\pi^2}$. The light quark mass is then fixed using a constant ratio $\hat{m}_s/\hat{m}_l$, the value corresponding to the physical pion mass value is $\hat{m}_s/\hat{m}_l = 27.5$.[31]

The lattice regularized partition function may be written as

$$\begin{aligned} \mathcal{Z}(T,V,\vec{\mu}) &= \int \prod_{x,\hat{\mu}} \mathrm{d}U_{x,\hat{\mu}} \prod_{x,f} \mathrm{d}\psi_{x,f} \mathrm{d}\bar{\psi}_{x,f} \; \mathrm{e}^{-S_f - S_g} \; , \\ &= \int \prod_{x,\hat{\mu}} \mathrm{d}U_{x,\hat{\mu}} \; \prod_f \det M_f(\mu_f) \; \mathrm{e}^{-S_g} \; , \end{aligned} \tag{22}$$

where S_g and S_f are the discretized versions of the gluonic and fermonic part of the action S_E. As the action is bilinear in the quark fields these can be integrated out, which gives rise to the determinant of fermion matrix M_f. Quite often exploratory lattice QCD studies are performed in the so-called "quenched approximation". This refers to the calculation of observables that contain fermionic degrees of freedom as valence quarks. However, back-reaction of fermions on the gauge fields (virtual quark loops) are not included in the observables. This is achieved by fixing $\det M_f =$

const. in Eq. 22, i.e. the determinant does not contribute in the generation of gauge field configurations nor does it contribute in the calculation of expectation values.

The fermion matrix depends on the quark chemical potential μ_f which is introduced on the time-like links of the lattice.[32] Although other formulations are possible[33] a common approach is to replace the link variables, $U_{x,\hat{0}} \to \exp(\mu_f a) U_{x,\hat{0}}$ and $U^\dagger_{x,\hat{0}} \to \exp(-\mu_f a) U^\dagger_{x,\hat{0}}$. The fermion determinant is positive definite only for $\mu_f \equiv 0$. For non-zero values of the chemical potential $\det M_f(\mu_f)$ is a complex function. Still the partition function is real, i.e. integration over the gauge fields eliminates the imaginary contributions. However, the real part of the fermion determinant still changes sign, which prohibits the application of conventional Monte Carlo simulation techniques. This is known as the 'sign-problem' in finite density QCD. There are various attempts to circumvent this sign-problem in numerical simulations performed directly at non-vanishing $\vec{\mu}$. At present complex Langevin simulation techniques[34–36] and the integration over Lefschetz thimbles[37–39] are most actively being explored. In this review we will focus on the Taylor expansion approach[40,41] for the evaluation of thermodynamic observables at non-zero chemical potential. This only requires numerical simulations at vanishing baryon chemical potential. However, it is naturally limited in applicability through the radius of convergence of the Taylor series which remains to be determined for QCD.

2.3. *Fermion discretization schemes*

When discretizing the Euclidean action one has quite some freedom. Discretization schemes that differ by higher order corrections in the cut-off are equivalent to the extent that they yield the same physical answers in the continuum limit. The basic construction principle of a lattice discretized version of QCD is that one wants to start with a theory that is manifestly gauge invariant. In addition one tries to choose discretization schemes that preserve as many of the symmetries of QCD as possible already at non-zero values of the lattice spacing. The discretization of the gluonic part of the action, S_g, is rather straightforward and well-established improvement schemes (Symanzik improvement[42,43]) are known that allow to eliminate systematically higher order cut-off errors.

Some difficulties already arise in the naive discretization of the fermionic part of the Euclidean action, S_f. When one simply approximates the covariant derivative in the fermion action by nearest-neighbor differences of the quark fields additional, unphysical degrees of freedom arise even in the continuum limit owing to the periodicity of the fermion dispersion relation on the lattice. This is known as the fermion doubling problem which is closely related to the explicit breaking of chiral symmetry in most commonly used fermion discretization schemes.[44]

There are several discretization schemes for the fermionic part of the action such as Wilson fermions,[13] staggered fermions,[45] Domain Wall fermions[46–49] as well as overlap fermions.[50,51] They differ to the extent they preserve chiral symmetry and/or eliminate the problem of fermion doublers. Wilson fermions avoid the dou-

bling problem by adding a dimension five operator to the naively discretized fermion action.[13] A variant of this is the so-called clover-improved Wilson fermion action where lattice cutoff effects are reduced from $\mathcal{O}(a)$ to $\mathcal{O}(a^2)$.[52] Most commonly used in QCD thermodynamics calculations is the staggered fermion discretization scheme in which the Dirac 4-spinor is spread over several lattice sites.[45] This reduces the doubler problem but does not eliminate it completely. However, it preserves a $U(1)_{even} \times U(1)_{odd}$ remnant of chiral symmetry, which allows independent rotations of the quark fields on even and odd sites of the lattice, respectively. This is of great advantage in the study of chiral symmetry breaking at non-zero temperature as it allows to introduce an order parameter, the chiral condensate, that is sensitive to the spontaneous breaking of this continuous symmetry. The reduction of the doubler problem in the staggered fermion approach leads to the introduction of additional heavier states for each fermion flavor. In the continuum limit these so-called taste symmetry partners will become degenerate with the Goldstone mode that corresponds to the broken $U(1)_{even} \times U(1)_{odd}$ symmetry. The Goldstone boson thus has another 15 heavier partners (tastes) which become degenerate with the Goldstone boson only in the continuum limit. To reduce the taste symmetry breaking, i.e. reduce the mass difference between physical states and their heavier taste partners two improved staggered actions, the Highly Improved Staggered Quarks (HISQ)[53] and the stout smeared action,[54] are commonly used in lattice studies of QCD thermodynamics. In Fig. 2 (left) we show some results for the cut-off dependence of the root-mean-square mass values $M_\pi^{\rm RMS}$ of the Goldstone particle and its 15 taste partners calculated in different staggered fermion discretization schemes. As seen in the left panel of Fig. 2 the 4stout and HISQ actions have the smallest $M_\pi^{\rm RMS}$. The right hand panel of this figure shows the influence of cut-off effects on the calculation of the fermion contribution to the pressure in the high temperature ideal gas limit. These cut-off effects are independent of the taste improvement schemes and solely arise from the strategy used to discretize the covariant derivatives appearing in the fermion action. The stout-smeared actions utilize the naive 1-link discretization scheme that leads to $\mathcal{O}(a^2)$ errors in the ideal gas limit. In the HISQ, asqtad and p4[55] actions 3-link terms are added to the action that eliminate the leading order cut-off effects in the ideal gas limit. In these cases discretization errors only start at $\mathcal{O}(a^4)$.

Domain Wall fermions (DWF) and overlap fermions allow for an exact representation of chiral symmetry even at non-zero lattice spacing. In the Domain Wall discretization scheme the physical chiral Dirac fermions are constructed on two 4-dimensional hyper-surfaces at the edges of a 5-dimensional lattice with extent L_s in that fifth direction. These hyper-surfaces represent the usual 4-dimensional space-time and on each of the surfaces fermions with one given chirality exist. There persists a small explicit breaking of chiral symmetry which vanishes exponentially in the limit $L_s \to \infty$. In DWF calculations this gives rise to a small additive renormalization of the quark masses, the so-called residual mass[56] m_{res}. Controlling and

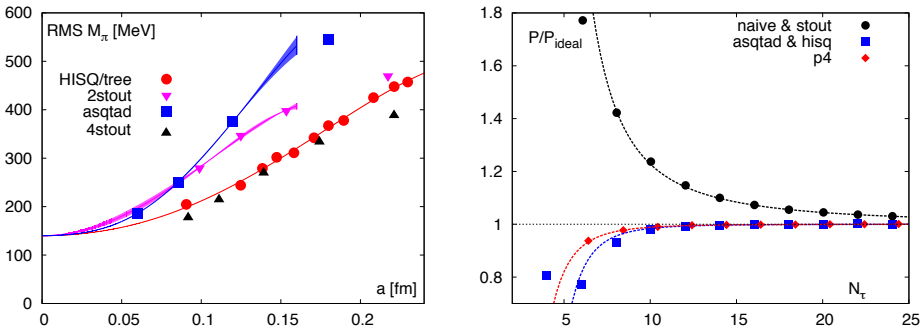


Fig. 2. (Left) Root mean squared pion mass ($M_\pi^{\rm RMS}$) as a function of lattice spacing a. RMS M_π is defined as the rooted sum of the mass squared of 16 pseudo scalar states divided by 4. The lattice cutoff effects are smaller with smaller $M_\pi^{\rm RMS}$. (Right) Ratio of quark contribution to the pressure, obtained from lattice QCD calculations in the infinite temperature, ideal gas limit, to the pressure of an ideal quark gas in the continuum ($P_{\rm ideal}$) as a function of N_τ. $P/P_{\rm ideal}$ approaches unity in the continuum limit.

reducing these residual mass effects is one of the important improvement steps in calculations with DWF.[57] Overlap fermions on the other hand preserve exact chiral symmetry on a 4-dimensional lattice by obeying the Ginsparg-Wilson relation at non-zero lattice spacing.[58]

Numerical calculations with Domain Wall as well as overlap fermions are quite time consuming. However, with increasing speed of super-computers calculations with physical light quark masses become feasible and chiral fermions have been used recently also for QCD thermodynamics studies.[59–62] In particular in the analysis of subtle aspects of the QCD transition related to the temperature dependence of the axial anomaly, calculations with fermions obeying exact chiral symmetry already at non-zero values of the cut-off are mandatory.

3. QCD phase diagram at high temperature

Our thinking about the phase structure of strong-interaction matter centers around two very basic concepts in strong interaction physics – confinement and chiral symmetry breaking. The former expresses the fact that only colorless states, baryons and mesons, can exist in the vacuum and are observed experimentally. This gave rise to the concept of a linearly rising, confining potential exhibited between quarks and anti-quarks,

$$V_{q\bar{q}}(r) = -\frac{\alpha(r)}{r} + \sigma r \ , \tag{23}$$

with σ being the string tension and $\alpha(r)$ the running coupling of QCD.

Chiral symmetry breaking, on the other hand is a mandatory feature of strong interactions needed to explain the appearance of a light, almost massless, particle

in the hadron spectrum – the pions. In the limit of vanishing quark masses the QCD Lagrangian has a build-in chiral symmetry. It is invariant under independent global rotations of quarks with left and right handed chirality in flavor space as well as chiral rotations of single flavor quark spinors. This gives rise to the $U(N_f)_L \times U(N_f)_R$ chiral symmetry which is equivalent to $SU(N_f)_L \times SU(N_f)_R \times U(1)_A \times U_V(1)$. The latter $U_V(1)$ reflects the conservation of baryon number, and the axial $U(1)_A$ symmetry, although an exact symmetry of the classical QCD Lagrangian, is explicitly broken by quantum fluctuations. The global $SU(N_f)_L \times SU(N_f)_R$ flavor symmetry, on the other hand, is broken spontaneously in massless QCD, giving rise to massless Goldstone modes and a non-vanishing chiral condensate,

$$\langle\bar{\psi}\psi\rangle_f = \frac{T}{V}\frac{\partial \ln Z}{\partial m_f} \quad , \quad f = 1, ..., N_f. \tag{24}$$

The masses of the light pseudo-scalar (Goldstone) pions are then understood as arising from the small non-zero values of the light up and down quark masses. This is reflected in the Gell-Mann-Oakes-Renner relation between the pion mass (m_π), the quark masses (m_u, m_d), the pion decay constant (f_π) and the non-vanishing chiral condensate $\langle\bar{\psi}\psi\rangle = \langle\bar{\psi}\psi\rangle_u + \langle\bar{\psi}\psi\rangle_d$ that arises from the spontaneous breaking of chiral symmetry,

$$f_\pi^2 m_\pi^2 = \frac{1}{2}(m_u + m_d)\langle\bar{\psi}\psi\rangle \; . \tag{25}$$

The fact that QCD describes confinement as well as spontaneous breaking of chiral symmetry is not evident from the QCD Lagrangian or the perturbative treatment of strong interactions described by it. It requires a non-perturbative analysis – lattice QCD calculations – to firmly establish the confining and symmetry breaking features of QCD.

Asymptotic freedom of QCD suggests that non-perturbative effects are suppressed at high temperatures and hot strong-interaction matter approaches ideal gas behavior asymptotically. It thus is expected that non-perturbative condensates also disappear at high temperatures. For exact global symmetries of QCD this is expected to happen through a true phase transition. Basic features of this transition can be understood by invoking universality arguments.[10]

The nature of the QCD transition depends crucially on the values of the quark masses and the number of flavors (N_f). Fig. 3 shows a sketch of the nature of the QCD transition as functions of the quark masses for a theory with two degenerate light (up and down) quarks with masses, $m_{u,d} \equiv m_l = m_u = m_d$, and a heavier strange quark with mass, m_s, at zero baryon chemical potential. In the limit $m_l \to \infty$ and $m_s \to \infty$ fermions decouple and the thermodynamics of a pure $SU(3)$ gauge theory ($N_f = 0$) is recovered. The $SU(3)$ gauge theory has an exact $Z(3)$ symmetry and the deconfimement transition is first order. This first order region extends to lower quark masses and ends at a second order critical line that belongs to the universality class of the 3-d, Z(2) symmetric Ising model.[63,64] For three degenerate flavors $N_f = 3$ with small quark masses $m_l = m_s \to 0$ the chiral transition is

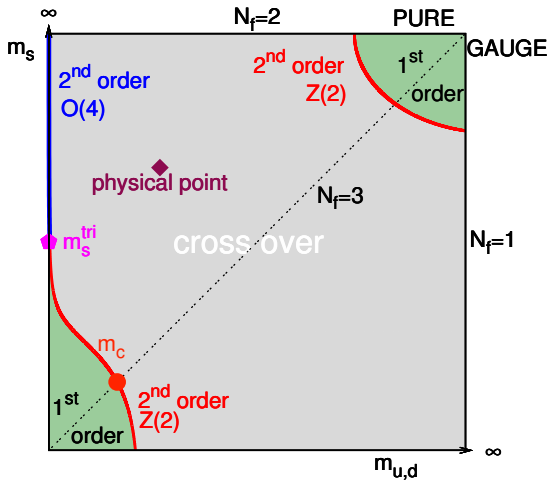


Fig. 3. A sketch of the nature of the QCD transition as functions of the two degenerate light (up and down) quarks with masses, $m_{u,d} \equiv m_l$, and a heavier strange quark with mass, m_s, at zero baryon chemical potential.

known to be first order.[65,66] Recent lattice QCD studies[67,68] with improved actions suggest that the extent of this first order region is quite small, i.e. limited to $m_l = m_s \lesssim m_s^{phys}/270$ where m_s^{phys} is the physical value of the strange quark mass.

An additional ingredient in the discussion of the order of the transition in the chiral limit arises from the role of the axial anomaly. The nature of the chiral transition for the massless $N_f = 2$ theory , i.e. for $m_l \to 0$ and $m_s \to \infty$, depends on the magnitude of the axial $U_A(1)$ symmetry breaking. If this remains significant close to the transition temperature then the relevant symmetry becomes isomorphic to that of the 3-d $O(4)$ spin model and the transition is expected to be second order belonging to that universality class.[10,69] However, if $U_A(1)$ symmetry breaking becomes negligible near the chiral transition temperature, the relevant symmetry becomes isomorphic to $O(2) \times O(4)$ and the transition be either first order[10] or second order.[70,71] In the intermediate quark mass region there is no true phase transition, rather a crossover takes place from the hadronic to the quark-gluon plasma phase.

All the first order regions are separated from the crossover region by lines of second order phase transitions belonging to the 3-d $Z(2)$ universality class. The first order region for the $N_f = 2 + 1$ case, the second order $Z(2)$ line separating the $N_f = 2 + 1$ first order and the crossover regions and the second order $O(4)$ line for the $N_f = 2$ case are supposed to meet at a tri-critical point characterized by a certain value of the strange quark mass, m_s^{tric}. Although, it is well established that in the real world, i.e. for the physical values of the quark masses, the transition is a crossover,[61,72] the location of the physical point with respect to m_s^{tric} has not been established and even $m_s^{tric} \to \infty$ cannot be ruled out. More specifically, it

is yet unclear whether $m_s^{phys} > m_s^{tric}$ or $m_s^{phys} = m_s^{tric}$ or $m_s^{phys} < m_s^{tric}$. If $m_s^{phys} > m_s^{tric}$ then in the limit of $m_l \to 0$ one should find a second order transition belonging to the 3-d $O(4)$ universality class, if $m_s^{phys} = m_s^{tric}$ the tri-critical point is a Gaussian fixed point of the 3-dimensional ϕ^6 model and its critical exponents take the mean field values[73] and if $m_s^{phys} < m_s^{tric}$ then in the $m_l \to 0$ limit one may cross through a second order transition belonging to the 3-d $Z(2)$ universality class and then may end up in the first order transition region.

In the following discussion we assume $m_s^{phys} > m_s^{tric}$.

3.1. *Chiral transition in (2+1)-flavor QCD*

In the vicinity of the chiral phase transition, the free energy density may be expressed as a sum of a singular and a regular part

$$f = -\frac{T}{V} \ln Z \equiv f_{sing}(t,h) + f_{reg}(T, m_l, m_s, \vec{\mu}) \; . \tag{26}$$

The parameter h represents the dimensionless explicit chiral symmetry breaking (magnetic) field and t incorporates all the 'thermal' variables that do not explicitly break the chiral symmetry, e.g. at leading order,

$$t = \frac{1}{t_0} \left[\frac{T - T_c^0}{T_c^0} + \kappa_q \left(\frac{\mu_q}{T} \right)^2 \right] \; , \qquad \text{and} \qquad h = \frac{1}{h_0} \frac{m_l}{m_s} \; , \tag{27}$$

where $\mu_q \equiv \mu_u = \mu_d$. T_c^0 denotes the (unknown) phase transition temperature in the chiral limit $m_l \to 0$ and for $\mu_q = 0$. The scaling variables t, h are normalized by two unknown parameters t_0 and h_0. The other unknown parameter κ_q controls how the chiral transition temperature T_c^0 changes as a function of μ_q. All these 4 unknown quantities $(T_c, \kappa_q, t_0, h_0)$ are unique to QCD, similar to the low energy constants in the chiral Lagrangian. These parameters can be determined by analyzing the scaling behaviors, arising from the singular part of the free energy, of the chiral order parameter and susceptibilities using lattice QCD.

3.1.1. *Pseudo-critical behavior at vanishing chemical potential*

Sufficiently close to the QCD chiral transition the renormalization group invariant dimensionless order parameter M_b, constructed out of the light quark chiral condensate, defined in Eq. 24, and the strange quark mass obeys the scaling relation

$$M_b \equiv \frac{m_s \langle \bar{\psi}\psi \rangle_l}{T^4} = h^{1/\delta} f_G(z) + \text{regular terms} \; , \tag{28}$$

in terms of a single scaling variable $z = t/h^{1/\beta\delta}$. The critical exponents β and δ and the scaling function $f_G(z)$ uniquely characterize the universality class of the chiral phase transition. As discussed before, for continuum QCD the relevant universality class is expected to be the same as that of 3-d $O(4)$ spin models. However, the situation is more subtle for QCD on the lattice. For example, since for staggered fermions away from the continuum limit there is only one Goldstone boson in the

chiral limit the relevant universality class is that of the 3-d $O(2)$ spin model. Table 1 summarizes the critical exponents and other relevant quantities for the 3-d $O(2)$ and $O(4)$ universality classes.

Fig. 4 shows results for the chiral order parameter M_b calculated in (2+1)-flavor QCD[76] for several values of the light to strange quark mass ratio m_l/m_s while keeping m_s fixed to its physical value m_s^{phys}. In the continuum limit the physical value of this ratio is $m_l^{phys}/m_s^{phys} = 1/27.5$.[31] The left hand panel in Fig. 4 shows the variation of M_b with temperature calculated on rather coarse lattices ($N_\tau = 4$) for several values of m_l/m_s. In the continuum limit the smallest of these ratios would correspond to pion masses of about 80 MeV. Clearly, the transition sharpens as the light quark masses become smaller. The right hand panel of Fig. 4 shows a comparison of the scaled order parameter $M_b/h^{1/\delta}$ (see Eq. 28) with the $O(2)$ scaling function. As can be seen, for small enough light quark masses, $m_l \lesssim m_s^{phys}/20$, the scaled order parameter for different values of the light quark mass collapses on a unique curve and compares well with the $O(2)$ scaling function. While these lattice results suggest that the chiral transition for $N_f = 2$ theory belongs to the 3-d $O(N)$ universality class one should bear in mind that these results are not continuum extrapolated and discretization effects may change the conclusion. In fact, lattice studies performed with the unimproved staggered action even further away from the continuum limit suggest that in this case the transition may even be first order.[77]

The chiral order parameter M_b can be used to define two susceptibilities obtained by either taking a derivative with respect to 'thermal' variable t, which give the mixed susceptibility $\chi_t \sim \partial M_b/\partial t \sim \partial^2 f_s/\partial t \partial h$, or with respect to the symmetry breaking variable, $\chi_h \sim \partial M_b/\partial h \sim \partial^2 f_s/\partial h^2$. These two susceptibilities are the only two second derivatives of the free energy of an $O(N)$ symmetric theory like QCD that diverge at the critical point[b], i.e. at $T = T_c^0$ for $m_l = 0$. Their singular behavior is controlled by two scaling functions, $f_G'(z) = \mathrm{d}f_G(z)/\mathrm{d}z$, and $f_\chi(z) = (f_G(z) - (z/\beta)f_G'(z))/\delta$, respectively. Away from the chiral limit, these two scaling functions have maxima at universal values of z, i.e. $z = z_t$ and $z = z_p$ (see Tab. 1),

[b]In general, there is a third susceptibility, the specific heat, C_V, which is obtained as a second derivative of the free energy with respect to the 'thermal' variable t, $C_V \sim \partial^2 f_s/\partial t^2$. In $O(N)$ symmetric theories, however, the relevant critical exponent α is negative. The specific heat, thus, does not diverge at T_c in the chiral limit.

Table 1. Critical exponents α, β, γ, δ for the 3-dimensional $O(N)$ universality classes.[74,75] Only two of the four critical exponents are independent. They are related to each other through the scaling relations $\gamma = \beta(\delta - 1)$ and $\alpha + 2\beta + \gamma = 2$. The last two columns give the location of the maxima of the scaling functions $f_G'(z)$ and $f_\chi(z)$, respectively.[74,75]

N	α	β	γ	δ	z_t	z_p
2	-0.017	0.349	1.319	4.779	0.46(20)	1.56(10)
4	-0.213	0.380	1.453	4.824	0.73(10)	1.35(3)

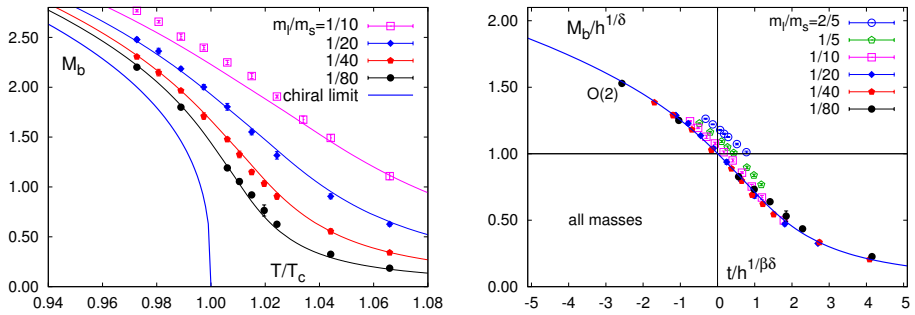


Fig. 4. $O(N)$ scaling of the chiral order parameter M_b introduced in Eq. 28 for (2+1)-flavor QCD.[76]

which can be used to define pseudo-critical temperatures.

For example, the scaling behavior of the chiral susceptibility for two light, degenerate flavors,

$$\chi_{m,l}(T) = 2\frac{\partial\langle\bar{\psi}\psi\rangle_l}{\partial m_l} \,, \tag{29}$$

is related to that of χ_h. The renormalization group invariant product of the chiral susceptibility $\chi_{m,l}$ and the square of the strange quark mass is related to the scaling functions by,

$$\frac{m_s^2\chi_{m,l}}{T^4} = \frac{1}{h_0}h^{1/\delta-1}f_\chi(z) + \text{regular terms} \,. \tag{30}$$

At vanishing quark chemical potential the chiral susceptibility thus diverges at the chiral critical temperature T_c^0 in the chiral limit $h \to 0$. The peak location of the chiral susceptibility will then be associated with the peak of the scaling function $f_\chi(z)$, located at $z = z_p$, and defines the chiral pseudo-critical temperature T_c for $h > 0$,

$$T_c = T_c^0\left[1 + \frac{z_p}{z_0}\left(\frac{m_l}{m_s}\right)^{1/\beta\delta}\right] + \text{regular terms} \,, \tag{31}$$

with $z_0 = t_0/h_0^{1/\beta\delta}$. As illustrated in Fig. 5, the chiral crossover temperature for physical QCD with $m_s = m_s^{phys}$ and $m_l^{phys} = m_s^{phys}/27.5$ was studied in detail[78] by using such a scaling analysis of the chiral susceptibility, including the influence of regular terms. By performing scaling fits to the chiral susceptibility, extrapolating to the physical value of light quark mass and subsequently taking the continuum limit one obtains a value of

$$T_c = (154 \pm 9)\ \text{MeV} \tag{32}$$

for the chiral crossover temperature in (2+1)-flavor physical QCD.[78] Studies with other improved staggered fermion discretization schemes,[79–81] which used other

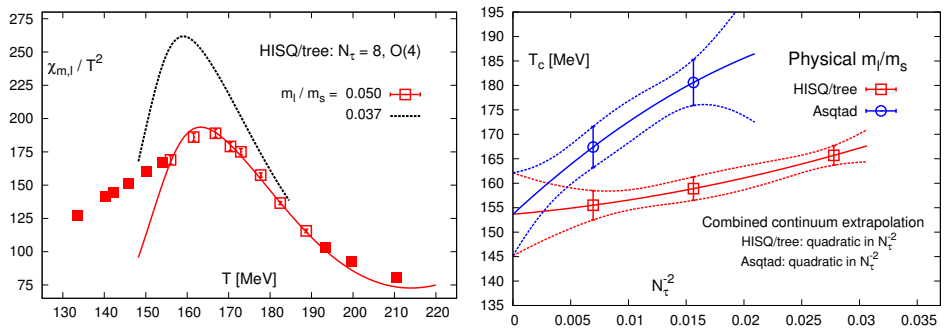


Fig. 5. (Left) $O(4)$ scaling of the chiral susceptibility and its extrapolation to the physical light quark mass for (2+1)-flavor QCD.[78] The peak location of the chiral susceptibility defines the chiral crossover temperature. (Right) Continuum extrapolation of the chiral crossover temperature for (2+1)-flavor physical QCD, yielding $T_c = (154 \pm 9)$ MeV.[78]

criteria, not directly related to criticality, to define a crossover temperature, and with chiral Domain Wall Fermions[61] also yielded compatible results for the QCD chiral crossover temperature.

3.1.2. *Curvature of the pseudo-critical line*

The scaling behavior of the mixed susceptibility, χ_t, can be utilized to determine the chiral phase boundary in the T-μ plane.[82] As introduced in Eq. 27, to leading order the chemical potential μ_q does not contribute to the explicit chiral symmetry breaking field h and can be treated as part of the 'thermal' scaling variable t. Thus, the derivative of the order parameter with respect to the chemical potential, $\chi_{m,\mu} = \partial^2 M_b/\partial(\mu_q/T)^2$, is equivalent to the mixed susceptibility, χ_t. The scaling behavior of the renormalization group invariant combination of $\chi_{m,\mu}$ multiplied with the strange quark mass, which combines a 'thermal' and 'field-like' derivative of the free energy, is given by

$$\frac{m_s \chi_{m,\mu}}{T^2} = \frac{2\kappa_q}{t_0} h^{-(1-\beta)/\beta\delta} f'_G(z) + \text{regular terms} \,. \tag{33}$$

In the chiral limit, $h \to 0$, this susceptibility diverges at T_c^0 for $\mu_q = 0$. For $\mu_q > 0$, the chemical potential dependence of the chiral transition temperature $T_c^0(\mu_q)$ is defined by the peak location, $z = z_t$, of the scaling function $f'_G(z)$ and in the leading order in $(\mu_q/T)^2$ it is given by

$$T_c^0(\mu_q) = T_c^0 \left[1 - \kappa_q \left(\frac{\mu_q}{T_c^0} \right)^2 + \mathcal{O}\left[\left(\frac{\mu_q}{T_c^0} \right)^4 \right] \right] + \text{regular terms} \,. \tag{34}$$

As illustrated in Fig. 6 (left), the curvature of the chiral phase transition line, κ_q, can be determined by fitting the scaled susceptibility $m_s t_0 h^{(1-\beta)/\beta\delta} \chi_{m,\mu}/T^2$ to the universal scaling function $f'_G(z)$.[82] Such a scaling analysis provides a value of the

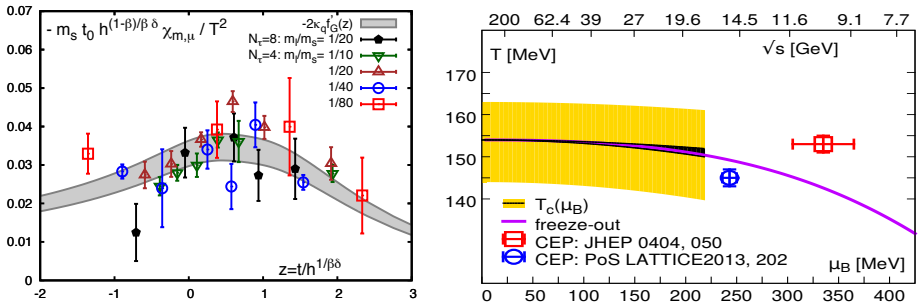


Fig. 6. (Left) $O(N)$ scaling of the susceptibility $\chi_{m,\mu}$ and determination of the curvature, κ_q, of the chiral phase boundary in the T-μ_q plane.[82] (Right) Chiral crossover temperature as function of baryon chemical potential, $T_c(\mu_B)$, compared with the freeze-out temperature in heavy-ion collisions. The parametrization of the freeze-out line is taken from Ref. 86, with the freeze-out temperature in the limit of infinite collision energy adjusted to the crossover temperature at vanishing chemical potential, $T_{fo}(\sqrt{s} \to \infty) = 154$ MeV. The black band for the crossover line, $T_c(\mu_B)$, reflects the systematic uncertainty arising from a factor of 2 difference in current estimates from calculations with real[82,83] and imaginary[84,85] μ_B (see text). Data points are from a reweighting analysis[87] and Taylor expansion[88] (see text). They also are normalized to $T_c = 154$ MeV.

curvature $\kappa_q = 0.059(6)$.[82] In terms of the baryon chemical potential $\mu_B = 3\mu_q$, the chiral transition temperature is then given by

$$T_c^0(\mu_B) = T_c^0 \left[1 - 0.0066(7) \left(\frac{\mu_B}{T_c^0} \right)^2 + \mathcal{O}\left[\left(\frac{\mu_B}{T_c^0} \right)^4 \right] \right] . \qquad (35)$$

This result is in very good agreement with the independent determination of the continuum extrapolated results of the curvature of the chiral phase boundary for (2+1)-flavor of physical QCD,[83] using different criteria. However, analytic continuation from purely imaginary chemical potential yields a factor two larger values for the curvature.[84,85] Fig. 6 (right) shows the proximity of the QCD phase boundary to the freeze-out line in heavy-ion collisions[86] in the T-μ_B plane.

3.1.3. *The critical end point*

Information on the location of a critical end point (CEP) in the QCD phase diagram (Fig. 1) from lattice QCD is ambiguous. Although considerable progress in developing algorithms that would allow direct calculations in lattice QCD at $\mu_B > 0$ have been made recently (see Ref. 36 for a recent review) these techniques are not yet applicable to realistic QCD parameter values.

The first calculations that provided hints for the existence of a critical point[87] used a reweighting technique that is applicable only on rather small lattices. It had been performed on coarse lattices with temporal extent $N_\tau = 4$ using only the naive 1-link staggered fermion action. Taste violation effects thus are large and the

reweighting is known to fail when used too far away from the parameters actually used in the calculations. It has been argued that this 'overlap problem' may have led to the spurious identification of a signal for a critical point.[89] Calculations performed with an imaginary chemical potential do not find any evidence for the existence of a critical point.[90] However, also these calculations have been performed on coarse lattices and utilized the naive staggered 1-link action.

The conclusions drawn in Ref. 90 are based on an analysis of the μ_B-dependence of the location of the boundary line that separates the first order transition region shown in Fig. 3 at small quark masses from the crossover region. These calculations, performed with staggered fermions using an imaginary chemical potential,[90] suggest that this boundary moves to smaller quark masses with increasing chemical potential. This disfavors the existence of a critical point connected to the Z(2) boundary line at vanishing chemical potential. A similar analysis, performed with clover-improved Wilson fermions, comes to the opposite conclusion[91] and thus does favor the existence of a critical point. The apparent differences between calculations performed with staggered fermions and Wilson fermions on coarse lattices underscores that better control over systematic errors is needed before a definite conclusion on the existence of a critical point can be drawn.

Analyzing the convergence properties of the Taylor series for the pressure at non-zero chemical potential[40,92] (Eq. 18) does, in principle, allow to relate the location of the CEP to the radius of convergence of this series. Although this approach has been used closer to the continuum limit ($N_\tau = 8$)[88,93] than the studies discussed above, the current estimates still are based on calculations with the naive staggered 1-link action. They still suffer from large taste symmetry violations. These calculations yield for the location of the critical point[88] $(T^E/T_c, \mu_B^E/T^E) = (0.94(1), 1.68(5))$[93] which is significantly lower than the reweighting result $(T^E/T_c, \mu_B^E/T^E) = (0.99(1), 2.2(2))$.[87] We show these two estimates for the location of the CEP in Fig. 6 (right). The systematic errors of these estimates are at present difficult to estimate.

Further information on the location of a critical point comes from the calculations of (i) the equation of state at $\mu_B > 0$ performed with improved staggered fermions, which we will discuss in Section 4, as well as (ii) the analysis of freeze-out parameters based on Taylor expansions of cumulants of charge fluctuations, which are also performed with improved staggered actions and which we will discuss in Section 5, both suggest that a CEP located at $\mu_B/T < 2$ is unlikely.

3.2. *Deconfining aspect of QCD*

Pure $SU(N_c)$ Yang-Mills theory without quarks possess an exact global $Z(N_c)$ center symmetry, which gets spontaneously broken in the high temperature deconfining

phase.[15,16] The thermal expectation value of the renormalized Polyakov loop

$$L_{\rm ren}(T) = e^{-c(g^2)N_\tau} \cdot \frac{1}{VN_c} \sum_{\vec{x}} \left\langle {\rm Tr} \prod_{x_0=1}^{N_\tau} {\rm U}_{(x_0,\vec{x}),\hat{0}} \right\rangle \ , \tag{36}$$

is not invariant under the $Z(N_c)$ center symmetry. The Polyakov loop can be interpreted as the free energy difference, $F_\infty(T)$, of a thermal system with and without an infinitely heavy static quark anti-quark pair separated by infinite distance, $L_{\rm ren}(T) = \exp(-F_\infty(T)/2T)$. The renormalization constant $c(g^2)$ can be fixed[94] by demanding that in the short distance limit the heavy quark free energy coincides, up to a trivial additive constant, with the Coulombic short distance behavior of the zero temperature heavy quark potential defined in Eq. 23. In the confined phase $F_\infty(T) = \infty$, as a static quark and anti-quark pair cannot be separated by infinite distance in this phase. Thus in the $Z(N_c)$ symmetric confined phase $L_{\rm ren}(T) = 0$. On the other hand, in the spontaneously $Z(N_c)$ broken deconfined phase a static quark anti-quark pair can be separated by infinite distance due to the presence of color screening and $L_{\rm ren}(T) \neq 0$. Thus, for a pure $SU(N_c)$ gauge theory, i.e. in the limit $m_l \to \infty$, the Polyakov loop serves as the order parameter for the deconfinement transition.[95] However, since the mere presence of quarks explicitly breaks the $Z(N_c)$ center symmetry, the Polyakov loop does not serve as an order parameter for QCD with realistic light quarks. Furthermore, since the Polyakov loop is not related to a derivative of the QCD partition function with respect to the thermal or the symmetry breaking field, its change or fluctuation across the QCD transition may not capture the true singularities of the QCD partition function in any limit. Thus, a deconfining temperature defined from the change of the Polyakov loop may not reflect the pseudo-critical properties of QCD with realistic light quark masses. As shown in Fig. 7 (left), the change of the Polyakov loop within the chiral crossover region, $T_c = 154(9)$ MeV, is rather gradual and smooth.

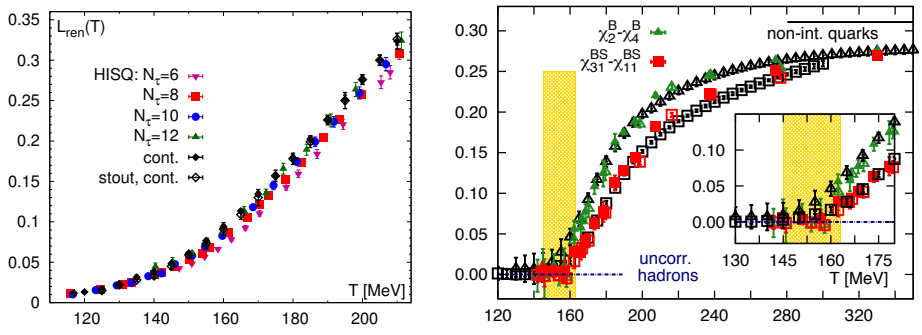


Fig. 7. (Left) The renormalized Polyakov loop in (2+1)-flavor QCD.[96] (Right) Appearance of the fractionally charged degrees of freedom in the chiral crossover region $T_c = 154(9)$ MeV (shaded region) for the light as well as the strange quark. The black points show results obtained using the stout action[97] and the other points have been obtained using the HISQ action.[98]

Deconfinement is associated with the liberation of degrees of freedom, manifested by a rapid rise in the bulk thermodynamic observables such as the pressure, energy density etc. Among such bulk thermodynamic observables fluctuations and correlations of different conserved quantum numbers, e.g. the baryon number (B), electric charge (Q) and strangeness (S), directly probe the liberation of the quark degrees of freedom and the consequent appearance of fractionally charged quantum number carriers. For example, both for an uncorrelated hadron gas and in a free quark gas the difference of second to fourth order cumulants of baryon number fluctuations probes the baryon number of degrees of freedom, specifically $\chi_2^B - \chi_4^B \propto B^2 - B^4$. For hadronic degrees of freedom carrying baryon number $B = \pm 1$ one thus has $\chi_2^B - \chi_4^B = 0$, but for quark-like degrees of freedom with $B = \pm 1/3$ one finds $\chi_2^B - \chi_4^B \neq 0$. Similarly, for the strange quark sector higher order baryon-strangeness correlation such as $\chi_{31}^{BS} - \chi_{11}^{BS} \propto (B^3 - B)S$ is non-vanishing if the strangeness carrying degrees of freedom are associated with quark-like baryon number $B = \pm 1/3$ and vanishes when the strangeness is carried by hadronic degrees of freedom with $B = \pm 1$. Thus, such combinations of higher order fluctuations and correlations of quantum numbers are sensitive probes of appearance of fractionally charged degrees of freedom in a deconfined medium.[98–100] The right hand panel of Fig. 7 shows lattice QCD results for $\chi_2^B - \chi_4^B$ and $\chi_{31}^{BS} - \chi_{11}^{BS}$ from the BNL-Bielefeld collaboration[98] as well as the Budapest-Wuppertal collaboration.[97] Clearly, both quantities start deviating strongly from zero in the chiral crossover region, $T_c = 154(9)$ MeV, indicating that fractionally charged degrees of freedom start to appear at these temperatures and onset of deconfinement takes place for the light as well as the strange quarks. Note, however, that also these fluctuation observables are not order parameters in the strict sense.

3.3. *Axial symmetry of QCD at high temperature*

Although, the axial $U_A(1)$ symmetry is not an exact symmetry of QCD, as mentioned before, the magnitude of its breaking is expected to influence the order of the chiral phase transition. Hence, knowledge of the temperature dependence of the $U_A(1)$ breaking is essential for a comprehensive understanding of the QCD chiral transition. The axial $U_A(1)$ symmetry of the massless QCD Lagrangian is broken due to quantum fluctuations, resulting in non-conservation of axial current[101,102] as well as explicit breaking of the global $U_A(1)$ symmetry induced by topologically non-trivial gauge field configurations, such as the instantons.[103] Due to color screening the instanton density gets suppressed as the temperature increases[104] and in the $T \to \infty$ limit the $U_A(1)$ symmetry becomes exact.

Since $U_A(1)$ is not an exact symmetry of QCD one cannot define an order parameter associated with its breaking. However, for two massless flavors, the pion (π) and the iso-vector scalar δ (a_1) mesons transform into each other under a $U_A(1)$ rotation. Since the presence of an exact $U_A(1)$ will render these meson states degenerate, the difference of the integrated two-point correlation functions of pion and δ

meson,

$$\chi_\pi - \chi_\delta = \int d^4x \left(\langle \pi^+(x)\pi^-(0)\rangle - \langle \delta^+(x)\delta^-(0)\rangle \right) , \tag{37}$$

will also vanish in the limit of exact $U_A(1)$ symmetry. Corrections due to small non-vanishing light quark masses will only contribute at $\mathcal{O}(m_l^2)$. Thus, this quantity can be taken as a measure of the $U_A(1)$ breaking.[105]

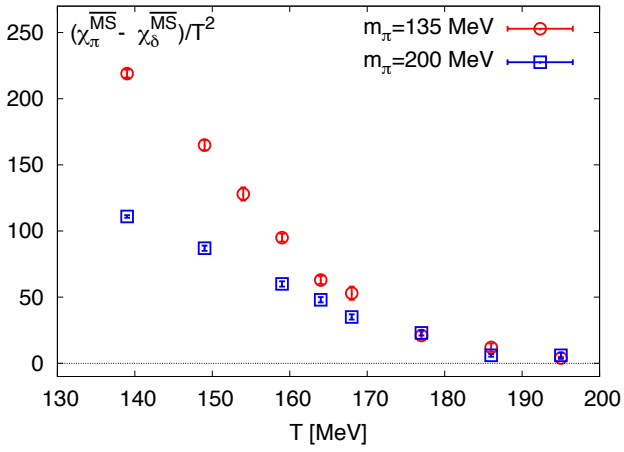


Fig. 8. The $U_A(1)$ breaking measure $\chi_\pi - \chi_\delta$ renormalized in the $\overline{\rm MS}$ scheme as function of temperature. Results are from a calculation with Domain Wall fermions.[61] The difference is non-vanishing for $T \geq T_c = 154(9)$ MeV. It becomes independent of quark mass for $T \gtrsim 168$ MeV and rises with decreasing quark mass at lower temperature. In fact, it will diverge in the chiral limit for $T < T_c$.

This measure of $U_A(1)$ breaking was studied in detail using improved p4 staggered fermions,[106] and it was found that $\chi_\pi - \chi_\delta$ remains non-vanishing for $T \lesssim 1.2T_c$. However, for staggered fermions the issue of axial anomaly is quite subtle and the correct anomaly may only emerge in the continuum limit.[107,108] On the other hand, emergence of the axial anomaly is more straightforward for the chiral DWF formulation.[49] For DWF, axial symmetry is broken by the same topologically non-trivial configurations as in the continuum. Lattice artifacts appear only at $\mathcal{O}(m_{\rm res}^2)$, due to the explicit chiral symmetry breaking residual mass,[56] $m_{\rm res}$, arising from finiteness of the fifth dimension ($L_s < \infty$). Thus, the DWF action turns out to be a natural candidate for investigation of the temperature dependence of $U_A(1)$ breaking in QCD. The temperature dependence of the $U_A(1)$ breaking measure, $\chi_\pi - \chi_\delta$, has been extensively studied using the DWF formalism for several volumes as well as quark masses.[59,61,109] As depicted in Fig. 8, calculations with DWF clearly show that $\chi_\pi - \chi_\delta$ does not vanish around the chiral crossover temperature T_c and remains non-vanishing for 165 MeV $\lesssim T \lesssim$ 195 MeV, independent of the light quark masses. These results indicate that $U_A(1)$ symmetry

may remain broken at these temperatures even in the chiral limit.

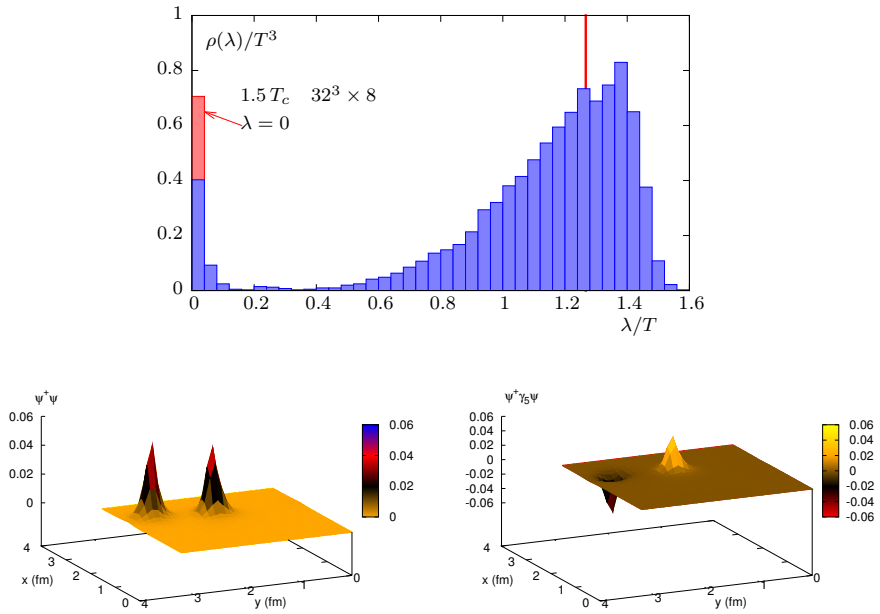


Fig. 9. (Top) Accumulation of near-zero eigenmodes of the Overlap-Dirac fermion matrix at $T = 1.5T_c$.[62] (Bottom) Spatial profile of a typical near-zero mode (left) and the spatial profile of the chirality of the same near-zero mode (right) at $T = 1.5T_c$.[62]

Since $U_A(1)$ breaking arises due to topology of the gauge fields, it is intimately related to the infrared modes of the Dirac fermions. In the limit of infinite volume, both the chiral order parameter, $\langle\bar{\psi}\psi\rangle_l$, and the $U_A(1)$ breaking measure, $\chi_\pi - \chi_\delta$, can be represented in terms of the eigenvalue density, $\rho(\lambda)$, of the Dirac fermions

$$\langle\bar{\psi}\psi\rangle_l = \int_0^\infty d\lambda \, \frac{2m_l\,\rho(\lambda)}{\lambda^2 + m_l^2} \,, \qquad \text{and} \qquad \chi_\pi - \chi_\delta = \int_0^\infty d\lambda \, \frac{4m_l^2\,\rho(\lambda)}{(\lambda^2 + m_l^2)^2} \,. \tag{38}$$

In the chiral symmetric phase and in the chiral limit $\langle\bar{\psi}\psi\rangle_l$ must vanish, but $\chi_\pi - \chi_\delta$ can remain non-zero. Identification of the infrared fermionic modes, i.e. the form of $\rho(\lambda)$, that give rise to such a phenomenon naturally leads to the underlying non-perturbative mechanism of axial symmetry breaking. Studies with DWF[59,109] as well as with overlap fermions,[62] possessing even better chiral properties and an exact index theorem, suggest that an accumulation of near-zero eigenmodes of the form $\rho(\lambda) \sim m_l^2\delta(\lambda)$ may largely account for the observed $U_A(1)$ breaking in $\chi_\pi - \chi_\delta$ at high temperature. Such accumulation of the near-zero modes are depicted in Fig. 9 (top). More detailed studies[62] of the space-time profiles, as illustrated in Fig. 9 (bottom), localization properties and distributions of these near-zero modes indicate

that their behavior is consistent with underlying presence of a dilute instanton gas—a gas of widely separated, weakly interacting, small instantons and anti-instantons. This suggests that even at temperatures $T \sim 1.5T_c$ weakly interacting instanton anti-instanton pairs are largely responsible for the $U_A(1)$ breaking.

The analysis of $U_A(1)$ symmetry breaking close to the chiral limit of 2 or (2+1)-flavor QCD, however, is far from being settled. Detailed systematic studies of the quark mass and volume dependence as well as the cut-off dependence are still missing. Moreover, results obtained with chiral fermions are still controversial. Calculations performed with dynamical overlap fermions[60,110] and so-called optimal domain wall fermions[111] at present suggest that $U_A(1)$ does get restored already at T_c, which would still allow for the occurrence of a first order transition when approaching the chiral limit.

4. Bulk thermodynamics

4.1. *The QCD equation of state at vanishing chemical potential*

Lattice QCD calculations of the equation of state, or more general, of basic bulk thermodynamic observables like the pressure (P), energy density (ϵ) or entropy density (s), have reached now a precision where continuum extrapolated results for physical light and strange quark masses can be obtained. This also allows detailed comparisons with perturbative calculations at high temperature and model calculations at low temperature.

The procedure to calculate bulk thermodynamic observables in lattice QCD is well established. The starting point for these calculations is the evaluation of the trace anomaly, $\Theta^{\mu\mu}(T) \equiv \epsilon - 3P$. The trace anomaly is directly obtained as a temperature derivative of P/T^4 which also is related to the QCD partition function, $Z(T,V)$,

$$\frac{\epsilon - 3P}{T^4} = T\frac{\mathrm{d}P/T^4}{\mathrm{d}T} \ , \tag{39}$$

with $P/T^4 = \lim_{V\to\infty}(VT^3)^{-1} \ln Z(T,V)$. As the trace anomaly arises as a derivative of the logarithm of the QCD partition function with respect to temperature, it can be expressed in terms of expectation values of rather simple observables, e.g. a combination of the gauge action and light and strange quark chiral condensates. Nonetheless, the calculations become rather time consuming because a subtraction of the zero temperature contributions is needed to eliminate divergent vacuum contributions[c].

As can be seen from Eq. 39 up to an integration constant at a temperature T_0 the pressure can be obtained from the trace anomaly,

$$\frac{P(T)}{T^4} - \frac{P(T_0)}{T_0^4} = \int_{T_0}^{T} \mathrm{d}T' \frac{\epsilon - 3P}{T'^5} \ . \tag{40}$$

[c]For more details we refer, for instance, to Ref. 112.

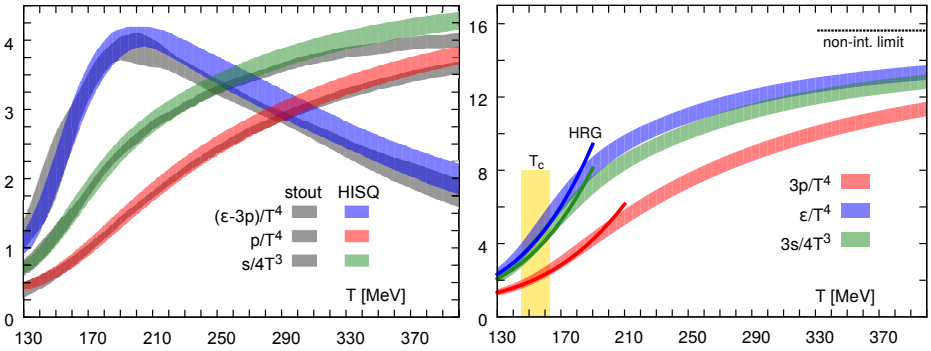


Fig. 10. (Left) Comparison of the trace anomaly $(\epsilon - 3P)/T^4$, pressure and entropy density calculated with the HISQ (colored)[114] and stout (grey)[113] discretization schemes for staggered fermions. (Right) Continuum extrapolated results for pressure, energy density and entropy density obtained with the HISQ action.[114] Solid lines on the low temperature side correspond to results obtained from hadron resonance gas (HRG) model calculations. The dashed line at high temperatures shows the result for a non-interacting quark-gluon gas.

This allows to reconstruct the energy density as well as the entropy density $s/T^3 = (\epsilon + P)/T^4$.

The determination of thermodynamic quantities in QCD is a parameter free calculation. All input parameters needed in the calculation, e.g. the quark masses ($m_u = m_d,\ m_s$) and the relation between the lattice cut-off, a, and the bare gauge coupling, $\beta = 6/g^2$, are determined through calculations at zero temperature. Likewise, there is only a single independent thermodynamic observable that is calculated in a lattice QCD calculation, for instance the trace anomaly, $\Theta^{\mu\mu}(T)$. All other bulk thermodynamic observables are obtained from $\Theta^{\mu\mu}(T)$ through standard thermodynamic relations. In Fig. 10 (left) we show recent results for the trace anomaly of (2+1)-flavor QCD[113,114] obtained with two different discretization schemes by two different groups. The results are extrapolated to the continuum limit and are obtained with a strange quark mass tuned to its physical value and light quark masses that differ slightly ($m_s/m_l = 27$[113] and 20[114]). The right hand panel in this figure shows results for the pressure, energy density and entropy density obtained from the trace anomaly by using Eqs. 39 and 40.

Also shown in Fig. 10 are results obtained from a hadron resonance gas (HRG) model calculation of bulk thermodynamics. As can be seen this describes the QCD equation of state quite well also in the transition region, although it may be noted that the HRG calculations yield results for all observables that are at the lower error band of the current QCD results. It has been speculated that this may indicate contributions from additional, experimentally not yet observed resonances which could contribute to the thermodynamics.[115] Indeed evidence for the contribution of a large number of strange baryons has recently been found in lattice QCD calculations of conserved charge fluctuations[116] (see also the discussion in Section 5 and 7).

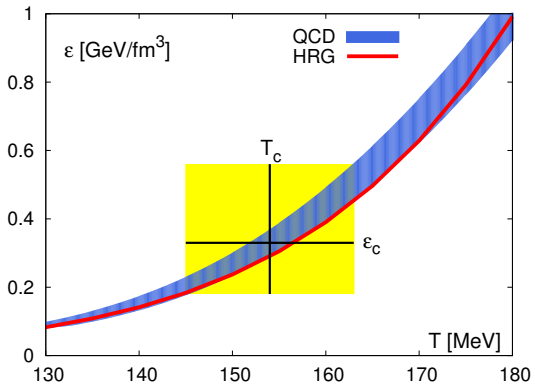


Fig. 11. The critical energy density ϵ_c in (2+1)-flavor QCD. The band gives the continuum extrapolated result for the energy density taken from Ref. 114. The HRG curve is based on all resonance with mass less than 2.5 GeV listed by the Particle Data Group.[31]

In Fig. 11 we show the energy density in the low temperature region. The box highlights the transition region characterized by the crossover temperature, $T_c = (154 \pm 9)$ MeV. From this we deduce the energy density in the crossover region, $\epsilon_c = (0.34 \pm 0.16)$ GeV/fm^3. This is a rather small value for the energy density needed to convert ordinary hadronic matter into a medium made up from quarks and gluons. It may be compared to the energy density of ordinary nuclear matter, $\epsilon^{\text{nuclear matter}} \simeq 0.15$ GeV/fm^3 or the energy density inside a nucleon, $\epsilon^{\text{nucleon}} \simeq 0.45$ GeV/fm^3, assuming the radius of nucleon $R_N \simeq 0.8$ fm. In fact, ϵ_c is close to the energy density reached in the dense packing limit of nucleons with radius R_N.

The simple bulk thermodynamic observables like pressure and energy density give the impression that an HRG model also provides a good description of the equation of state for temperatures above the crossover region, i.e. for $T \gtrsim 165$ MeV. However, as discussed in the previous section the analysis of conserved charge fluctuations clearly shows that at temperatures $T \gtrsim 160$ MeV thermodynamics can no longer be described in terms of hadronic degrees of freedom (see for instance Fig. 7 (right) and the discussion in Section 7). This also becomes evident in second order derivatives of the QCD partition function with respect to temperature. The speed of sound, $c_s^2 = \mathrm{d}p/\mathrm{d}\epsilon$, is related to the inverse of the specific heat, $C_V = \mathrm{d}\epsilon/\mathrm{d}T$,

$$c_s^2 = \frac{\mathrm{d}p}{\mathrm{d}\epsilon} = \frac{\mathrm{d}p/\mathrm{d}T}{\mathrm{d}\epsilon/\mathrm{d}T} = \frac{s}{C_V} \,, \tag{41}$$

$$\frac{C_V}{T^3} = \left.\frac{\partial \epsilon}{\partial T}\right|_V \equiv \left(4\frac{\epsilon}{T^4} + T\left.\frac{\partial(\epsilon/T^4)}{\partial T}\right|_V\right) . \tag{42}$$

Both quantities are shown in Fig. 12. The specific heat does not develop a pronounced peak in the transition region as one could have expected from pseudo-

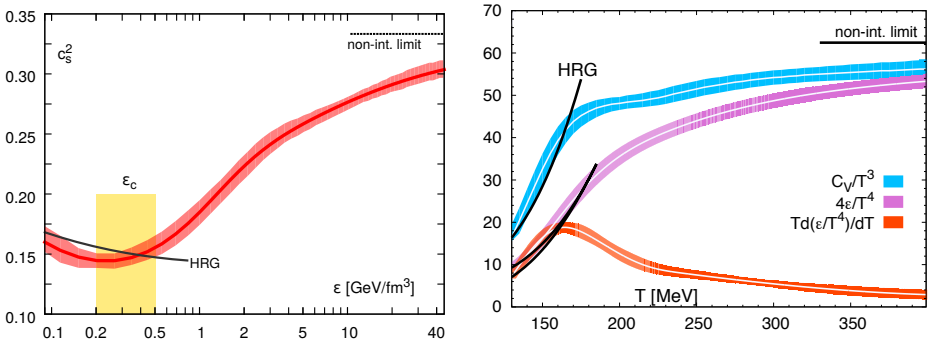


Fig. 12. The velocity of sound in (2+1)-flavor QCD (left) and the specific heat C_V/T^4 together with the two components (see Eq. 42) contributing to it (right). Solid black lines in the low and high temperature regions show the corresponding hadron resonance gas (HRG) and non-interacting quark-gluon gas results, respectively.

critical behavior of energy density fluctuations close to a critical point. This may be understood[114] from the temperature dependence of the two terms contributing to C_V/T^3. The dominant singular contribution arises from the temperature derivative of ϵ/T^4, which has a peak. This, however, is overwhelmed by the large energy density contribution at high temperature which reflects the liberation of many partonic degrees of freedom. Furthermore, even in the chiral limit, where QCD is expected to have a second order phase transition belonging to the universality class of 3-d, $O(4)$ symmetric spin models, the specific heat will not diverge as the relevant critical exponent $\alpha \simeq -0.2$ that controls its singular behavior, $C_V/T^3 \sim (|T - T_c|/T_c)^{-\alpha} + \text{const.}$, is negative for this universality class (see Table 1). The speed of sound will therefore stay non-zero at T_c also in the chiral limit.

4.2. *The QCD equation of state at non-vanishing chemical potential*

In Section 3 we have discussed lattice QCD results on the dependence of the QCD crossover temperature on the baryon chemical potential and its relation to the freeze-out temperatures determined in heavy ion experiments. These experiments, in particular the beam energy scan program performed at RHIC, will probe properties of strong-interaction matter at non-vanishing baryon chemical potential in the temperature range $0.9 \lesssim T/T_c \lesssim 2$ and $0 \lesssim \mu_B/T \lesssim 3$, with T_c denoting the crossover temperature at $\mu_B = 0$. For the hydrodynamic modeling of matter in this (T, μ_B) regime it thus is of importance to also know the equation of state at non-vanishing μ_B/T. As direct numerical calculations at non-zero μ_B are not yet possible, a viable approach is to analyze the equation of state using a Taylor expansion in terms of chemical potentials[117,118] as given in Eq. 18. In this way some results for the EoS at non-zero baryon chemical potential have already been obtained on coarse lattices.[40,41,118,119] Continuum extrapolated results for Taylor

expansion coefficients of the pressure at $\mathcal{O}(\mu_I^2)$ have been obtained.[120,121] These have been used to construct the EoS at $\mathcal{O}(\mu_B^2)$[122] which implements the strangeness neutrality constraint[119] ($\langle n_S \rangle = 0$) and the electric charge to baryon number relation ($\langle n_Q \rangle = 0.4 \langle n_B \rangle$) suitable for conditions met in heavy ion collisions.

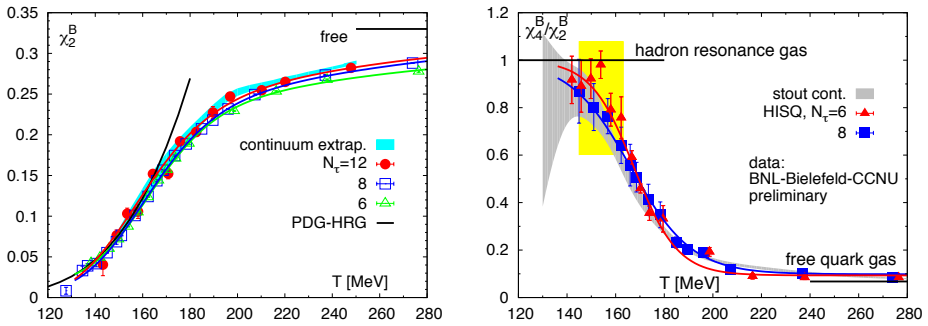


Fig. 13. Expansion coefficients of the pressure at non-zero baryon chemical potential. The left hand figure shows the leading order correction[121] and the right hand figure shows the relative contribution of the next to leading order correction. The continuum extrapolated result obtained with the stout action is taken from Ref. 123.

We will discuss here only the case $\mu_Q = \mu_S = 0$ in some detail in order to illustrate the relative importance of higher order corrections in different temperature and μ_B regions. The Taylor series for the pressure is given by,

$$\frac{P(T,\mu_B) - P(T,0)}{T^4} = \frac{1}{2}\chi_2^B(T)\left(\frac{\mu_B}{T}\right)^2 \left(1 + \frac{1}{12}\frac{\chi_4^B(T)}{\chi_2^B(T)}\left(\frac{\mu_B}{T}\right)^2\right) + \mathcal{O}(\mu_B^6)\,. \quad (43)$$

The leading order correction to the pressure thus is proportional to the quadratic fluctuations of net baryon number. The next to leading order corrections are proportional to the quartic fluctuations. When written in the form given in Eq. 43 it becomes easy to identify the relative importance of leading and next to leading order corrections. In Fig. 13 we show $\chi_2^B(T)$ (left) and $\chi_2^B(T)/\chi_4^B(T)$ (right). With increasing temperature the $\mathcal{O}(\mu_B^4)$ correction rapidly looses importance relative to the leading $\mathcal{O}(\mu_B^2)$ term.

In Fig. 14 we show preliminary results for the μ_B-dependent contribution to the total pressure evaluated for different values of μ_B/T and taking into account corrections up to $\mathcal{O}((\mu_B/T)^4)$.[124] These results suggests that an $\mathcal{O}((\mu_B/T)^4)$ Taylor expansion of the pressure (and energy density) is well controlled for all values of the chemical potential below $\mu_B/T = 2$. This covers a wide range of the QCD phase diagram accessible in the beam energy scan (BES) at RHIC, i.e. the region of beam energies $\sqrt{s} \geq 20$ GeV.

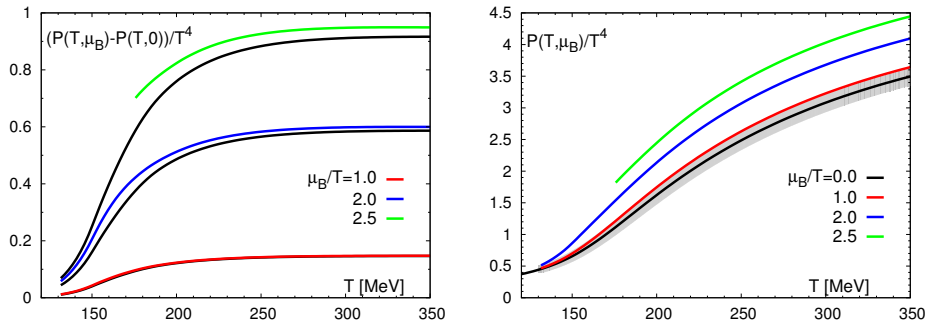


Fig. 14. (Left) The μ_B-dependent part of the pressure at $\mathcal{O}((\mu_B/T)^2)$ (black) and $\mathcal{O}((\mu_B/T)^4)$ (colored).[124] The latter is shown only in the temperature regime where neglected corrections at $\mathcal{O}((\mu_B/T)^6)$ are estimated to contribute less than 10%. (Right) When combined with the $\mu_B = 0$ contribution for the pressure shown in Fig. 10 these neglected terms contribute less than 3% to the total pressure.[124] The grey band gives the uncertainty on $P(T,0)/T^4$ and the central line in the band is the parametrization of $P(T,0)/T^4$ given in Ref. 114.

4.3. *Perturbation theory, hadron resonance gas and the strongly interacting liquid*

In our discussion of bulk thermodynamic observables we have compared with HRG model calculations. We have seen that the HRG does provide a rather good description of bulk thermodynamics below and even in the crossover region. However, the HRG does depend on the resonance spectrum used in the calculation. This is of some significance when one looks at more selective observables like, e.g., fluctuations and correlations of strange baryons (see Sections 5 and 7). Spectrum independent HRG results are, for instance, related to fluctuations of net baryon number. The ratio of fourth to second order net-baryon number cumulants shown in Fig. 13 (right) is unity in any HRG model irrespective of details of the spectrum. This figure thus shows that an HRG model calculation can be expected to provide a good description of QCD thermodynamics on a 10% level only at temperatures less than about $T \simeq (140 - 145)$ MeV.

At asymptotically high temperatures hard thermal loop, perturbative calculations[24] or dimensionally reduced QCD (EQCD)[125] provide a well-established framework for the analysis of bulk thermodynamics and fluctuations of conserved charges. We show in Fig. 15 a comparison of the trace anomaly (left) and the pressure (right) calculated in lattice QCD with HTL and EQCD calculations. These calculations seem to give a good description of bulk thermodynamics at temperatures $T \gtrsim 400$ MeV. However, even in this regime there remain differences between HTL and EQCD calculations that are of the order of 10%. Moreover, within the HTL calculations there seems to be no unique choice for the renormalization scale μ, that would allow to match all observables simultaneously. Similar conclusions can be drawn from the HTL analysis of net-baryon number fluctuations shown in Fig. 16 (right). Although observables that are dominated at high temperature by

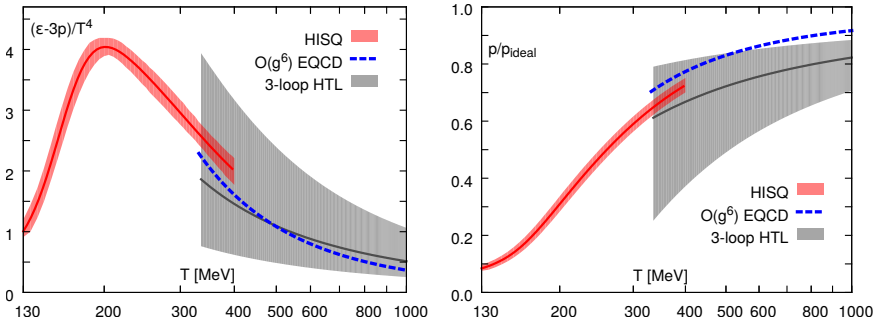


Fig. 15. Comparison of the (2+1)-flavor calculation[114] of the trace anomaly (left) and pressure (right) with HTL and EQCD (dashed line) calculations. The black line corresponds to the HTL calculation[24] with renormalization scale $\mu = 2\pi T$. Note that this solid line would move up for the trace anomaly and move down for the pressure if the scale μ in HTL is reduced.

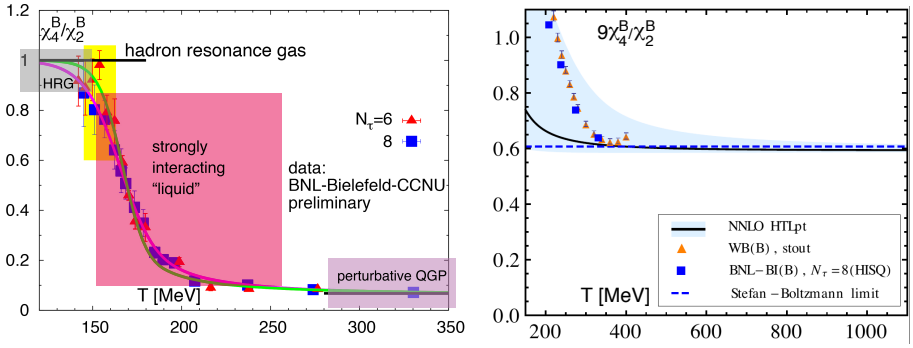


Fig. 16. The ratio of quartic and quadratic net-baryon number fluctuations versus temperature. The left hand panel shows temperature ranges in which HRG and resummed perturbative calculations, respectively, provide good approximations to lattice QCD results. The right hand panel shows the result from a HTL-resummed calculations.[24]

quark rather than gluon contributions seem to approach perturbative behavior earlier, it still is evident that agreement with lattice QCD results on the 10% level only is possible for $T \gtrsim (250-300)$ MeV. In general the temperature range $T_c \leq T \leq 2\,T_c$ is highly non-perturbative and obviously not accessible to hadronic model calculations. This is highlighted in the left hand panel of Fig. 16. We will discuss in the following sections properties of strong-interaction matter in this temperature range.

5. Fluctuations of conserved charges

Proximity of a second order criticality, such as the $O(4)$ chiral phase transition or the QCD critical point, is universally manifested through long-range correlations at all length scales, resulting in increased fluctuations of the order parameter.

These fluctuations can be quantified through the Gaussian (variance) as well as non-Gaussian (skewness, kurtosis *etc.*) cumulants of the distribution of the order parameter. Higher order non-Gaussian cumulants become increasingly sensitive to proximity of a critical point[100] which is reflected in their grows with higher powers of the correlation length.[126] Moreover, even qualitative features, such as the sign change and the associated non-monotonicity, of these non-Gaussian cumulants can encode the presence of a nearby critical region.[127–129] Non-Gaussian cumulants can be accessed in heavy-ion experiments via the event-by-event fluctuations of various conserved charges and particle multiplicities.[130–134] In this vein, a major focus of the Beam Energy Scan (BES) program[135] at the RHIC is measurements of the event-by-event fluctuations of particle multiplicities and conserved charges.[136–141]

Among several conserved charges, the net electric charge is of special interest. Cumulants of net electric charge fluctuations can be measured in experiments[138,141] and are calculable in lattice QCD.[120,121] Cumulants of net electric charge fluctuations and correlations with other conserved charges are well defined in lattice QCD at vanishing chemical potentials where standard lattice QCD techniques can be used to compute them. Furthermore, Taylor expansions in powers of μ_B around $\mu_B = 0$, can be employed to obtain generalized susceptibilities for $\mu_B > 0$,

$$\chi_n^Q\left(T,\mu_B\right) = \sum_{k=0}^{\infty} \frac{1}{k!}\, \chi_{kn}^{BQ}(T) \left(\frac{\mu_B}{T}\right)^k \,. \tag{44}$$

These susceptibilities directly relate to cumulants of the net electric charge fluctuations,

$$\begin{aligned}
\chi_1^Q\left(T,\mu_B\right) &= \frac{1}{VT^3}\left\langle N_Q\right\rangle \,, \\
\chi_2^Q\left(T,\mu_B\right) &= \frac{1}{VT^3}\left\langle \left(\delta N_Q\right)^2\right\rangle \,, \\
\chi_3^Q\left(T,\mu_B\right) &= \frac{1}{VT^3}\left\langle \left(\delta N_Q\right)^3\right\rangle \,, \\
\chi_4^Q\left(T,\mu_B\right) &= \frac{1}{VT^3}\left[\left\langle \left(\delta N_Q\right)^4\right\rangle - 3\left\langle \left(\delta N_Q\right)^2\right\rangle^2\right] \,,
\end{aligned} \tag{45}$$

where N_Q is the net (positive minus negative) charge and $\delta N_Q = N_Q - \langle N_Q\rangle$.

On the other hand, through the measurements of the event-by-event distributions of the net electric charge, heavy-ion experiments provide various cumulants, mean (M_Q), variance (σ_Q), skewness (S_Q), and kurtosis (κ_Q), of the electric charge fluctuations for given beam energy ($\sqrt{s}$)[138]

$$\begin{aligned}
M_Q\left(\sqrt{s}\right) &= \left\langle N_Q\right\rangle \,, & \sigma_Q^2\left(\sqrt{s}\right) &= \left\langle \left(\delta N_Q\right)^2\right\rangle \,, \\
S_Q\left(\sqrt{s}\right) &= \frac{\left\langle \left(\delta N_Q\right)^3\right\rangle}{\sigma_Q^3} \,, & \kappa_Q\left(\sqrt{s}\right) &= \frac{\left\langle \left(\delta N_Q\right)^4\right\rangle}{\sigma_Q^4} - 3 \,.
\end{aligned} \tag{46}$$

Thus, the charge susceptibilities obtained from lattice QCD calculations and the cumulants measured in the heavy-ion experiments are directly related to each other

through the appropriate volume-independent ratios[142]

$$\frac{M_Q\left(\sqrt{s}\right)}{\sigma_Q^2\left(\sqrt{s}\right)} = \frac{\chi_1^Q\left(T,\mu_B\right)}{\chi_2^Q\left(T,\mu_B\right)} \equiv R_{12}^Q \,, \tag{47a}$$

$$\frac{S_Q\left(\sqrt{s}\right)\sigma_Q^3\left(\sqrt{s}\right)}{M_Q\left(\sqrt{s}\right)} = \frac{\chi_3^Q\left(T,\mu_B\right)}{\chi_1^Q\left(T,\mu_B\right)} \equiv R_{31}^Q \,. \tag{47b}$$

As in many other cases, one still has to worry about directly confronting thermodynamic QCD calculations performed in equilibrium and in the thermodynamic limit to the rapidly expanding dense matter created in heavy ion collisions in a small volume. In the analysis of higher order cumulants additional complications may arise from more complicated efficiency corrections and the limited experimental acceptance windows.[143–145]

In heavy-ion collision experiments the only tunable parameter is the beam energy, $\sqrt{s}$. However, to gain access to the information regarding the QCD phase diagram this only tunable parameter needs to be related to the thermodynamic variables, e.g. temperature and baryon chemical potential. Traditionally, this $\sqrt{s} \leftrightarrow (T,\mu_B)$ mapping has been done by relying on the statistical hadronization model based analysis.[86] Recent advances in heavy-ion experiments as well as in lattice QCD calculations have placed us in a unique situation where, for the first time, this mapping can now be obtained through direct comparisons between the experimental results and rigorous (lattice) QCD calculations. Recently, it has been shown[142,146] that by directly comparing lattice QCD calculations for R_{31}^Q (Eq. 47b) and R_{12}^Q (Eq. 47a) with their corresponding cumulant ratios measured in heavy-ion experiments it is possible to extract the thermal parameters, namely the freeze-out temperature, T^f, and the freeze-out baryon chemical potential μ_B^f. The feasibility of such a procedure has been demonstrated in Refs. 123,147,148. Fig. 17[149] illustrates a recent example of such a comparison and subsequent determination of the freeze-out parameters.

As can be seen from Fig. 17, due to large errors on the experimental results for $(S_Q\sigma_Q^3)/M_Q$, at present, only an upper limit on the freeze-out temperature can be determined using the method described above. Thus, a complementary procedure for the determination of T^f, relying on a separate observable that can be extracted both from heavy-ion experiments and lattice QCD calculations, is certainly welcome. Recently, such a complementary procedure for the determination of T^f has been proposed in Ref. 116. This procedure takes advantage of the fact that the initially colliding nuclei in heavy-ion collisions are free of net strangeness. Thus, the conservation of strangeness under strong interaction ensures that the QGP medium created during the collisions of these heavy-ions is also strangeness neutral.

By Taylor expanding the net strangeness density, $\langle n_S\rangle\left(\mu_B,\mu_S\right)$, in μ_B and μ_S and subsequently imposing the strangeness neutrality condition, $\langle n_S\rangle\left(\mu_B,\mu_S\right)=0$, for a homogeneous thermal medium the strangeness chemical potential, μ_S, can be

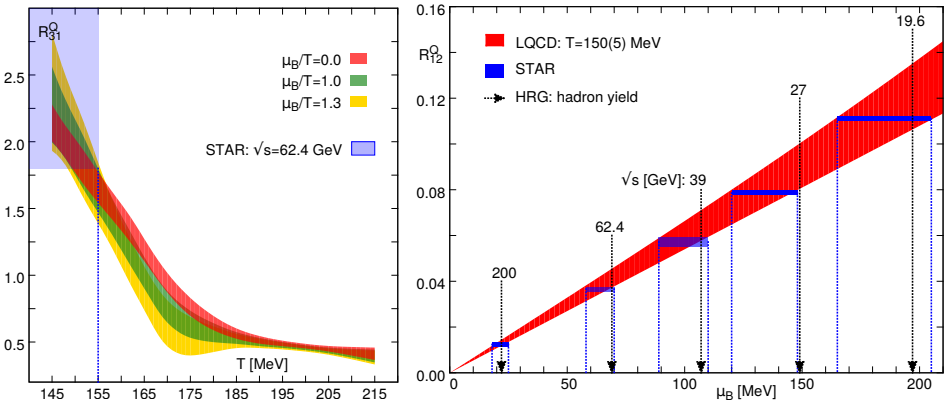


Fig. 17. (Left) A comparison between the lattice QCD results[149] for R_{31}^Q and the STAR data[138] for $(S_Q\sigma_Q^3)/M_Q$ at $\sqrt{s} = 62.4$ GeV. The overlap of the experimental results with the lattice QCD calculations provides an upper bound on the freeze-out temperature $T^f \leq 155$ MeV. (Right) Lattice QCD results[149] for R_{12}^Q as a function of μ_B compared with the STAR data[138] for M_Q/σ_Q^2 in the temperature range $T^f = 150(5)$ MeV. The overlap regions of the experimentally measured results with the lattice QCD calculations provide estimates for the freeze-out chemical potential μ_B^f for a given $\sqrt{s}$. The arrows indicate the corresponding values of μ_B^f obtained from the statistical hadronization model fits to experimentally measured hadron yields.[86]

obtained as[116]

$$\frac{\mu_S}{\mu_B} = s_1(T) + s_3(T)\left(\frac{\mu_B}{T}\right)^2 + \mathcal{O}\left[\left(\frac{\mu_B}{T}\right)^4\right] . \tag{48}$$

The coefficients s_1, s_3, etc. consist of various generalized baryon, charge and strangeness susceptibilities defined at vanishing chemical potentials and can be calculated through standard lattice QCD computations at zero chemical potentials.[116] Fig. 18 (left) shows the leading order contribution to μ_S/μ_B, *i.e.* $s_1(T)$. A comparison of the lattice result with the predictions from the hadron resonance gas model reveal that the inclusion of only experimentally observed hadrons, as listed by the Particle Data Group,[31] fails to reproduce the lattice results around the crossover region. Note that, while μ_S/μ_B is unique in QCD, for a hadron gas it depends on the relative abundances of the open strange baryons and mesons. For fixed T and μ_B, a strangeness neutral hadron gas having a larger relative abundance of strange baryons over open strange mesons naturally leads to a larger value of μ_S. Astonishingly, the inclusion of additional, unobserved strange hadrons predicted within the quark model[150,151] provides a much better agreement with lattice results, hinting that these additional hadrons become thermodynamically relevant close to the crossover temperature.[116] As will be discussed in Section 7 , other lattice thermodynamics studies also indicate that additional, unobserved charm hadrons do become thermodynamically relevant close to the QCD crossover.[152]

On the other hand, the experimentally measured yields of the strangeness S

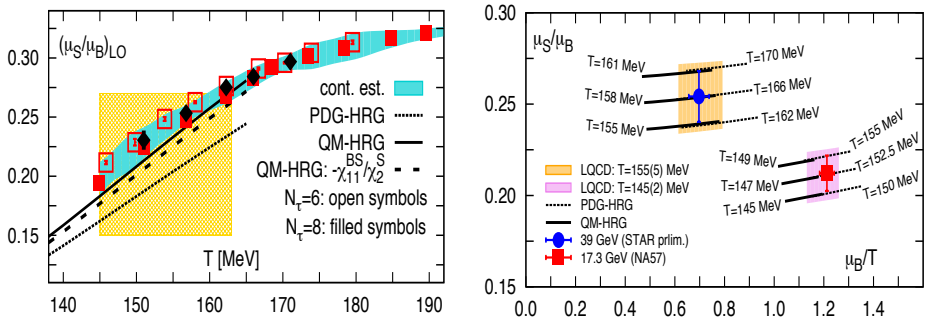


Fig. 18. (Left) Lattice QCD results[116] for μ_S/μ_B at the leading order, i.e. $s_1(T)$ (see Eq. 48). The dotted line (PDG-HRG) shows the results of a hadron resonance gas model containing only hadrons listed by the Particle Data Group.[31] The solid line (QM-HRG) depicts the result for a hadron gas when additional, experimentally yet unobserved, quark model predicted strange hadrons[150,151] are included. The shaded region indicates the chiral crossover region $T_c = 154(9)$ MeV. (Right) A comparison between experimentally extracted values of $(\mu_S^f/\mu_B^f, \mu_B^f/T^f)$ (filled symbols) and lattice QCD results for μ_S/μ_B (shaded bands).[116] The lattice QCD results are shown for $\mu_B/T = \mu_B^f/T^f$. The temperature range where lattice QCD results match with μ_S^f/μ_B^f provide the values of T^f, i.e. $T^f = 155(5)$ MeV and 145(2) MeV for $\sqrt{s} = 39$ GeV and 17.3 GeV, respectively.

anti-baryon to baryon ratios, R_H, at the freeze-out are determined by the thermal freeze-out parameters (T^f, μ_B^f, μ_S^f),[86]

$$R_H(\sqrt{s}) = \exp\left[-\frac{2\mu_B^f}{T^f}\left(1 - \frac{\mu_S^f}{\mu_B^f}|S|\right)\right] . \tag{49}$$

By fitting the experimentally measured values of R_Λ, R_Ξ and R_Ω, corresponding to $|S| = 1, 2$ and 3, the values of μ_S^f/μ_B^f and μ_B^f/T^f, as 'observed' in a heavy-ion experiment at a given $\sqrt{s}$, can easily be extracted. Matching these experimentally extracted values of μ_S^f/μ_B^f with the lattice QCD results for μ_S/μ_B as a function of temperature, one can determine the freeze-out temperature T^f. Fig. 18 (right) illustrates this procedure. Once again, the inclusion of additional unobserved strange hadrons in the hadron resonance gas model (QM-HRG) leads to very similar values of the freeze-out temperatures as obtained using the lattice data. However, including only the hadrons listed by the Particle Data Group[31] (PDG-HRG) yields freeze-out temperatures that are 5-8 MeV larger.

6. Transport properties

As we have seen in previous sections the analysis of bulk thermodynamics and charge fluctuations provides plenty of evidence that thermodynamics of strong-interaction matter above the crossover transition temperature, T_c, and up to temperatures of about $(1.5 - 2)T_c$ is highly non-perturbative. In this temperature range the

velocity of sound is significantly smaller than that in a non-interacting quark gluon gas suggesting also significant modifications of its transport properties. One of the striking results of heavy-ion experiments at RHIC and LHC is that strong-interaction matter in this temperature range shows features of a strongly coupled medium with a small shear viscosity to entropy density ratio and small diffusion coefficients. This led to the notion of strong-interaction matter close to the crossover transition being a 'nearly perfect liquid'.

Transport properties of strong-interaction matter can be explored in lattice QCD calculations through the analysis of current-current correlation functions, e.g. for some current $J(\tau, \vec{x})$,

$$G_J^{\alpha\beta}(\tau, \mathbf{p}) = \int \mathrm{d}^3x \; \mathrm{e}^{i\mathbf{px}} \langle J^\alpha(0,0) J^{\beta\dagger}(\tau, \mathbf{x}) \rangle = \int_0^\infty \frac{\mathrm{d}\omega}{2\pi} \, \rho_J^{\alpha\beta}(\omega, \mathbf{p}) \, K(\omega, \tau), \qquad (50)$$

where the integration kernel $K(\omega, \tau)$ is

$$K(\omega, \tau) = \frac{\cosh(\omega(\tau - 1/2T))}{\sinh(\omega/2T)} \; , \qquad (51)$$

and α, β are appropriately chosen (scalar, vector, tensor) indices specifying the current.

In Euclidean space-time these correlation functions have a spectral representation. The low frequency and low momentum structure of the spectral functions $\rho_J^{\alpha\beta}(\omega, \mathbf{p})$ then gives access to transport properties of strong-interaction matter while at higher frequencies the spectral functions provide information on in-medium properties of bound states. We will discuss the latter in the Section 7. Extracting the spectral function from a Euclidean correlation function is, however, difficult. This is due to the fact that Euclidean correlation functions are calculated in finite temperature lattice QCD only at a few discrete Euclidean time separations, e.g. $0 \leq \tau \leq N_\tau$ [d]. It requires the application of inversion methods like the Maximum Entropy Method (MEM)[153] or a modeling of the structure of the spectral function at low frequencies.

According to the Kubo relations, which express the response of a medium to small perturbations, transport coefficients can be determined from spectral functions calculated in equilibrium thermodynamics. They are given by the slope of the corresponding spectral functions at vanishing energy. For instance, using in Eq. 50 the electromagnetic current $J^\mu(t, \mathbf{x}) \equiv J_V(t, \mathbf{x}) = \bar{\psi}(t, \mathbf{x}) \gamma^\mu \psi(t, \mathbf{x})$ for a fermionic charge carrier (quarks) with charge e (e.g. $Q_d = -e/3$ for a down quark) one can extract the electrical conductivity σ which quantifies the response of the QGP to small perturbations induced by an electromagnetic field,

$$\sigma = \frac{C_{em}}{6} \lim_{\omega \to 0} \lim_{\mathbf{p} \to 0} \sum_{i=1}^{3} \frac{\rho^{ii}(\omega, \mathbf{p}, T)}{\omega} \; . \qquad (52)$$

[d]Note that Eq. 51 is symmetric around $\tau = 1/2T$ and as a consequence only half the number of data points of the Euclidean temporal correlation function, i.e. $N_\tau/2$, provide independent information to extract the spectral function.

Here C_{em} is the sum of the square of the elementary charges of the quark flavor f, $C_{em} = \sum_f Q_f^2$. The electrical conductivity and the vector spectral function are also related to the emission rate of soft thermal photons,

$$\lim_{\omega\to 0} \omega \frac{\mathrm{d}R_\gamma}{\mathrm{d}^3 p} = \frac{3}{2\pi^2}\,\sigma(T)\,T\,\alpha_{em}\ . \tag{53}$$

and the contribution of quark-antiquark annihilation to the thermal dilepton rate,

$$\frac{\mathrm{d}W}{\mathrm{d}\omega\,\mathrm{d}^3\mathbf{p}} = \frac{5\alpha_{em}^2}{54\pi^3}\frac{1}{\omega^2(e^{\omega/T}-1)}\,\rho_V(\omega,\mathbf{p},T), \tag{54}$$

where α_{em} is the electromagnetic fine structure constant.

Using the vector current $J_V(\tau,\mathbf{x})$ for heavy quarks one obtains from Eq. 50 the corresponding spectral function of heavy quarkonium in the vector channel, ρ_V^{ii}, which allows to determine the heavy quark diffusion coefficient D,

$$D = \frac{1}{6\chi_2^h}\lim_{\omega\to 0}\lim_{\mathbf{p}\to 0}\sum_{i=1}^{3}\frac{\rho_V^{ii}(\omega,\mathbf{p},T)}{\omega}. \tag{55}$$

Here χ_2^h is the heavy quark number susceptibility which is defined through the zeroth component of the temporal meson correlator in the vector channel. E.g., for charm quarks this is just the net charm number susceptibility introduced in Eq. 12. Similarly, in the light quark sector, the electric charge diffusion coefficient D_Q is defined as the ratio of σ to electric charge susceptibility χ_2^Q defined in Eq. 19, i.e. $D_Q = \sigma/\chi_2^Q$.

The heavy quark diffusion coefficient D can be related to the momentum diffusion coefficient κ and drag coefficient η through the Einstein relation

$$D = \frac{2T^2}{\kappa} = \frac{T}{M\eta}\ . \tag{56}$$

It is used to describe the Brownian motion of a heavy quark in the hot medium and can also be related to the ratio of shear viscosity over entropy density η/s.[154]

The shear (η) and bulk (ζ) viscosities of strong-interaction matter are extracted from correlation functions of the energy-momentum tensor, $T^{\mu\nu} = F^{\mu\alpha}F^{\nu\alpha} - \frac{1}{4}\delta_{\mu\nu}F^{\rho\sigma}F^{\rho\sigma}$. I.e. using the current $J^{\mu\nu}(\tau,\mathbf{x}) \equiv T^{\mu\nu}(t,\mathbf{x})$ in Eq. 50 one obtains

$$\eta = \pi\lim_{\omega\to 0}\lim_{\mathbf{p}\to 0}\frac{\rho^{12,12}(\omega,\mathbf{p})}{\omega}\ , \tag{57}$$

$$\zeta = \frac{\pi}{9}\lim_{\omega\to 0}\lim_{\mathbf{p}\to 0}\sum_{k,l}\frac{\rho^{kk,ll}(\omega,\mathbf{p})}{\omega}\ . \tag{58}$$

At present only a few calculations of transport coefficients have been performed in QCD with dynamical quark degrees of freedom. Most calculations utilized the quenched approximation at vanishing baryon number density.[155] In the following subsections we will summarize current results for the transport coefficients introduced above. For further details on the calculation of transport coefficients on the lattice and earlier results see, for instance, Ref. 156.

6.1. *Electrical conductivity, charge diffusion and dilepton rates*

Probably the best analyzed spectral function is that of the light quark vector current which gives access to the electrical conductivity, $\sigma(T)$ (Eq. 52), soft photon emission rates (Eq. 53) and thermal dilepton rates (Eq. 54) as well as the electric charge diffusion constant $D_Q = \sigma/\chi_2^Q$. The vector spectral function $\rho_V(\omega) \equiv \rho_V(\omega, 0, T)$ has been calculated first in quenched QCD[157] using the MEM approach[153,158] in which the analysis had only been constrained at large frequencies through a default model based on the free fermion spectral function and the largest lattices used only had $N_\tau = 16$ points in the temporal direction. It has, however, been noticed[159] that this is not sufficient to get access to transport coefficients, which require the spectral functions at low frequencies to be linear in ω. Furthermore, a larger time extent[160] is needed to control the low frequency part of the spectral functions.

First continuum extrapolated results for the vector spectral function were obtained in quenched QCD using clover-improved Wilson fermions[160] at $T \simeq 1.4\ T_c$. These results have been extended to three different temperatures recently.[161–163] In these calculations the thermal spectral functions are obtained by fitting the continuum-extrapolated two-point Euclidean correlation functions to an ansatz for the spectral function that is motivated by kinetic theory and perturbation theory

$$\rho^{model}(\omega) = \chi_q c_{BW} \frac{\omega\Gamma}{\omega^2 + \Gamma^2/4} + \frac{3}{2\pi}(1+k)\,\omega^2 \tanh\left(\frac{\omega}{4T}\right) . \qquad (59)$$

Here χ_q is similar to χ_2^h appearing in Eq. 55 but for light quarks and it is obtained by summing the zeroth component of the light temporal vector correlation function over space-time coordinates. The unknown parameters are thus the amplitude c_{BW} and the width Γ of the Breit-Wigner function as well as the parameter k, which parametrizes deviations from the free theory behavior at large ω. The thermal spectral functions obtained in this way and the resulting thermal dilepton rates are shown in Fig. 19. In the high frequency region, i.e. for $\omega/T \gtrsim 7$, all the thermal spectral functions at the three temperatures above T_c are well described by leading order perturbation theory (Born rate) as well as Hard Thermal Loop (HTL) calculations. At small frequencies the lattice QCD results are significantly enhanced over the Born rate, indicating the presence of a transport peak, but are smaller than the HTL rates. In fact, the latter rises too rapidly at low frequency and would give rise to a divergent electrical conductivity.

The finite intercept of $\rho(\omega)/(\omega T)$ at $\omega = 0$ seen in Fig. 19 gives the electrical conductivity (see Eq. 52), $\sigma/(C_{\rm em}T) \in [0.21, 0.44]$.[163] In these calculations σ/T does not show any significant temperature dependence[e], which may be due to the use of the quenched approximation. The results are consistent with a calculation that used staggered fermions, but no renormalized vector currents,[159] $\sigma/(C_{\rm em}T) \simeq 0.4(1)$ for $1.5 \lesssim T/T_c \lesssim 2.25$. These results are, however, substantially smaller than earlier calculations performed on coarse lattices.[164]

[e]This is also reflected in the temperature dependence of the temporal correlation functions divided

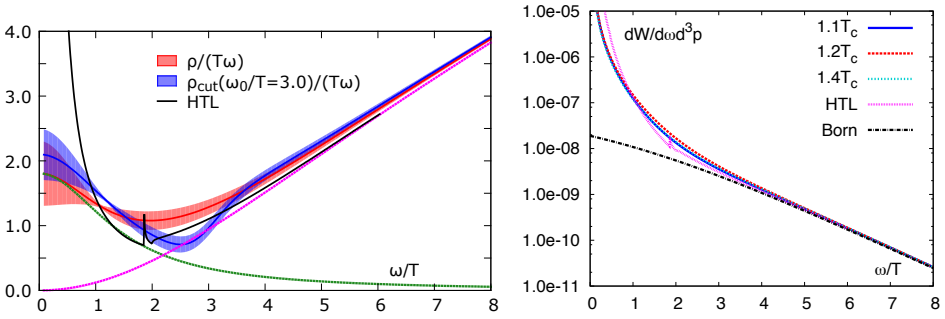


Fig. 19. (Left) Thermal spectral function at 1.1 T_c calculated in quenched QCD.[163] (Right) Temperature dependence of the quark-antiquark annihilation contribution to the thermal dilepton rate above T_c.[163]

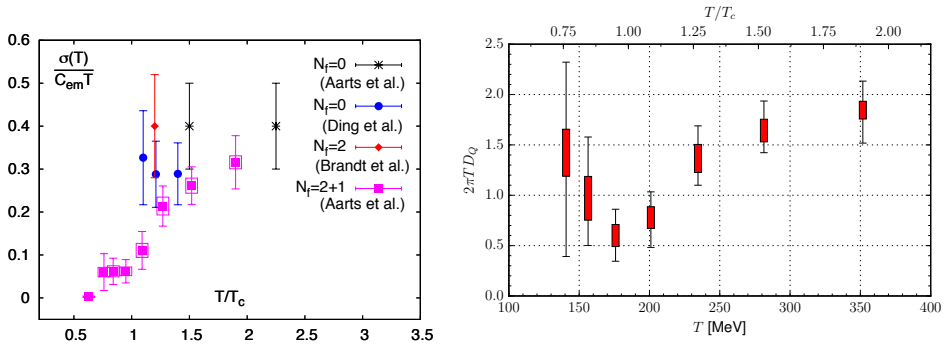


Fig. 20. (Left) Lattice QCD results for the electrical conductivity $\sigma/(C_{\rm em}T)$ as function of T/T_c including results obtained in quenched QCD,[159,160,163] 2-flavor QCD with $m_\pi \simeq 270$ MeV[165] and (2+1)-flavor QCD with $m_\pi \simeq 380$MeV.[166] Note that the values of T_c obtained in these calculations are different, i.e. $T_c^{N_f=0} \simeq 270$ MeV, $T_c^{N_f=2} \simeq 208$ MeV and $T_c^{N_f=2+1} \simeq 185$ MeV. (Right) Temperature dependence of charge diffusion coefficient $2\pi T D_Q = 2\pi T\sigma/\chi_2^Q$. The results are obtained in (2+1)-flavor QCD calculations on anisotropic lattices at one value of the spatial lattice cut-off, $a \simeq 0.12$ fm and with light quark masses corresponding to $m_\pi \simeq 380$ MeV.[166]

Recently the calculation of the electrical conductivity has also been performed in QCD with dynamical quarks. The first calculation was done in 2-flavor QCD using $\mathcal{O}(a)$ improved Wilson quarks corresponding to $m_\pi \simeq 270$ MeV. The electrical conductivity of the quark-gluon plasma at $T \simeq 250$ MeV was found to be similar to the quenched result, $\sigma/(C_{\rm em}T) = 0.40(12)$.[165]

First results from a calculation in (2+1)-flavor QCD performed on anisotropic lattices with quark masses corresponding to a pion mass $m_\pi \simeq 380$ MeV[166,167] are shown in Fig. 20. The simulation is performed at one value of the lattice cut-off.

by T^3 which are temperature independent for this temperature range.[163]

Varying the temporal extent of the lattice, N_τ, from between 48 and 16 a temperature range from 0.63 T_c to 1.90 T_c is covered. The left hand panel of this figure shows temperature dependence of $\sigma/(C_{\rm em}T)$ (square points). It stays constant within errors in the transition region and increases with temperature for $T > T_c$. Also shown in the left hand panel of Fig. 20 are electrical conductivities obtained in quenched QCD[159,160,163] and 2-flavor QCD.[165] The right hand panel of Fig. 20 shows the temperature dependence of charge diffusion coefficient D_Q multiplied by $2\pi T$. $2\pi T D_Q$ shows a dip near T_c which arises from the rapid exponential drop of the electric charge susceptibility at low temperature where the electrical conductivity of a pion gas[168] remains nonzero and vanishes only like $\sqrt{T}$.

6.2. *Heavy quark diffusion*

Contrary to earlier expectations it has been found in heavy ion collision experiments at RHIC[169,170] and LHC[171] that heavy-quark mesons show a substantial elliptic flow that is comparable to that of light-quark mesons. Moreover, also somewhat unexpectedly, heavy quarks are found to lose a significant amount of energy while traversing through the QGP. The latter has been called the heavy quark energy loss puzzle. Phenomenological explanations of these phenomena try to model the heavy quark diffusion in a hot and dense medium. This requires knowledge about the heavy quark diffusion coefficients D[154,172,173] which can be determined in lattice QCD calculations.

The charm-quark diffusion coefficient has been calculated in quenched QCD at three temperatures in the deconfined phase[174] using lattices with temporal extent $N_\tau = 48, 32$ and 24 at a fixed value of the cut-off. Results from this calculation are shown in Fig. 21. The left hand panel shows the transport peak in the charmonium vector spectral function at three different temperatures above T_c. These transport peaks are obtained using a MEM analysis where an ansatz of Lorentzian form is used as the prior information for the low frequency part of the spectral function, i.e. $\omega\eta/(\omega^2+\eta^2)$. The intercept at $\omega/T = 0$ gives the charm quark diffusion coefficient (c.f. Eq. 55). It is found that $2\pi TD \simeq 2$ and, with current understanding of uncertainties, this product is independent of temperature. These values of D are much smaller than the results from perturbative calculations[175] and are very close to the value obtained from the AdS/CFT correspondence.[176] These different results are compared in the right hand panel of Fig. 21.

A direct determination of the diffusion coefficient for bottom quarks from bottomonium correlation functions is difficult as it would require quite small lattice spacings to accommodate the bottomonium states on the lattice. The method of choice here is to start with the infinite quark mass limit where one can use Heavy Quark Effective Theory (HQEFT) to compute the diffusion coefficient of a static quark. In this approach the propagation of a heavy quark carrying color charge and its response to a colored Lorentz force can be described using linear response

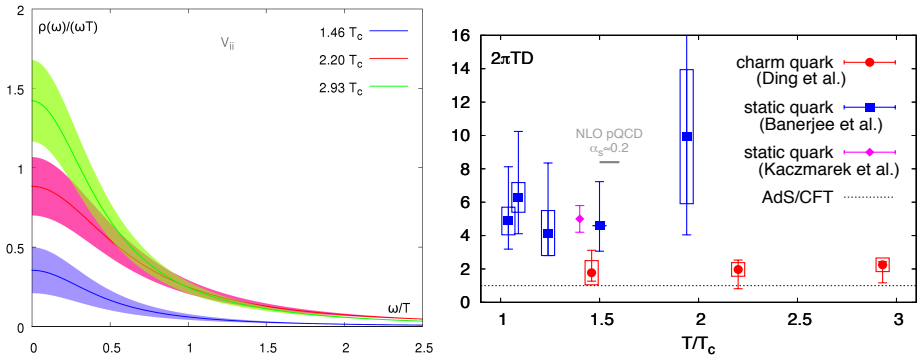


Fig. 21. (Left) The low frequency transport part of the charmonium vector spectral function obtained from a MEM analysis of vector correlation functions in quenched lattice QCD.[174] The central lines are mean values while the bands reflect the statistical uncertainties. (Right) Temperature dependence of heavy quark diffusion coefficients multiplied by $2\pi T$ in pure gluonic matter. The charm diffusion coefficients are obtained from the spectral functions shown in the left plot.[174] Also shown are results for the static quark diffusion coefficient obtained by using the lattice discretized versions of HQEFT.[177,178] The boxes show the statistical error while the error bars reflect the systematic uncertainties. The horizontal dotted line labels the value of $2\pi TD$ in the heavy quark limit from the AdS/CFT correspondence [176] and the short, horizontal solid line indicates the value of $2\pi TD$ from next-to-leading order pQCD calculations at $\alpha_s \simeq 0.2$.[175]

.

theory. This leads to the spectral analysis of a "color-electric correlator"[179,180]

$$G_E(\tau) = -\frac{1}{3}\sum_{i=1}^{3}\frac{\langle \mathrm{ReTr}\,[U(1/T;\tau)gE_i(\tau,\mathbf{0})\,U(\tau;0)gE_i(0,\mathbf{0})]\rangle}{\langle \mathrm{Re\,Tr}\,[U(1/T;0)]\rangle}, \tag{60}$$

where $U(\tau_2;\tau_1)$ is a Wilson line in the Euclidean time direction and $gE_i(\tau,\mathbf{x})$ denotes the color-electric field at time-space $(\tau,\mathbf{x})$. The momentum diffusion coefficient κ can then be extracted from the slope of the corresponding spectral function in the limit of vanishing frequency ω,

$$\kappa/T^3 = \lim_{\omega\to 0}\frac{2\,\rho_E(\omega)}{\omega T^2}. \tag{61}$$

Here $\rho_E(\omega)$ is the corresponding spectral function that is related to $G_E(\tau)$ via Eq. 50. In the non-relativistic limit, i.e. for a heavy quark mass $M \gg \pi T$, the momentum diffusion coefficient κ is related to the (spatial) heavy quark diffusion coefficient D via Eq. 56.

The color-electric correlator $G_E(\tau)$ is defined in terms of gluonic observables only. It thus suffers from a small signal to noise ratio, a problem similar to what one encounters in the calculation of viscosities[181] (see next subsection). In both cases efficient noise reduction techniques are needed for a calculation of the gluonic correlation functions. In a recent study[177] the correlator $G_E(\tau)$ has been calculated using multi-level updates[181,182] as well as the link integration technique.[183,184] The improved correlator $G_{imp}(\tau T)$ obtained this way at $T \simeq 1.4\ T_c$ for four different

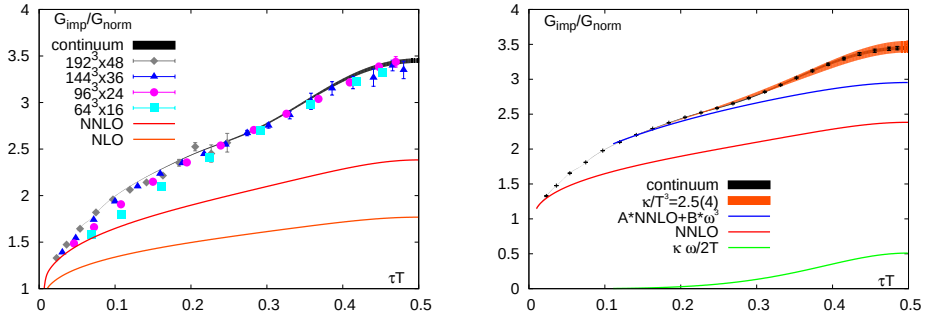


Fig. 22. (Left) Continuum extrapolation of improved color-electric correlator $G_E(\tau) \equiv G_{imp}(\tau)$ (see Eq. 60) normalized to the high temperature, free field theory result $G_{norm}(\tau)$ and the comparison with NNLO and NLO perturbative QCD calculations at 1.4 T_c on quenched lattice QCD.[177] (Right) χ^2 fit to the continuum extrapolated G_{imp}/G_{norm} using an ansatz $\rho_E^{model}(\omega) = \max\left\{A\rho_{NNLO}(\omega) + B\omega^3, \frac{\omega\kappa}{2T}\right\}$. Also shown are the separate contributions to the correlator arising from the different parts of the fit ansatz for the spectral function.[177]

values of the lattice cut-off in quenched QCD has been extrapolated to the continuum limit. Results are shown in the left hand panel of Fig. 22. In order to extract the momentum diffusion coefficient from this correlator an ansatz for the spectral function has been used.[177] The corresponding fit is shown in the right hand panel of Fig. 22. It yields,

$$\kappa/T^3 = 2.5(4) \quad \text{at} \quad T \sim 1.4\ T_c. \tag{62}$$

This corresponds to $2\pi TD = 5.0(8)$ which is consistent with similar lattice QCD studies using HQEFT.[178] However, it is a factor 2 to 3 larger than the charm quark diffusion coefficient discussed above[174] (see Fig.21).

The heavy quark diffusion coefficient D has also been calculated in perturbative QCD in both leading and next-to-leading order as well as from the AdS/CFT correspondence. At $\alpha_s \approx 0.2$ the leading order pQCD calculation[185] gives $2\pi TD \approx 71.2$ while $2\pi TD \approx 8.4$ is obtained in next-to-leading order calculations.[175] In the strong coupling limit $2\pi TD = 1$ is obtained from the AdS/CFT correspondence[176] (see Fig.21).

6.3. *Shear & bulk viscosities*

The computation of shear and bulk viscosities has been attempted already in the 80's.[186] However, it turned out that the signal to noise ratio in calculating Euclidean energy-momentum correlation functions is very small and high statistics or improved algorithms are needed. The latter became available for quenched QCD calculations with the multi-level algorithms[182] which have been used for the calculation of shear and bulk viscosities.[181,187] Results from such an analysis by Meyer[181] and those with direct high statistics calculations by Nakamura & Sakai[188] are shown in Fig. 23.

The ratio obtained in the former calculation are smaller than those obtained in the earlier direct simulations; $\eta/s = 0.102(56)$ at 1.24 T_c and 0.134(33) at 1.65 T_c obtained in quenched QCD on lattices with temporal extent $N_\tau = 8$.[181] This shows that noise reduction techniques like the multi-level algorithm are mandatory for a successful calculation of viscosities. Results on the bulk viscosity to entropy ratio ζ/s show that this ratio rapidly becomes small above T_c.[189] At $T \gtrsim 1.2\ T_c$ it is smaller than η/s and, in fact, within errors it is consistent with zero.[181,188,189]

Still the calculations of viscosities are performed on lattices with rather small temporal extent compared to those used in calculations of the electrical conductivity and diffusion constants. Systematic uncertainties in these calculations need to be better controlled in future. Here it will also be helpful to combine lattice QCD calculations with information from analytic approaches that put constraints on the structure of spectral functions, e.g. QCD sum rules.[190–192]

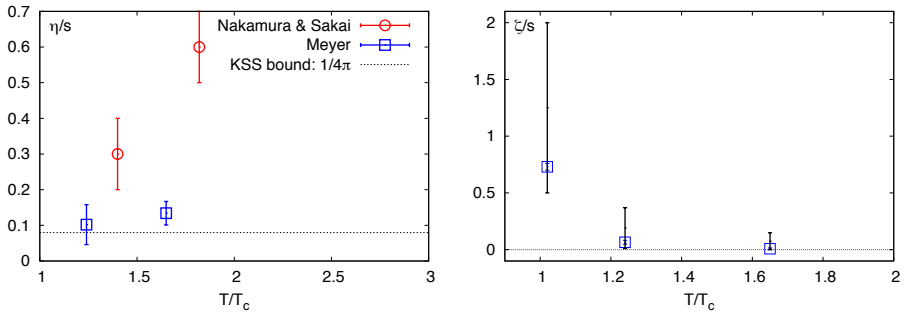


Fig. 23. (Left) Temperature dependence of the shear viscosity, η/s, of gluonic matter obtained by using noise-reduction techniques (squares)[181] and direct high statistical calculations (circles)[188] on $N_\tau = 8$ lattices. The dotted line corresponds to the conjectured lower bound of η/s from AdS/CFT correspondence.[176] (Right) Temperature dependence of the bulk viscosity, ζ/s, of gluonic matter.[189] The square points include the statistical uncertainties while the solid black bars denote the systematic uncertainties. Results for the same quantity from Ref. 188 which are not shown are consistent with zero at $T \in [1.4\ T_c, 1.8\ T_c]$. Data are taken from Refs. 181,188,189.

6.4. *Transport coefficients of second order hydrodynamics*

Due to the importance of viscous effects in the evolution of hot and dense matter created in heavy ion collision there is considerable interest in extending the hydrodynamic modeling beyond leading order gradient expansions of the energy momentum tensor. A second order gradient expansion is parameterized by additional transport coefficients,[193] which may become accessible to lattice QCD calculations.[194–196] One of these new transport coefficients[f] is κ, which controls the momentum depen-

[f]Although this particular second order coefficient is also called κ it should be noted that it is not related to the momentum diffusion coefficient κ introduced in Eq. 56

dence of space-like correlations of the energy momentum tensor. It is defined as the leading order coefficient of the Taylor expansion of the retarded correlator of energy-momentum tensor in momentum $\mathbf{p}$ about zero,[192,197]

$$G^R(\omega=0,\mathbf{p}) = \int_{-\infty}^{\infty} \mathrm{d}t\,\mathrm{d}\mathbf{x}\; \mathrm{e}^{i\mathbf{p}\mathbf{x}} \langle [T_{12}(\tau,\mathbf{x}), T_{12}(0,0)] \rangle \theta(t) \\ = G^R(0) + \frac{\kappa}{2}\,|\mathbf{p}|^2 + \mathcal{O}(|\mathbf{p}|^4)\;. \tag{63}$$

Since the difference between the retarded correlator G^R and the Euclidean correlator at vanishing frequency $\omega = 0$ is just a contact term, which has been shown to be momentum independent,[198] κ can directly be extracted from the corresponding Euclidean correlator,

$$\kappa = 2 \lim_{|\mathbf{p}|\to 0} \frac{\mathrm{d}G^E(\omega=0,\mathbf{p})}{\mathrm{d}|\mathbf{p}|^2}\;. \tag{64}$$

This is considerably simpler to compute than first order coefficients such as the shear or bulk viscosity as it does not require analytic continuation from imaginary time to real time. The only complication is that large spatial lattice sizes are required to get access to small momenta in the lattice QCD calculation.

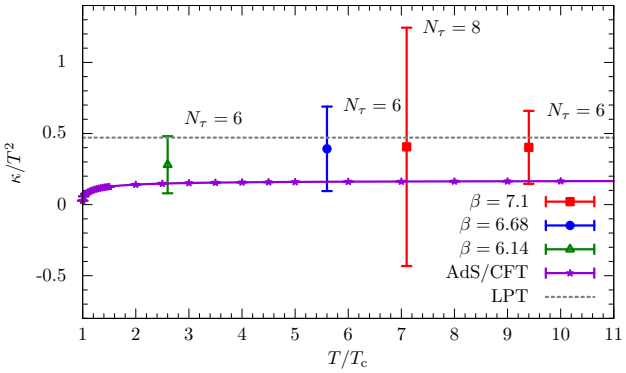


Fig. 24. Transport coefficient of second order hydrodynamics κ/T^2 as a function of T. The lines denote the results from AdS/CFT correspondence[197] and lattice perturbation theory (LPT),[199] respectively.

The second order hydro-coefficient κ has been computed in quenched QCD on lattices with temporal extent $N_\tau = 8$ and 6 and a large spatial size.[199] Results from this calculation are shown in Fig. 24. It yields $\kappa/T^2 = 0.36(15)$. Within the current large errors no further temperature dependence is observed in the temperature range $2T_c < T < 10T_c$ and results are compatible with both perturbative QCD[192,195] and AdS/CFT results.[200]

7. Open heavy flavors and heavy quarkonia

Owing to their large masses heavy flavors, such as charm and bottom, are produced only during the earliest stages of a heavy ion collision and get affected by the hot and dense medium during its entire evolution. They then emerge as hadrons with open heavy flavors or as quarkonia. Thus, heavy flavors provide unique identifiable probes against which the temperature and coupling of the medium created during heavy-ion collisions can be calibrated. The melting of charmonium states has long been considered as an important signature for the formation of quark-gluon plasma.[18] Understanding its production rates and abundance can provide detailed information on properties of the matter formed in a heavy ion collision. We will discuss current results on the temperature dependence of quarkonium bound states in subsection 7.2. In addition, understanding the fate of open flavor bound states also is of importance for the understanding of the strongly interacting regime in the QGP close to the transition temperature. The question whether or not heavy flavor mesons can survive above T_c plays a crucial role in the phenomenological modeling of the heavy quark energy loss.[201–203] Lattice QCD results on the dissociation of open charm hadrons will be discussed in the next subsection.

7.1. *Melting and abundances of open charm hadrons*

Similar to the case of strangeness,[98] discussed in Section 3.2, the deconfinement or melting of open charm hadrons can be probed[152] by using fluctuations of the charm quantum number (C) and its correlations with baryon number (B) fluctuations. To this end one may consider appropriately chosen ratios of correlations between net-baryon and net-charm number fluctuations. One such ratio is, for instance, $\chi_{22}^{BC}/\chi_{13}^{BC}$.[152] Since at low temperatures, for a gas of uncorrelated charmed hadrons, the thermodynamic contributions of the much heavier $|C| = 2, 3$ baryons can be safely neglected, this particular ratio is dominated by $|C| = 1$ baryons and thus yields $\chi_{22}^{BC}/\chi_{13}^{BC} = |B| = 1$. On the other hand, at high temperatures, for a free gas of massive charm quarks with masses much larger than T, the above ratio is[g] $\chi_{22}^{BC}/\chi_{13}^{BC} = |B| = 1/3$. Thus, this quantity can be viewed as a measure for the baryon number associated with the predominant degrees of freedom that are carriers of the charm quantum number in a given temperature region. Its behavior can indicate the liberation of quark-like degrees of freedom with fractional baryon number.

Fig. 25 (left)[152] shows that close to the chiral crossover temperature, $T_c = 154(9)$ MeV, the quantity $\chi_{22}^{BC}/\chi_{13}^{BC}$ starts deviating from unity. This indicates that beyond this temperature fractionally charged quark-like degrees of freedom start appearing and open charm hadrons start to melt. The left hand panel of

[g]Here one makes use of the fact that the Boltzmann gas approximation is still a good approximation for a charm quark gas at a few times the transition temperature. This is the temperature range of interest to heavy ion collision experiments.

Fig. 25 also shows a comparison with similar quantities involving both baryon-strangeness correlations as well as baryon-electric charge correlations. The first of these quantities is sensitive to the deconfinement of strange quarks and the second one is also sensitive to the deconfinement of light up and down quarks. It is clear from the figure that the onset of deconfinement for the charm, strange as well as the up/down quarks happens in the same chiral crossover region.

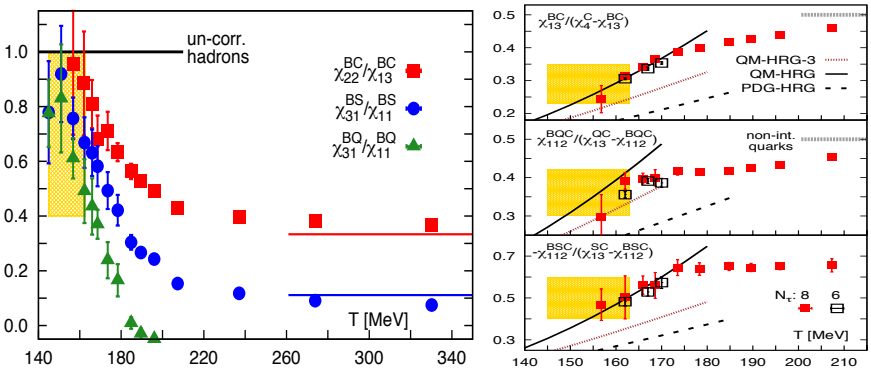


Fig. 25. (Left) Ratios between cumulants of correlations of net baryon number with net charm, net strangeness and net electric charge fluctuations.[152] Deviations of these ratios from unity in the crossover region (shaded band) suggest that the onset of the melting/deconfinement of open charm hadrons as well as open strange hadrons and hadrons with light up/down quarks starts in the same temperature range (see text for details). (Right) Thermodynamic contributions of all charmed baryons (top), all charged charmed baryons (middle) and all strange charmed baryons (bottom) relative to that of corresponding charmed mesons.[152] The dashed lines (PDG-HRG) are predictions for an uncorrelated hadron gas using only the PDG states[31] . The solid lines (QM-HRG) are similar HRG predictions including also the states predicted by the quark model.[204,205] The dotted lines (QM-HRG-3) are the same QM predictions, but only including states having masses less than 3 GeV.

The right hand panel of Fig. 25 shows ratios of generalized susceptibilities that are constructed such that in a gas of uncorrelated hadrons the numerator would correspond to the partial pressure of baryons with quantum numbers selected by the other indices, while the denominator would correspond to the partial pressure of corresponding mesons. E.g. χ_{13}^{BC} will give the partial pressure of charmed baryons and $\chi_4^C - \chi_{13}^{BC}$ filters out the corresponding partial pressure of charmed mesons. The ratios $\chi_{13}^{BC}/(\chi_4^C - \chi_{13}^{BC})$, $\chi_{112}^{BQC}/(\chi_{13}^{QC} - \chi_{112}^{BQC})$ and $-\chi_{112}^{BSC}/(\chi_{13}^{SC} - \chi_{112}^{BSC})$ thus correspond to ratios of partial pressures arising from charmed baryons to that from open charm mesons, charged-charmed baryons to open charm charged mesons and strange-charmed baryons to strange-charmed mesons, respectively. As can be seen in Fig. 25 (right) results for these ratios at low temperatures are well described by a hadron gas that uses open charm resonances obtained in quark model calculations (QM-HRG) while, not surprisingly, it differs strongly from a simple hadron resonance gas based only on the very few experimentally known charmed hadrons

(PDG-HRG). This observation is similar to that made for strange hadron fluctuations in Section 5 (right panel of Fig. 18). These observations clearly provide evidence for contributions from experimentally yet unobserved charmed/strange hadrons to charm and strangeness fluctuations in the vicinity of the crossover transition temperature. In additions, the agreement between lattice QCD data and QM-HRG model calculations below T_c and the onset of deviations just in the transition region also suggests that open charm hadrons start to dissociate in the crossover region. This conclusion is consistent with that drawn from the temperature dependence of the ratio in the left hand panel of Fig. 25, which has the advantage of being independent of details of the charmed hadron spectrum.

7.2. *Heavy Quarkonia*

Inside the QGP the interaction between a heavy quark anti-quark pair gets weakened due to the screening effects of the intervening deconfined colored medium. This telltale signature of the presence of a color deconfined medium is expected to be manifested through melting of heavy quarkonium states,[18] i.e. bound states of a quark anti-quark pair. Melting of heavy quarkonium states in the QGP is also expected to follow a distinctive sequential pattern with the smallest, most tightly bound quarkonium state surviving up to the highest temperature, effectively serving as a 'thermometer' to probe the temperature of the medium created at RHIC (for a recent review see Ref. 206). Since quarkonia do not carry flavor quantum numbers, unlike the open heavy flavor hadrons, their melting cannot be accessed in lattice QCD calculations through quantum number correlation based studies as discussed in Section 7.1. Currently, at least three approaches are being actively pursued to study thermal modifications of heavy quarkonia on the lattice. The first approach is to use potential models with heavy quark potentials computed on the lattice. The second approach relies on the extraction of quarkonium spectral functions from Euclidean temporal correlators. The third approach involves spatial correlation functions of quarkonia and the study of their in-medium screening properties. Here, we summarize the recent progresses and developments concerning these three approaches. More details about earlier lattice results can also be found in Refs. 206–208.

7.2.1. *Heavy quark potential*

Properties of heavy quarkonia in the vacuum have been successfully described by the potential model approach. In this approach, the interaction between a heavy quark pair forming the quarkonium is described by an instantaneous potential.[209,210] Due to its success at zero temperature, the potential model approach has also been applied at nonzero temperature, by making the potential between the heavy quarks temperature dependent.[211] The temperature dependent potentials used in these calculations are based either on model calculations or on finite temperature lattice

QCD results for the free energy and the internal energy. However, justification for the use of these potentials in a Schrödinger equation is mostly based on phenomenological arguments and has no rigorous connections to the real-time evolution of heavy quarkonia described by the Schrödinger equation.

Recently, a non-relativistic effective theory approach at nonzero temperature, relying on a particular hierarchy of the relevant scales, has been developed.[212–214] Generally by integrating out the hard energy scale, i.e. the rest mass of the heavy quark m, Non-Relativistic QCD (NRQCD) effective theory[215,216] is obtained, and by further integrating out the soft scale, i.e. the typical momentum exchange between the bounded quarks of $\mathcal{O}(mv)$, so-called potential non-relativistic QCD (pNRQCD), is obtained.[217] In pNRQCD a heavy quark bound state can be described by a two-point function satisfying a Schrödinger equation,[212–214]

$$i\partial_t D^{>}_{NR}(t,\vec{r}) = \left(-\frac{1}{m}\nabla_r^2 + V(t,r)\right) D^{>}_{NR}(t,\vec{r}), \tag{65}$$

where $D^{>}_{NR}(t,\vec{r})$ is the real-time forward heavy quark pair correlation function in the non-relativistic limit. The potential $V(t,r)$ in such a Schrödinger equation is well defined and turns out to be complex valued.[212–214] Its real part reflects color Debye screening effects while the imaginary part is related to Landau-damping, i.e. the scattering of quarks with the constituents of the medium and the absorption of gluons from the medium via singlet-octet transition.[214] It has been shown in Ref. 218 that in the limit $m \to \infty$ the leading part of the potential $V(t,r)$ can be obtained as

$$V(r) = \lim_{t\to\infty} \frac{i\partial_t W(t,r)}{W(t,r)} \,, \tag{66}$$

where $W(t,r)$ is the real-time thermal Wilson loop. Through a Fourier transformation one obtains,

$$W(t,r) = \int_{-\infty}^{+\infty} \mathrm{d}\omega\, \rho(\omega,r)\, \mathrm{e}^{-i\omega t} \,, \tag{67}$$

where $\rho(\omega,r)$ is the spectral function of the real-time Wilson loop. The above equation can be analytically continued to the Euclidean time, giving

$$W(\tau,r) = \int_{-\infty}^{+\infty} \mathrm{d}\omega\, \rho(\omega,r)\, \mathrm{e}^{-\omega\tau} \,. \tag{68}$$

In Eq. 68 the Wilson loop, $W(\tau,r)$ is the usual Euclidean-time Wilson loop which can be obtained from lattice QCD calculations. As if there exists a well defined lowest lying peak structure in the spectral function $\rho(\omega,r)$ it would dominate the dynamics in the Wilson loop in the late time limit thus giving to the complete information of the heavy quark potential as shown in Eq. 66. However, as argued in Ref. 219 the late time dynamics is not completely separated from the early time non-potential physics and to take these effects into account a skewed Lorentzian function including the early time contribution for $\rho(\omega,r)$ is required to fit the Wilson loop.

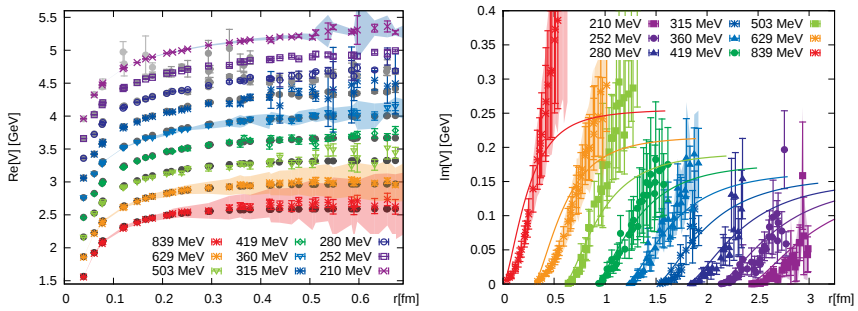


Fig. 26. Real (left) and imaginary (right) parts of the heavy quark potential calculated in quenched lattice QCD.[221] Values are shifted for better visibility. Gray circles denote color singlet free energies and solid lines are leading order hard thermal loop results.

The position and width of this skewed Lorentzian peak are connected to the real and the imaginary parts of the potential, respectively. Thus, by extracting the spectral function, $\rho(\omega, r)$, from the Euclidean-time Wilson loop[h], $W(\tau, r)$, obtained from lattice QCD calculations and by subsequently fitting this $\rho(\omega, r)$ with a skewed Lorentzian ansatz the real and the imaginary part of the heavy quark potential, $V(r)$, can be obtained.

This procedure has been tested using the Wilson loop calculated using hard thermal loop perturbation theory[220] as well as for the pure gauge theory.[221] Fig. 26 shows the real (left) and imaginary (right) parts of the heavy quark potential in the pure gluonic medium.[221] The real part of the heavy quark potential turns out to be close to the heavy quark singlet free energy, defined through the spatial correlation function of the Polyakov loop and its conjugate,[222] at all temperatures. At high temperatures the imaginary part of the heavy quark potential is close to the leading order hard thermal loop result, but at low temperatures it lies below hard thermal loop result.

Using the same procedure the real part of the heavy quark potential has also been extracted in (2+1)-flavor QCD[221] on lattices with temporal extent of only $N_\tau = 12$. Of course, on such small lattices it is hardly possible to extract reliable information on the imaginary part of the heavy quark potential. Nonetheless, similar to the quenched limit result the real part of the heavy quark potential is found to be close to the singlet free energies. However, string breaking is not observed at $T < T_c \approx 174$ MeV up to ~ 1.2 fm. This could be due to the large pion mass ($m_\pi \approx 300$ MeV) employed in this exploratory QCD calculation.

The heavy quark potential has also been extracted from the Wilson line correlation function calculated on $48^3 \times 12$ lattices at $T = 250$ MeV and 305 MeV using a fit ansatz motivated by hard thermal loop calculations.[223] These calculations used

[h]As illustrated in Ref. 220 in order to avoid the cusp divergence and the large noise to signal ratio in computations of Wilson loops, some other observables, e.g. Wilson line correlation functions defined in the Coulomb gauge, can be a substitution and are actually used in lattice calculations.

HISQ action with quark masses that would correspond to $m_\pi \approx 160$ MeV in the continuum limit. In this calculation the real part of the potential was found to be equal or larger than the singlet free energies at these two temperatures and it always was smaller than the zero temperature potential. Moreover, the imaginary part is found to be of similar size as predicted by leading order hard thermal loop perturbation theory.[223]

7.2.2. *Spectral functions of quarkonia*

The spectral function of quarkonium can be extracted from lattice QCD calculations of the two-point correlation functions of the heavy quark currents in the Euclidean time

$$G(\tau,T) = \int d^3\vec{x} \left\langle \left(\bar{q}(\tau,\vec{x})\,\Gamma\,q(\tau,\vec{x})\right)\left(\bar{q}(0,\vec{0})\,\Gamma\,q(0,\vec{0})\right)^\dagger \right\rangle \,, \tag{69}$$

where q represents the heavy quark field. Γ are Dirac matrices defining the spin structure of quarkonium, in particular $\Gamma = 1, \gamma_5, \gamma_\mu, \gamma_5\gamma_\mu$ corresponds to the scalar, pseudo-scalar, vector and axial-vector quarkonium states, respectively. Signatures of medium modification and melting of quarkonium are reflected in the structure of the spectral density $\rho(\omega,T)$. It can be obtained from the quarkonium correlator in the Euclidean-time

$$G(\tau,T) = \int_0^\infty \frac{d\omega}{2\pi}\rho(\omega,T)\frac{\cosh\left(\omega\left(\tau-1/2T\right)\right)}{\sinh\left(\omega/2T\right)} \,. \tag{70}$$

While $\rho(\omega,T)$ is a continuous function of the frequency ω over an infinite range, $G(\tau,T)$ is calculable on the lattice only at a finite number of discrete points along the temporal direction due to the finiteness of the lattice. As has been discussed in Section 6 inverting Eq. 70 to get spectral function $\rho(\omega,T)$ from the correlation function $G(\tau,T)$ is a typical ill-posed problem and a suitable inversion method is needed to solve the problem. The commonly used inversion methods for the extractions of quarkonium spectral functions is the Maximum Entropy Method (MEM).[153] Variants of this have recently been suggested which include a modified MEM with an extended search space[224,225] and a Bayesian method which is analogous to MEM but uses a different prior distribution.[226]

The charmonium spectral functions at finite temperature have been studied extensively for quenched lattice QCD.[228–232] Recently quenched lattice QCD calculations[227] have been performed using lattices with large temporal extents, leading to quite reliable extractions of the charmonium spectral functions. Fig. 27 illustrates the spectral functions of J/Ψ (left) and η_c (right) for various temperatures. These studies suggest that all charmonium states are dissociated for $T \gtrsim 1.5T_c$ in a gluonic plasma.[227] Investigations on charmonium spectral functions in lattice QCD calculations with dynamical quarks lead to consistent conclusions.[233,234]

Lattice QCD calculations for bottom quarks are technically challenging since present computational limitations do not permit calculations with sufficiently fine

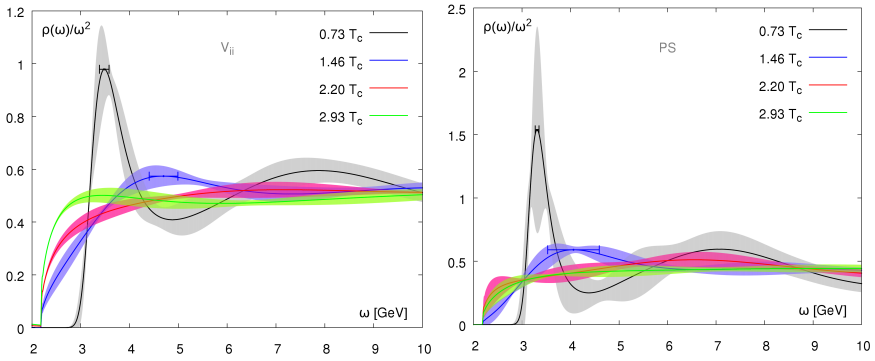


Fig. 27. Temperature dependence of J/Ψ (left) and η_c (right) spectral functions obtained from quenched lattice QCD calculations.[227]

lattice spacings that are much smaller than the inverse of the heavy bottom quark mass. Large discretization errors arise from the large heavy-quark bare mass in units of the lattice spacing, $m_b a$. Nonetheless, although it is computationally very demanding relativistic bottomonium correlations functions have been computed recently in quenched QCD using isotropic lattices with N_σ=192 and large temporal extent,[236] $N_\tau = 96$ and 48 at the same value of the lattice spacing, $a \simeq 0.01$ fm, i.e. $m_b a \simeq 0.2$. The temporal lattice sizes correspond to temperatures $T = 0.7\ T_c$ and $1.4\ T_c$. In this calculation it has been found that at $1.4\ T_c$ only the bottomonium correlation function in the vector channel show significantly smaller thermal modifications than the charmonium correlation function in the same channel.[236]

To circumvent the problem of large cut-off effects in calculations with bottom quarks without performing calculations at extremely small lattice spacings, one needs to adapt a lattice discretization scheme for heavy quarks that is capable to describe heavy quark physics in some chosen kinematic regime also at moderately small values of the cut-off. One such approach is Non-Relativistic QCD (NRQCD)[237,238] where the heavy quark mass is assumed to be much larger than the inverse lattice spacing, but the momentum dependence of the heavy quark energy is included in the non-relativistic limit. NRQCD does not possess a proper continuum limit because the radiative corrections to coefficients of the NRQCD Lagrangian diverge as $m_b a \to 0$. However, since the non-relativistic quark field is not compactified along the Euclidean-time direction, the relation between Euclidean-time quarkonium correlation functions and the corresponding spectral functions becomes simpler,

$$G(\tau, T) = \int_0^\infty \frac{\mathrm{d}\omega}{2\pi}\, \rho(\omega, T)\ \mathrm{e}^{-\omega\tau}\ , \tag{71}$$

giving rise to a temperature independent integration kernel, $\exp(-\omega\tau)$. Moreover, the transport peak is also absent in the NRQCD spectral function, which makes its determination much easier.

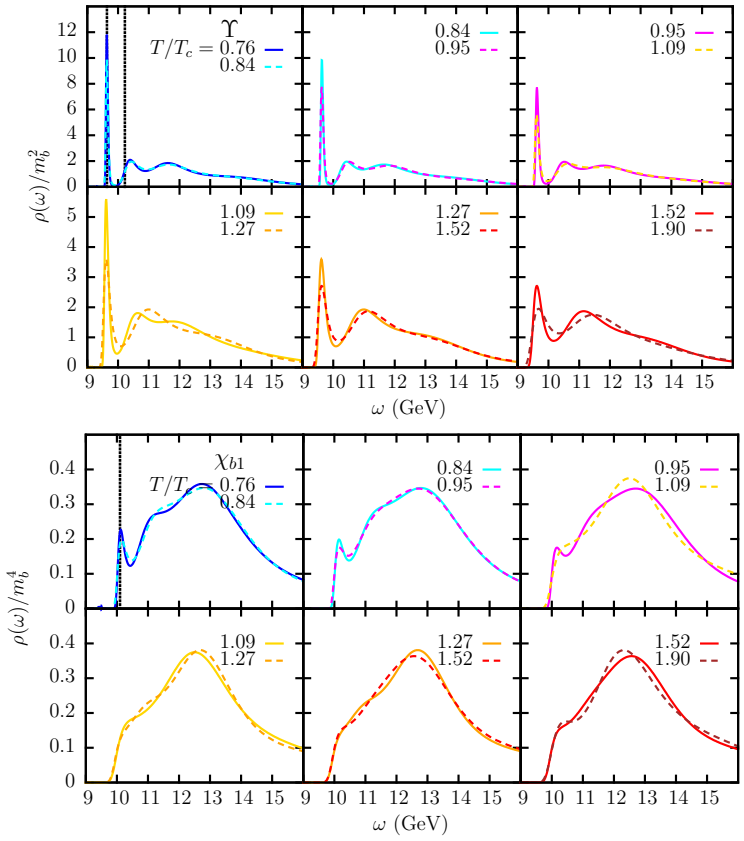


Fig. 28. Temperature dependence of spectral functions for the Υ (top) and χ_{b1} states (bottom). Results are obtained by using a lattice discretized form of NRQCD.[235]

Treating the bottom quark within the NRQCD framework the fate of bottomonium states has been studied on anisotropic lattices using $N_f = 2$ and $2 + 1$ of improved Wilson quarks with $m_\pi \approx 400$ MeV and $m_\pi \approx 500$ MeV, respectively.[235,239–242] Fig. 28 shows the temperature dependence of the Υ (top) and χ_{b1} (bottom) spectral functions extracted using the MEM.[235] This indicates that the S-wave ground state Υ survives up to 1.9 T_c while the P-wave ground state χ_{b1} melts just above T_c.[235] However, a recent lattice QCD study[243] that uses a different Bayesian method suggested in Ref. 226 for the extraction of the spectral functions finds that the P-wave ground state χ_{b1} may survive up to 1.6 T_c. This analysis, however, has been performed on lattices with a rather small temporal extents, $N_\tau = 12$.

7.2.3. *Spatial correlation functions of quarkonia*

Similarly as the temporal correlation functions spatial quarkonium correlation functions are defined as the sum of heavy quark current-current correlation functions instead over a 'funny' space of τ, x and y

$$G(z,T) = \int_0^{1/T} \mathrm{d}\tau \int \mathrm{d}x\,\mathrm{d}y \left\langle \left(\bar{q}(\tau,\vec{x})\,\Gamma\,q(\tau,\vec{x})\right)\left(\bar{q}(0,\vec{0})\,\Gamma\,q(0,\vec{0})\right)^{\dagger}\right\rangle \,, \tag{72}$$

are also related to the quarkonium spectral functions as follows

$$G(z,T) = \int_{-\infty}^{\infty} \frac{\mathrm{d}p_z}{2\pi}\,\mathrm{e}^{ip_z z} \int_0^{\infty} \frac{\mathrm{d}\omega}{2\pi}\,\frac{\rho(\omega,p_z,T)}{\omega}. \tag{73}$$

The spatial correlation functions, however, are sensitive also to the momentum dependence of spectral functions which is reflected in an additional integration over the momentum p_z along the z-direction. Despite of its more complicated connection to the spectral function compared to that of temporal correlators (see Eq. 70), the spatial correlation function has some distinct advantages. Since the spatial separation is not limited by the inverse temperature, the spatial correlation function can be studied at separations larger than $1/T$ and thus is more sensitive to in-medium modifications of quarkonia. Furthermore, in contrast to the temporal correlation functions, the spatial correlation functions can be directly compared to the corresponding vacuum correlation function to quantify modifications of the in-medium spectral function as the entire temperature dependence of spatial correlation functions emerges from the temperature dependence of the spectral function (Eq. 73), while in the case of temporal correlation functions (Eq. 70) this temperature dependence is folded with the temperature dependence of the kernel, $\cosh\left(\omega\left(\tau - 1/2T\right)\right) / \sinh\left(\omega/2T\right)$.

While the relation between spectral functions and spatial meson correlators is more involved, in some limiting cases it becomes more intuitive. At large distances the spatial correlation functions decay exponentially, $G(z,T) \sim \exp(-M(T)z)$, characterized by the screening mass M. At low temperatures this exponential drop of a mesonic correlator projecting on a given quantum number channel Γ is controlled by the bound state with smallest mass in this channel. The spectral function then is dominated by this state,

$$\rho(\omega,p_z,T) \sim \delta(\omega^2 - p_z^2 - m_0^2), \tag{74}$$

where M becomes equal to the pole mass m_0 of the meson. At high temperatures, when the mesonic excitations have completely dissolved and become uncorrelated, the spatial meson correlation functions describe the propagation of a free quark anti-quark pair and the screening mass is given by[244]

$$M_{\mathrm{free}} = \sqrt{m_{q_1}^2 + (\pi T)^2} + \sqrt{m_{q_2}^2 + (\pi T)^2}, \tag{75}$$

where m_{q_1} and m_{q_2} are the masses of the quark and anti-quark that form the meson. This form of the screening mass in the non-interacting limit is a consequence of the

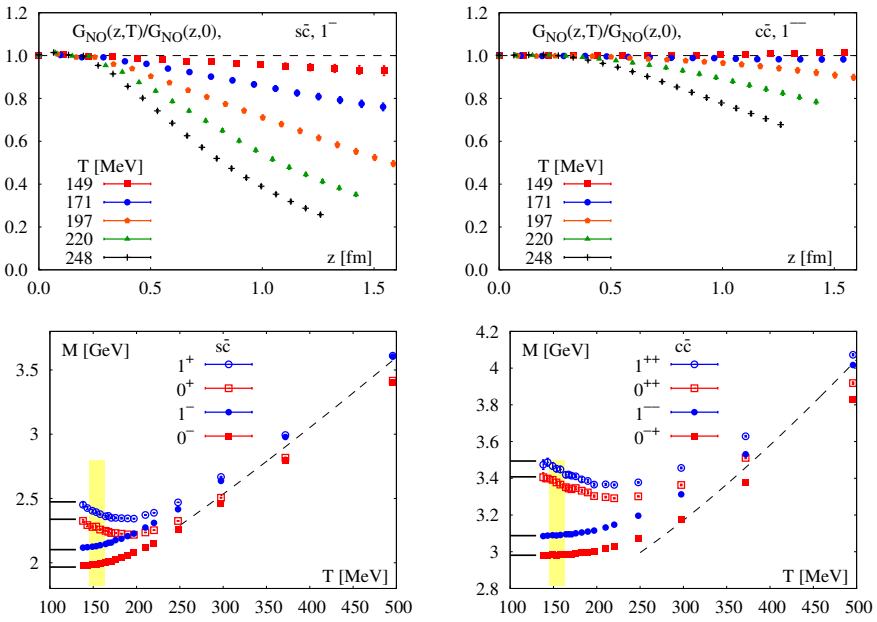


Fig. 29. (Top) Temperature dependence of ratios of spatial correlation functions to those at zero temperature for D_s^* (top left) and J/Ψ (top right).[245] (Bottom) Temperature dependence of screening masses of ground state $s\bar{c}$ mesons (left) D_{s1}^* (1^+), D_{s0}^* (0^+), D_s^* (1^-) and D_s (0^-) and ground state charmonia (right) χ_{c_1} (1^{++}), χ_{c_0} (0^{++}), J/Ψ (1^{--}) and η_c (0^{-+}).[245] The horizontal solid lines denote the corresponding zero-temperature meson masses and the dashed line depicts the non-interacting theory limit of a freely propagating quark anti-quark pair. The yellow band denotes the chiral crossover temperature region, i.e. $T_c = 154 \pm 9$ MeV.

fermionic (anti-periodic) boundary condition along the Euclidean-time direction, which leads to the appearance of a smallest non-zero Matsubara frequency, πT, in the quark and anti-quark propagators. As the bosonic meson state is dissolved in the non-interacting limit the screening mass reflects two independently propagating fermionic degrees of freedom. Thus, the transition between these two limiting values for the screening mass can be used as an indicator for the thermal modification and eventual dissociation of charmonia and open charm mesons.

A first analysis of spatial correlation functions of charmonia was performed using staggered fermions with the p4 action.[246] Recently, a detailed comparative study of the spatial correlation functions of charmonia and open charm mesons was performed using the HISQ action.[245] Fig. 29 shows ratios of the spatial correlation functions for the D_s^* (top left) and the J/Ψ (top right) at different temperatures to the corresponding zero temperature results. As discussed before, such a ratio can directly probe the thermal modifications of the spectral functions. If there is no change in the meson spectral functions, these ratios will be equal to unity and deviations from unity will indicate in-medium modification of the meson spectral

functions at non-zero temperature. As can be seen, even for $T \sim T_c \approx 154$ MeV the ratio for the open charm sector (Fig. 29 (top left)) shows significant deviation from unity. This is completely consistent with the previously discussed quantum number correlation based studies in Section 7.1 which concluded that open charm mesons start to melt in the vicinity of T_c.[152] On the other hand, for the charmonia the ratio of non-zero to zero temperature correlation functions remains very close to unity for $T \lesssim 170$ MeV and significant deviations, comparable to the open charm sector at $T \sim T_c$, only show up for $T \gtrsim 200$ MeV (Fig. 29 (top right)). This indicates that up to $T \simeq 1.1\ T_c$ J/Ψ exists almost like a vacuum state and significant thermal modifications appears only for $T \gtrsim 1.3 T_c$. The same physics is also reflected in temperature dependence of the screening masses of open charm mesons and charmonia as shown in Fig. 29 (bottom). The screening masses of all open charm mesons (bottom left) start to deviate from unity significantly already in the chiral crossover region. The J/Ψ and η_c screening masses (bottom right), however, remain to be almost identical to their vacuum pole masses up to $T \simeq 1.1\ T_c$. The screening masses for χ_{c0} and χ_{c1} deviate from their vacuum masses even below T_c indicating significant thermal modifications of these states. At higher temperatures, i.e. $T \gtrsim 2\ T_c$ the screening masses in all channels increase linearly with temperature. This rise agrees well with that of a freely propagating quark anti-quark pair.

8. QCD in external magnetic fields

In recent past it has been realized that large magnetic fields created during the early stages of heavy-ion collisions may give rise to fascinating observable effects induced through the coupling between the magnetic field and the chiral anomaly.[20,21] This observation also motivated a plethora of activities including lattice QCD studies of hot-dense strong-interaction matter under the influence of external magnetic fields. This section presents a very brief summary of these lattice QCD studies. More comprehensive reviews on this topic can be found in Refs. 247–250.

An external magnetic field along the z-direction, $\vec{B} = B\hat{z}$, can be induced by choosing electro-magnetic gauge fields: $A_{\hat{y}} = Bx$ and $A_{\hat{x}} = A_{\hat{z}} = A_{\hat{\tau}} = 0$. On the lattice this can be implemented simply by multiplying the $SU(3)$ gauge field variables $U_{n,\hat{\mu}}$ with the corresponding $U(1)$ phase factors: $u_{n,\hat{y}} = e^{ia^2 qBn_x}$ and $u_{n,\hat{x}} = u_{n,\hat{z}} = u_{n,\hat{\tau}} = 1$. Here, q is the (electric) charge of a quark and $n = (n_x, n_y, n_z, n_\tau)$ denotes a lattice site, with $n_{x,y,z} = 1 \ \ldots \ N_\sigma$ and $n_\tau = 1 \ \ldots \ N_\tau$. This choice ensures that the magnetic flux, $a^2 B$, is constant through all the plaquettes in the x-y plane, except at the boundary $(N_\sigma, n_y, n_z, n_\tau)$ owing to the periodic boundary condition on the gauge fields along the spatial directions. Thus, to preserve the smoothness of the external magnetic field across the boundary and the gauge invariance of the fermion action the $U(1)$ factor on the boundary links must be modified: $u_{(N_\sigma,n_y,n_z,n_\tau),\hat{x}} = e^{-ia^2 qN_\sigma Bn_y}$. By making such a choice one pays the price that the magnetic flux becomes quantized, $a^2 B = 2\pi n_B/(qN_\sigma^2)$

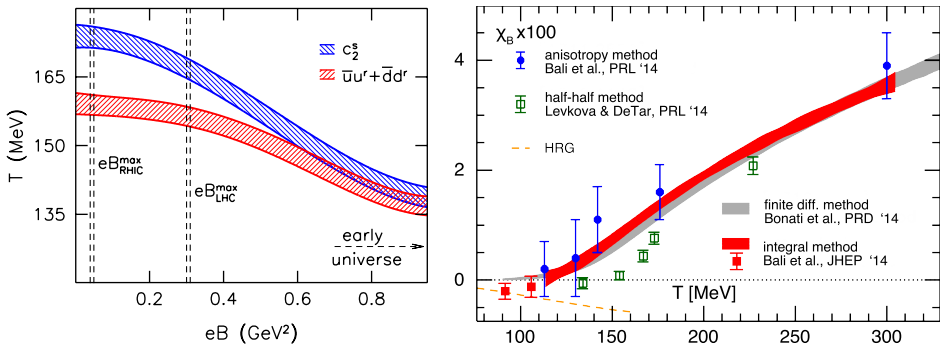


Fig. 30. (Left) The QCD crossover temperature as a function of the magnetic field obtained from the inflection point of the quark condensate (red band) and strange quark susceptibility (blue band).[253] (Right) The magnetic susceptibility χ_B, i.e. the correction to the pressure proportional to quadratic power of the magnetic field, as a function of temperature.[258]

with $n_B = 0 \ldots N_\sigma^2$. Thus, at a given temperature T and on a finite volume there is a minimal value for the constant, external magnetic field $B = 2\pi T^2 N_\tau^2/(qN_\sigma^2)$. On the other hand, for given temporal extent, N_τ, of the lattice the maximal value of the magnetic field achieved in this case is $B = 2\pi T^2 N_\tau^2/q$. Most importantly, since the external magnetic field is induced by multiplying the $SU(3)$ gauge field variables with purely imaginary phase factors the fermion determinant remains real and positive, allowing direct Monte-Carlo sampling.

The QCD crossover transition in an external magnetic field has been extensively studied using lattice QCD. In contrast to the earlier effective model based predictions and the results of first lattice QCD calculations[251,252] using unimproved staggered fermions with heavy pion masses, the QCD crossover temperature T_c turns out to decease with increasing magnetic field.[253–255] Fig. 30 (left) illustrates the decrease of T_c as function of the magnetic field.[253] The reduction of T_c follows from the reduction of the chiral condensate with increasing B, a phenomenon known as the inverse magnetic catalysis, for the relevant intermediate temperature range. However, for low as well as high enough temperatures the chiral condensate shows the expected magnetic catalysis, i.e. an increase with increasing B.[255–257]

The response of the hot strong-interaction matter to an external magnetic field has also been investigated through lattice QCD calculations of the magnetic susceptibility. The magnetic susceptibility is the second derivative of the QCD partition function with respect to the external magnetic field B and, thus, gives the order B^2 corrections to the pressure. Since the standard approach leads to discrete, quantized values for B on the lattice, unlike for the susceptibilities of the chemical potentials, taking direct derivatives of the QCD partition function with respect to B is not straightforward. Lattice calculations of the magnetic susceptibility have been performed using three different approaches: (i) by computing the free energy difference

through an integration over the varying magnetic field;[259,260,260] (ii) through computations of the magnetization via pressure anisotropies parallel and orthogonal to the direction of the magnetic field;[261,262] (iii) by adopting a non-uniform external field such that the net magnetic flux across the x-y plane of the whole lattice is zero, resulting in a non-quantized magnetic field and allowing for a direct computation of the derivatives of the partition function with respect to B.[263] As shown in Fig. 30 (right), all these different approaches produce more or less consistent results. The QGP phase turns out to be paramagnetic. However, for low enough temperatures QCD is weakly diamagnetic, in accordance with the hadron resonance gas model.[264] These results also suggests that for $T \lesssim 300$ MeV the order B^2 magnetic contribution to the QCD pressure is at best a few percent for a magnetic field of the order of 10^{15} T, which is relevant for heavy-ion collision experiments.[21]

Lattice QCD studies have also been carried out to investigate the chiral magnetic effect,[21] namely the phenomenon of (electric) charge separation along the direction of the magnetic field in presence of chiral anomaly induced topological fluctuations. Various different avenues have been pursued by studying: (i) charge fluctuations on given topological background;[265] (ii) enhanced fluctuations of the electric current along the magnetic field,[266] (iii) dependence of the electric current on a given axial chemical potential,[266] (iv) correlations of the electric polarization and the topological charge.[267] In all cases, the chiral magnetic effect has been observed, however, in a suppressed magnitude compared to the model based expectations. Obviously, in lattice QCD studies of the chiral magnetic effect, which is closely related to the chiral anomaly of QCD, it would be of great interest to have lattice QCD calculations perfomed with a chiral fermion formulation. Fully dynamical calculations with DWF or overlap fermions at present do not yet exist.

9. Summary

In this review we have discussed selected topics in finite temperature QCD that have a direct link to the ongoing experimental study of the phase diagram of strong-interaction matter and the properties of matter formed in heavy ion collisions. We naturally focused on topics to which lattice QCD calculations can contribute and have lead or may lead to definite, quantitative answers in the future.

Lattice QCD calculations at finite temperature started more than 30 years ago with simulations of pure $SU(N)$ gauge theories on computers that delivered less than one Mega-Flop/s peak-performance. Nowadays these calculations are performed with dynamical quarks and the correct mass spectrum of QCD on computers that reach a peak-performance of more than ten Peta-Flop/s. The field thus could utilize computing resources with a peak-performance that increased by more than ten orders of magnitude, or doubled the speed almost every year. Although we know quite well from the physics of the hadron gas that an exponential rise cannot continue for ever, we still do not seem to have reached the critical point and we may

also in the future expect to gain further inside into the physics of strong-interaction matter through numerical lattice QCD calculations.

During the last years lattice QCD calculations have accomplished two long-standing goals: (i) the pseudo-critical temperature of strong-interaction matter with physical light and strange quark masses has been determined at vanishing net-baryon number, $T_c = (154 \pm 9)$ MeV, and (ii) the equation of state has been calculated in a wide temperature range. It now is frequently used in the hydrodynamic modeling of heavy ion collisions. The extension of these results to non-zero chemical potential is well controlled at least in leading order Taylor expansion of the pressure in terms of baryon, electric charge and strangeness chemical potentials and we will soon have results for bulk thermodynamics in a range of baryon chemical potentials $\mu_B/T \lesssim 3$, which will cover most of the parameter space that can be explored in heavy ion experiments at RHIC and the LHC. These Taylor expansions also provide specific information on fluctuations of and correlations among conserved charges. Lattice QCD calculations of these observables have reached a stage where guidance can be provided to the experimental search for the critical end point and, with some care, a comparison between experimental results for measured proton number, strangeness and, in particular, electric charge fluctuations on the one hand and lattice QCD calculations on the other hand starts to become possible.

A major focus in the ongoing experimental heavy ion program is to explore in detail the properties of matter formed in heavy ion collisions. The analysis of transport coefficients, thermal masses and screening lengths does play an important role in this effort. Lattice QCD calculations of these quantities are possible, although in many cases they are complicated as an analytic continuation from Euclidean time to Minkowski time is needed. For this reason most of the existing calculations have been performed in the quenched approximation where fermionic degrees of freedom are taken into account only as valence quarks and the influence of virtual quark loops on the gluonic background is neglected. Still these calculations prepare the ground for future fully dynamical calculations of transport properties of strong-interaction matter, for which in some cases exploratory work has already started.

There remain many obvious, open questions in the study of the phase diagram of strong-interaction matter and the properties of the strongly interacting medium created in heavy ion collisions which can be addressed in future lattice QCD calculations and which will profit from future increasing computing resources as well as algorithmic advances. Calculations at non-zero baryon number density and the search for the critical point, the calculation of transport properties with fully dynamical, light quarks as well as calculations of thermodynamic quantities using chiral fermion discretization schemes are among the most demanding problems which hopefully can be addressed in the coming years with improved techniques and resources.

Acknowledgements

This review would not have been possible without the input from many of our colleagues, in particular, Prasad Hegde, Olaf Kaczmarek, Christian Schmidt and Mathias Wagner, with whom we could collaborate over many years in the HotQCD and Bielefeld-BNL-CCNU collaborations. This work has been supported in part through contract DE-SC0012704 with the U.S. Department of Energy, the BMBF under grant 05P12PBCTA and the GSI BILAER grant.

References

1. R. Hagedorn, *Statistical thermodynamics of strong interactions at high-energies*, *Nuovo Cim.Suppl.* **3** (1965) 147–186.
2. G. Baym, *Confinement of quarks in nuclear matter*, *Physica A* **96** (1979) 131.
3. T. Celik, F. Karsch, and H. Satz, *A percolation approach to strongly interacting matter*, *Phys.Lett.* **B97** (1980) 128–130.
4. K. Redlich and H. Satz, *The Legacy of Rolf Hagedorn: Statistical Bootstrap and Ultimate Temperature*, `arXiv:1501.0752`.
5. H. D. Politzer, *Reliable Perturbative Results for Strong Interactions?*, *Phys.Rev.Lett.* **30** (1973) 1346–1349.
6. D. J. Gross and F. Wilczek, *Ultraviolet Behavior of Nonabelian Gauge Theories*, *Phys.Rev.Lett.* **30** (1973) 1343–1346.
7. N. Cabibbo and G. Parisi, *Exponential Hadronic Spectrum and Quark Liberation*, *Phys.Lett.* **B59** (1975) 67–69.
8. J. C. Collins and M. Perry, *Superdense Matter: Neutrons Or Asymptotically Free Quarks?*, *Phys.Rev.Lett.* **34** (1975) 1353.
9. E. V. Shuryak, *Quantum Chromodynamics and the Theory of Superdense Matter*, *Phys.Rept.* **61** (1980) 71–158.
10. R. D. Pisarski and F. Wilczek, *Remarks on the Chiral Phase Transition in Chromodynamics*, *Phys.Rev.* **D29** (1984) 338–341.
11. K. Rajagopal and F. Wilczek, *The Condensed matter physics of QCD*, `hep-ph/0011333`.
12. K. Fukushima and T. Hatsuda, *The phase diagram of dense QCD*, *Rept.Prog.Phys.* **74** (2011) 014001, [`arXiv:1005.4814`].
13. K. G. Wilson, *Confinement of Quarks*, *Phys.Rev.* **D10** (1974) 2445–2459.
14. M. Creutz, *Monte Carlo Study of Quantized SU(2) Gauge Theory*, *Phys.Rev.* **D21** (1980) 2308–2315.
15. L. D. McLerran and B. Svetitsky, *A Monte Carlo Study of SU(2) Yang-Mills Theory at Finite Temperature*, *Phys.Lett.* **B98** (1981) 195.
16. J. Kuti, J. Polonyi, and K. Szlachanyi, *Monte Carlo Study of SU(2) Gauge Theory at Finite Temperature*, *Phys.Lett.* **B98** (1981) 199.
17. J. Engels, F. Karsch, H. Satz, and I. Montvay, *High Temperature SU(2) Gluon Matter on the Lattice*, *Phys.Lett.* **B101** (1981) 89.
18. T. Matsui and H. Satz, *J/ψ Suppression by Quark-Gluon Plasma Formation*, *Phys.Lett.* **B178** (1986) 416.
19. R. Rapp and J. Wambach, *Chiral symmetry restoration and dileptons in relativistic heavy ion collisions*, *Adv.Nucl.Phys.* **25** (2000) 1, [`hep-ph/9909229`].
20. D. E. Kharzeev, K. Landsteiner, A. Schmitt, and H.-U. Yee, *'Strongly interacting*

matter in magnetic fields': an overview, *Lect.Notes Phys.* **871** (2013) 1–11, [arXiv:1211.6245].
21. D. E. Kharzeev, L. D. McLerran, and H. J. Warringa, *The Effects of topological charge change in heavy ion collisions: 'Event by event P and CP violation'*, *Nucl.Phys.* **A803** (2008) 227–253, [arXiv:0711.0950].
22. A. D. Linde, *Infrared Problem in Thermodynamics of the Yang-Mills Gas*, *Phys.Lett.* **B96** (1980) 289.
23. E. Braaten and R. D. Pisarski, *Soft Amplitudes in Hot Gauge Theories: A General Analysis*, *Nucl.Phys.* **B337** (1990) 569.
24. N. Haque, A. Bandyopadhyay, J. O. Andersen, M. G. Mustafa, M. Strickland, et al., *Three-loop HTLpt thermodynamics at finite temperature and chemical potential*, *JHEP* **1405** (2014) 027, [arXiv:1402.6907].
25. E. Braaten and A. Nieto, *Effective field theory approach to high temperature thermodynamics*, *Phys.Rev.* **D51** (1995) 6990–7006, [hep-ph/9501375].
26. A. Hietanen, K. Kajantie, M. Laine, K. Rummukainen, and Y. Schroder, *Three-dimensional physics and the pressure of hot QCD*, *Phys.Rev.* **D79** (2009) 045018, [arXiv:0811.4664].
27. I. Montvay and G. Muenster, *Quantum Fields on a Lattice* . Cambridge Monographs on Mathematical Physics, 2010.
28. H. J. Rothe, *Lattice Gauge Theories: An Introduction (Fourth Edition)*. World Scientific Lecture Notes in Physics, 2012.
29. T. Degrand and C. Detar, *Lattice Methods for Quantum Chromodynamics*. World Scientific, 2006.
30. C. Gattringer and C. Lang, *Quantum Chromodynamics on the Lattice-An Introductory Presentation*. Springer, 2010.
31. **Particle Data Group** Collaboration, K. Olive et al., *Review of Particle Physics*, *Chin.Phys.* **C38** (2014) 090001.
32. P. Hasenfratz and F. Karsch, *Chemical Potential on the Lattice*, *Phys.Lett.* **B125** (1983) 308.
33. R. Gavai, *Chemical Potential on the Lattice Revisited*, *Phys.Rev.* **D32** (1985) 519.
34. G. Aarts, F. A. James, E. Seiler, and I.-O. Stamatescu, *Complex Langevin: Etiology and Diagnostics of its Main Problem*, *Eur.Phys.J.* **C71** (2011) 1756, [arXiv:1101.3270].
35. G. Aarts, L. Bongiovanni, E. Seiler, D. Sexty, and I.-O. Stamatescu, *Controlling complex Langevin dynamics at finite density*, *Eur.Phys.J.* **A49** (2013) 89, [arXiv:1303.6425].
36. D. Sexty, *New algorithms for finite density QCD*, *PoS* **Lattice2015** (2014) 016, [arXiv:1410.8813].
37. **AuroraScience** Collaboration, M. Cristoforetti, F. Di Renzo, and L. Scorzato, *New approach to the sign problem in quantum field theories: High density QCD on a Lefschetz thimble*, *Phys.Rev.* **D86** (2012) 074506, [arXiv:1205.3996].
38. H. Fujii, D. Honda, M. Kato, Y. Kikukawa, S. Komatsu, et al., *Hybrid Monte Carlo on Lefschetz thimbles - A study of the residual sign problem*, *JHEP* **1310** (2013) 147, [arXiv:1309.4371].
39. M. Cristoforetti, F. Di Renzo, G. Eruzzi, A. Mukherjee, C. Schmidt, et al., *An efficient method to compute the residual phase on a Lefschetz thimble*, *Phys.Rev.* **D89** (2014) 114505, [arXiv:1403.5637].
40. R. V. Gavai and S. Gupta, *Pressure and nonlinear susceptibilities in QCD at finite chemical potentials*, *Phys.Rev.* **D68** (2003) 034506, [hep-lat/0303013].
41. C. Allton, S. Ejiri, S. Hands, O. Kaczmarek, F. Karsch, et al., *The Equation of*

state for two flavor QCD at nonzero chemical potential, *Phys.Rev.* **D68** (2003) 014507, [hep-lat/0305007].
42. K. Symanzik, *Continuum Limit and Improved Action in Lattice Theories. 1. Principles and phi**4 Theory*, *Nucl.Phys.* **B226** (1983) 187.
43. K. Symanzik, *Continuum Limit and Improved Action in Lattice Theories. 2. O(N) Nonlinear Sigma Model in Perturbation Theory*, *Nucl.Phys.* **B226** (1983) 205.
44. H. B. Nielsen and M. Ninomiya, *No Go Theorem for Regularizing Chiral Fermions*, *Phys.Lett.* **B105** (1981) 219.
45. J. B. Kogut and L. Susskind, *Hamiltonian Formulation of Wilson's Lattice Gauge Theories*, *Phys.Rev.* **D11** (1975) 395–408.
46. D. B. Kaplan, *A Method for simulating chiral fermions on the lattice*, *Phys.Lett.* **B288** (1992) 342–347, [hep-lat/9206013].
47. Y. Shamir, *Chiral fermions from lattice boundaries*, *Nucl.Phys.* **B406** (1993) 90–106, [hep-lat/9303005].
48. Y. Shamir, *The Euclidean spectrum of Kaplan's lattice chiral fermions*, *Phys.Lett.* **B305** (1993) 357–365, [hep-lat/9212010].
49. V. Furman and Y. Shamir, *Axial symmetries in lattice QCD with Kaplan fermions*, *Nucl.Phys.* **B439** (1995) 54–78, [hep-lat/9405004].
50. H. Neuberger, *More about exactly massless quarks on the lattice*, *Phys.Lett.* **B427** (1998) 353–355, [hep-lat/9801031].
51. H. Neuberger, *Exactly massless quarks on the lattice*, *Phys.Lett.* **B417** (1998) 141–144, [hep-lat/9707022].
52. B. Sheikholeslami and R. Wohlert, *Improved Continuum Limit Lattice Action for QCD with Wilson Fermions*, *Nucl.Phys.* **B259** (1985) 572.
53. E. Follana, Q. Mason, C. Davies, K. Hornbostel, G. P. Lepage, J. Shigemitsu, H. Trottier, and K. Wong, *Highly improved staggered quarks on the lattice with applications to charm physics*, *Phys. Rev. D* **75** (2007) 054502.
54. C. Morningstar and M. J. Peardon, *Analytic smearing of SU(3) link variables in lattice QCD*, *Phys.Rev.* **D69** (2004) 054501, [hep-lat/0311018].
55. U. M. Heller, F. Karsch, and B. Sturm, *Improved staggered fermion actions for QCD thermodynamics*, *Phys.Rev.* **D60** (1999) 114502, [hep-lat/9901010].
56. **RBC, UKQCD** Collaboration, D. J. Antonio et al., *Localization and chiral symmetry in three flavor domain wall QCD*, *Phys.Rev.* **D77** (2008) 014509, [arXiv:0705.2340].
57. D. Renfrew, T. Blum, N. Christ, R. Mawhinney, and P. Vranas, *Controlling Residual Chiral Symmetry Breaking in Domain Wall Fermion Simulations*, *PoS* **LATTICE2008** (2008) 048, [arXiv:0902.2587].
58. P. H. Ginsparg and K. G. Wilson, *A Remnant of Chiral Symmetry on the Lattice*, *Phys.Rev.* **D25** (1982) 2649.
59. M. I. Buchoff, M. Cheng, N. H. Christ, H. T. Ding, C. Jung, et al., *QCD chiral transition, U(1)A symmetry and the dirac spectrum using domain wall fermions*, *Phys.Rev.* **D89** (2014) 054514, [arXiv:1309.4149].
60. G. Cossu, S. Aoki, H. Fukaya, S. Hashimoto, T. Kaneko, et al., *Finite temperature study of the axial U(1) symmetry on the lattice with overlap fermion formulation*, *Phys.Rev.* **D87** (2013) 114514, [arXiv:1304.6145].
61. T. Bhattacharya, M. I. Buchoff, N. H. Christ, H.-T. Ding, R. Gupta, et al., *QCD Phase Transition with Chiral Quarks and Physical Quark Masses*, *Phys.Rev.Lett.* **113** (2014) 082001, [arXiv:1402.5175].
62. V. Dick, F. Karsch, E. Laermann, S. Mukherjee, and S. Sharma, *Microscopic Origin of $U_A(1)$ Symmetry Violation in the High Temperature Phase of QCD*,

arXiv:1502.0619.
63. **WHOT-QCD** Collaboration, H. Saito et al., *Phase structure of finite temperature QCD in the heavy quark region*, *Phys.Rev.* **D84** (2011) 054502, [arXiv:1106.0974].
64. H. Saito, S. Ejiri, S. Aoki, K. Kanaya, Y. Nakagawa, et al., *Histograms in heavy-quark QCD at finite temperature and density*, *Phys.Rev.* **D89** (2014) 034507, [arXiv:1309.2445].
65. F. Karsch, E. Laermann, and C. Schmidt, *The Chiral critical point in three-flavor QCD*, *Phys.Lett.* **B520** (2001) 41–49, [hep-lat/0107020].
66. P. de Forcrand and O. Philipsen, *The Chiral critical line of N(f) = 2+1 QCD at zero and non-zero baryon density*, *JHEP* **0701** (2007) 077, [hep-lat/0607017].
67. G. Endrodi, Z. Fodor, S. Katz, and K. Szabo, *The Nature of the finite temperature QCD transition as a function of the quark masses*, *PoS* **LAT2007** (2007) 182, [arXiv:0710.0998].
68. H.-T. Ding, A. Bazavov, P. Hegde, F. Karsch, S. Mukherjee, et al., *Exploring phase diagram of $N_f = 3$ QCD at $\mu = 0$ with HISQ fermions*, *PoS* **LATTICE2011** (2011) 191, [arXiv:1111.0185].
69. A. Butti, A. Pelissetto, and E. Vicari, *On the nature of the finite temperature transition in QCD*, *JHEP* **0308** (2003) 029, [hep-ph/0307036].
70. A. Pelissetto and E. Vicari, *Relevance of the axial anomaly at the finite-temperature chiral transition in QCD*, *Phys.Rev.* **D88** (2013) 105018, [arXiv:1309.5446].
71. M. Grahl and D. H. Rischke, *Functional renormalization group study of the two-flavor linear sigma model in the presence of the axial anomaly*, *Phys.Rev.* **D88** (2013) 056014, [arXiv:1307.2184].
72. Y. Aoki, G. Endrodi, Z. Fodor, S. Katz, and K. Szabo, *The Order of the quantum chromodynamics transition predicted by the standard model of particle physics*, *Nature* **443** (2006) 675–678, [hep-lat/0611014].
73. E. K. Riedel and F. J. Wegner, *Tricritical exponents and scaling fields*, *Phys. Rev. Lett.* **29** (1972) 349–352.
74. J. Engels, S. Holtmann, T. Mendes, and T. Schulze, *Finite size scaling functions for 3-d O(4) and O(2) spin models and QCD*, *Phys.Lett.* **B514** (2001) 299–308, [hep-lat/0105028].
75. J. Engels, L. Fromme, and M. Seniuch, *Correlation lengths and scaling functions in the three-dimensional O(4) model*, *Nucl.Phys.* **B675** (2003) 533–554, [hep-lat/0307032].
76. S. Ejiri, F. Karsch, E. Laermann, C. Miao, S. Mukherjee, et al., *On the magnetic equation of state in (2+1)-flavor QCD*, *Phys.Rev.* **D80** (2009) 094505, [arXiv:0909.5122].
77. C. Bonati, P. de Forcrand, M. D'Elia, O. Philipsen, and F. Sanfilippo, *Chiral phase transition in two-flavor QCD from an imaginary chemical potential*, *Phys.Rev.* **D90** (2014) 074030, [arXiv:1408.5086].
78. A. Bazavov, T. Bhattacharya, M. Cheng, C. DeTar, H. Ding, et al., *The chiral and deconfinement aspects of the QCD transition*, *Phys.Rev.* **D85** (2012) 054503, [arXiv:1111.1710].
79. Y. Aoki, Z. Fodor, S. Katz, and K. Szabo, *The QCD transition temperature: Results with physical masses in the continuum limit*, *Phys.Lett.* **B643** (2006) 46–54, [hep-lat/0609068].
80. Y. Aoki, S. Borsanyi, S. Durr, Z. Fodor, S. D. Katz, et al., *The QCD transition temperature: results with physical masses in the continuum limit II.*, *JHEP* **0906** (2009) 088, [arXiv:0903.4155].
81. **Wuppertal-Budapest** Collaboration, S. Borsanyi et al., *Is there still any Tc*

mystery in lattice QCD? Results with physical masses in the continuum limit III, *JHEP* **1009** (2010) 073, [arXiv:1005.3508].
82. O. Kaczmarek, F. Karsch, E. Laermann, C. Miao, S. Mukherjee, et al., *Phase boundary for the chiral transition in (2+1) -flavor QCD at small values of the chemical potential*, *Phys.Rev.* **D83** (2011) 014504, [arXiv:1011.3130].
83. G. Endrodi, Z. Fodor, S. Katz, and K. Szabo, *The QCD phase diagram at nonzero quark density*, *JHEP* **1104** (2011) 001, [arXiv:1102.1356].
84. P. Cea, L. Cosmai, and A. Papa, *Critical line of 2+1 flavor QCD*, *Phys.Rev.* **D89** (2014) 074512, [arXiv:1403.0821].
85. C. Bonati, M. D'Elia, M. Mariti, M. Mesiti, F. Negro, et al., *Curvature of the chiral pseudocritical line in QCD*, *Phys.Rev.* **D90** (2014) 114025, [arXiv:1410.5758].
86. A. Andronic, P. Braun-Munzinger, K. Redlich, and J. Stachel, *The thermal model on the verge of the ultimate test: particle production in Pb-Pb collisions at the LHC*, *J.Phys.* **G38** (2011) 124081, [arXiv:1106.6321].
87. Z. Fodor and S. Katz, *Critical point of QCD at finite T and mu, lattice results for physical quark masses*, *JHEP* **0404** (2004) 050, [hep-lat/0402006].
88. S. Datta, R. V. Gavai, and S. Gupta, *QCD at finite chemical potential with $N_t = 8$*, *PoS* **LATTICE2013** (2014) 202.
89. S. Ejiri, *Lee-Yang zero analysis for the study of QCD phase structure*, *Phys.Rev.* **D73** (2006) 054502, [hep-lat/0506023].
90. P. de Forcrand and O. Philipsen, *The QCD phase diagram for small densities from imaginary chemical potential*, *Nucl.Phys.* **B642** (2002) 290–306, [hep-lat/0205016].
91. X.-Y. Jin, Y. Kuramashi, Y. Nakamura, S. Takeda, and A. Ukawa, *Curvature of the critical line on the plane of quark chemical potential and pseudo scalar meson mass for three-flavor QCD*, arXiv:1504.0011.
92. C. Allton, M. Doring, S. Ejiri, S. Hands, O. Kaczmarek, et al., *Thermodynamics of two flavor QCD to sixth order in quark chemical potential*, *Phys.Rev.* **D71** (2005) 054508, [hep-lat/0501030].
93. R. Gavai and S. Gupta, *QCD at finite chemical potential with six time slices*, *Phys.Rev.* **D78** (2008) 114503, [arXiv:0806.2233].
94. O. Kaczmarek, F. Karsch, P. Petreczky, and F. Zantow, *Heavy quark anti-quark free energy and the renormalized Polyakov loop*, *Phys.Lett.* **B543** (2002) 41–47, [hep-lat/0207002].
95. L. D. McLerran and B. Svetitsky, *Quark Liberation at High Temperature: A Monte Carlo Study of SU(2) Gauge Theory*, *Phys.Rev.* **D24** (1981) 450.
96. A. Bazavov and P. Petreczky, *Polyakov loop in 2+1 flavor QCD*, *Phys.Rev.* **D87** (2013) 094505, [arXiv:1301.3943].
97. R. Bellwied, S. Borsanyi, Z. Fodor, S. D. Katz, and C. Ratti, *Is there a flavor hierarchy in the deconfinement transition of QCD?*, *Phys.Rev.Lett.* **111** (2013) 202302, [arXiv:1305.6297].
98. A. Bazavov, H. T. Ding, P. Hegde, O. Kaczmarek, F. Karsch, et al., *Strangeness at high temperatures: from hadrons to quarks*, *Phys.Rev.Lett.* **111** (2013) 082301, [arXiv:1304.7220].
99. V. Koch, A. Majumder, and J. Randrup, *Baryon-strangeness correlations: A Diagnostic of strongly interacting matter*, *Phys.Rev.Lett.* **95** (2005) 182301, [nucl-th/0505052].
100. S. Ejiri, F. Karsch, and K. Redlich, *Hadronic fluctuations at the QCD phase transition*, *Phys.Lett.* **B633** (2006) 275–282, [hep-ph/0509051].
101. S. L. Adler, *Axial vector vertex in spinor electrodynamics*, *Phys.Rev.* **177** (1969) 2426–2438.

102. J. Bell and R. Jackiw, *A PCAC puzzle: pi0 -gt; gamma gamma in the sigma model*, *Nuovo Cim.* **A60** (1969) 47–61.
103. G. 't Hooft, *Symmetry Breaking Through Bell-Jackiw Anomalies*, *Phys.Rev.Lett.* **37** (1976) 8–11.
104. D. J. Gross, R. D. Pisarski, and L. G. Yaffe, *QCD and Instantons at Finite Temperature*, *Rev.Mod.Phys.* **53** (1981) 43.
105. E. V. Shuryak, *Which chiral symmetry is restored in hot QCD?*, *Comments Nucl.Part.Phys.* **21** (1994) 235–248, [hep-ph/9310253].
106. M. Cheng, S. Datta, A. Francis, J. van der Heide, C. Jung, et al., *Meson screening masses from lattice QCD with two light and the strange quark*, *Eur.Phys.J.* **C71** (2011) 1564, [arXiv:1010.1216].
107. S. R. Sharpe, *Rooted staggered fermions: Good, bad or ugly?*, *PoS* **LAT2006** (2006) 022, [hep-lat/0610094].
108. G. C. Donald, C. T. Davies, E. Follana, and A. S. Kronfeld, *Staggered fermions, zero modes, and flavor-singlet mesons*, *Phys.Rev.* **D84** (2011) 054504, [arXiv:1106.2412].
109. **HotQCD** Collaboration, A. Bazavov et al., *The chiral transition and $U(1)_A$ symmetry restoration from lattice QCD using Domain Wall Fermions*, *Phys.Rev.* **D86** (2012) 094503, [arXiv:1205.3535].
110. A. Tomiya, G. Cossu, H. Fukaya, S. Hashimoto, and J. Noaki, *Effects of near-zero Dirac eigenmodes on axial U(1) symmetry at finite temperature*, arXiv:1412.7306.
111. **TWQCD** Collaboration, T.-W. Chiu, W.-P. Chen, Y.-C. Chen, H.-Y. Chou, and T.-H. Hsieh, *Chiral symmetry and axial U(1) symmetry in finite temperature QCD with domain-wall fermion*, *PoS* **LATTICE2013** (2014) 165, [arXiv:1311.6220].
112. F. Karsch, *Lattice QCD at high temperature and density*, *Lect.Notes Phys.* **583** (2002) 209–249, [hep-lat/0106019].
113. S. Borsanyi, Z. Fodor, C. Hoelbling, S. D. Katz, S. Krieg, et al., *Full result for the QCD equation of state with 2+1 flavors*, *Phys.Lett.* **B730** (2014) 99–104, [arXiv:1309.5258].
114. **HotQCD** Collaboration, A. Bazavov et al., *Equation of state in (2+1)-flavor QCD*, *Phys.Rev.* **D90** (2014) 094503, [arXiv:1407.6387].
115. A. Majumder and B. Muller, *Hadron Mass Spectrum from Lattice QCD*, *Phys.Rev.Lett.* **105** (2010) 252002, [arXiv:1008.1747].
116. A. Bazavov, H. T. Ding, P. Hegde, O. Kaczmarek, F. Karsch, et al., *Additional Strange Hadrons from QCD Thermodynamics and Strangeness Freezeout in Heavy Ion Collisions*, *Phys.Rev.Lett.* **113** (2014) 072001, [arXiv:1404.6511].
117. R. V. Gavai and S. Gupta, *Quark number susceptibilities, strangeness and dynamical confinement*, *Phys.Rev.* **D64** (2001) 074506, [hep-lat/0103013].
118. C. Allton, S. Ejiri, S. Hands, O. Kaczmarek, F. Karsch, et al., *The QCD thermal phase transition in the presence of a small chemical potential*, *Phys.Rev.* **D66** (2002) 074507, [hep-lat/0204010].
119. S. Ejiri, F. Karsch, E. Laermann, and C. Schmidt, *The Isentropic equation of state of 2-flavor QCD*, *Phys.Rev.* **D73** (2006) 054506, [hep-lat/0512040].
120. S. Borsanyi, Z. Fodor, S. D. Katz, S. Krieg, C. Ratti, et al., *Fluctuations of conserved charges at finite temperature from lattice QCD*, *JHEP* **1201** (2012) 138, [arXiv:1112.4416].
121. **HotQCD** Collaboration, A. Bazavov et al., *Fluctuations and Correlations of net baryon number, electric charge, and strangeness: A comparison of lattice QCD results with the hadron resonance gas model*, *Phys.Rev.* **D86** (2012) 034509, [arXiv:1203.0784].

122. S. Borsanyi, G. Endrodi, Z. Fodor, S. Katz, S. Krieg, et al., *QCD equation of state at nonzero chemical potential: continuum results with physical quark masses at order mu^2*, *JHEP* **1208** (2012) 053, [arXiv:1204.6710].
123. S. Borsanyi, Z. Fodor, S. Katz, S. Krieg, C. Ratti, et al., *Freeze-out parameters: lattice meets experiment*, *Phys.Rev.Lett.* **111** (2013) 062005, [arXiv:1305.5161].
124. **for the BNL-Bielefeld-CCNU** Collaboration, P. Hegde, *The QCD equation of state to $\mathcal{O}(\mu_B^4)$*, arXiv:1412.6727.
125. M. Laine and Y. Schroder, *Quark mass thresholds in QCD thermodynamics*, *Phys.Rev.* **D73** (2006) 085009, [hep-ph/0603048].
126. M. Stephanov, *Non-Gaussian fluctuations near the QCD critical point*, *Phys.Rev.Lett.* **102** (2009) 032301, [arXiv:0809.3450].
127. M. Asakawa, S. Ejiri, and M. Kitazawa, *Third moments of conserved charges as probes of QCD phase structure*, *Phys.Rev.Lett.* **103** (2009) 262301, [arXiv:0904.2089].
128. B. Friman, F. Karsch, K. Redlich, and V. Skokov, *Fluctuations as probe of the QCD phase transition and freeze-out in heavy ion collisions at LHC and RHIC*, *Eur.Phys.J.* **C71** (2011) 1694, [arXiv:1103.3511].
129. M. Stephanov, *On the sign of kurtosis near the QCD critical point*, *Phys.Rev.Lett.* **107** (2011) 052301, [arXiv:1104.1627].
130. M. A. Stephanov, K. Rajagopal, and E. V. Shuryak, *Signatures of the tricritical point in QCD*, *Phys.Rev.Lett.* **81** (1998) 4816–4819, [hep-ph/9806219].
131. M. A. Stephanov, K. Rajagopal, and E. V. Shuryak, *Event-by-event fluctuations in heavy ion collisions and the QCD critical point*, *Phys.Rev.* **D60** (1999) 114028, [hep-ph/9903292].
132. S. Jeon and V. Koch, *Event by event fluctuations*, hep-ph/0304012.
133. Y. Hatta and M. Stephanov, *Proton number fluctuation as a signal of the QCD critical endpoint*, *Phys.Rev.Lett.* **91** (2003) 102003, [hep-ph/0302002].
134. C. Athanasiou, K. Rajagopal, and M. Stephanov, *Using Higher Moments of Fluctuations and their Ratios in the Search for the QCD Critical Point*, *Phys.Rev.* **D82** (2010) 074008, [arXiv:1006.4636].
135. *Studying the phase diagram of qcd matter at rhic*, 2014. https://drupal.star.bnl.gov/STAR/files/BES_WPII_ver6.9_Cover.pdf.
136. **STAR** Collaboration, M. Aggarwal et al., *Higher Moments of Net-proton Multiplicity Distributions at RHIC*, *Phys.Rev.Lett.* **105** (2010) 022302, [arXiv:1004.4959].
137. **STAR** Collaboration, L. Adamczyk et al., *Energy Dependence of Moments of Net-proton Multiplicity Distributions at RHIC*, *Phys.Rev.Lett.* **112** (2014) 032302, [arXiv:1309.5681].
138. **STAR** Collaboration, L. Adamczyk et al., *Beam energy dependence of moments of the net-charge multiplicity distributions in Au+Au collisions at RHIC*, *Phys.Rev.Lett.* **113** (2014) 092301, [arXiv:1402.1558].
139. **STAR** Collaboration, N. R. Sahoo, *Recent results on event-by-event fluctuations from the RHIC Beam Energy Scan program in the STAR experiment*, *J.Phys.Conf.Ser.* **535** (2014) 012007, [arXiv:1407.1554].
140. **STAR** Collaboration, X. Luo, *Energy Dependence of Moments of Net-Proton and Net-Charge Multiplicity Distributions at STAR*, *PoS* **CPOD2014** (2014) 019, [arXiv:1503.0255].
141. **PHENIX** Collaboration, J. T. Mitchell, *The RHIC Beam Energy Scan Program: Results from the PHENIX Experiment*, *Nucl.Phys.* **A904-905** (2013) 903c–906c, [arXiv:1211.6139].

142. A. Bazavov, H. Ding, P. Hegde, O. Kaczmarek, F. Karsch, et al., *Freeze-out Conditions in Heavy Ion Collisions from QCD Thermodynamics*, *Phys.Rev.Lett.* **109** (2012) 192302, [arXiv:1208.1220].
143. M. Kitazawa and M. Asakawa, *Relation between baryon number fluctuations and experimentally observed proton number fluctuations in relativistic heavy ion collisions*, *Phys.Rev.* **C86** (2012) 024904, [arXiv:1205.3292].
144. A. Bzdak and V. Koch, *Acceptance corrections to net baryon and net charge cumulants*, *Phys.Rev.* **C86** (2012) 044904, [arXiv:1206.4286].
145. A. Bzdak and V. Koch, *Local Efficiency Corrections to Higher Order Cumulants*, *Phys.Rev.* **C91** (2015) 027901, [arXiv:1312.4574].
146. F. Karsch, *Determination of Freeze-out Conditions from Lattice QCD Calculations*, *Central Eur.J.Phys.* **10** (2012) 1234–1237, [arXiv:1202.4173].
147. S. Mukherjee and M. Wagner, *Deconfinement of strangeness and freeze-out from charge fluctuations*, *PoS* **CPOD2013** (2013) 039, [arXiv:1307.6255].
148. S. Borsanyi, Z. Fodor, S. Katz, S. Krieg, C. Ratti, et al., *Freeze-out parameters from electric charge and baryon number fluctuations: is there consistency?*, *Phys.Rev.Lett.* **113** (2014) 052301, [arXiv:1403.4576].
149. S. Mukherjee, *"freeze-out condition from lattice qcd and the role of additional strange hadrons"*, *PoS* **CPOD2014** (2014) 005.
150. S. Capstick and N. Isgur, *Baryons in a Relativized Quark Model with Chromodynamics*, *Phys.Rev.* **D34** (1986) 2809.
151. D. Ebert, R. Faustov, and V. Galkin, *Mass spectra and Regge trajectories of light mesons in the relativistic quark model*, *Phys.Rev.* **D79** (2009) 114029, [arXiv:0903.5183].
152. A. Bazavov, H.-T. Ding, P. Hegde, O. Kaczmarek, F. Karsch, et al., *The melting and abundance of open charm hadrons*, *Phys.Lett.* **B737** (2014) 210–215, [arXiv:1404.4043].
153. M. Asakawa, T. Hatsuda, and Y. Nakahara, *Maximum entropy analysis of the spectral functions in lattice QCD*, *Prog.Part.Nucl.Phys.* **46** (2001) 459–508, [hep-lat/0011040].
154. R. Rapp and H. van Hees, *Heavy Quark Diffusion as a Probe of the Quark-Gluon Plasma*, arXiv:0803.0901.
155. H.-T. Ding, *Hard and thermal probes of QGP from the perspective of Lattice QCD*, arXiv:1404.5134.
156. H. B. Meyer, *Transport Properties of the Quark-Gluon Plasma: A Lattice QCD Perspective*, *Eur.Phys.J.* **A47** (2011) 86, [arXiv:1104.3708].
157. F. Karsch, E. Laermann, P. Petreczky, S. Stickan, and I. Wetzorke, *A Lattice calculation of thermal dilepton rates*, *Phys.Lett.* **B530** (2002) 147–152, [hep-lat/0110208].
158. Y. Nakahara, M. Asakawa, and T. Hatsuda, *Hadronic spectral functions in lattice QCD*, *Phys.Rev.* **D60** (1999) 091503, [hep-lat/9905034].
159. G. Aarts, C. Allton, J. Foley, S. Hands, and S. Kim, *Spectral functions at small energies and the electrical conductivity in hot, quenched lattice QCD*, *Phys.Rev.Lett.* **99** (2007) 022002, [hep-lat/0703008].
160. H.-T. Ding, A. Francis, O. Kaczmarek, F. Karsch, E. Laermann, et al., *Thermal dilepton rate and electrical conductivity: An analysis of vector current correlation functions in quenched lattice QCD*, *Phys.Rev.* **D83** (2011) 034504, [arXiv:1012.4963].
161. O. Kaczmarek, E. Laermann, M. Müller, F. Karsch, H. Ding, et al., *Thermal dilepton rates from quenched lattice QCD*, *PoS* **ConfinementX** (2012) 185,

[arXiv:1301.7436].
162. O. Kaczmarek and M. Müller, *Temperature dependence of electrical conductivity and dilepton rates from hot quenched lattice QCD*, *PoS* **LATTICE2013** (2014) 175, [arXiv:1312.5609].
163. H.-T. Ding, O. Kaczmarek, and F. Meyer, *Vector spectral functions and transport properties in quenched QCD*, arXiv:1412.5869.
164. S. Gupta, *The Electrical conductivity and soft photon emissivity of the QCD plasma*, *Phys.Lett.* **B597** (2004) 57–62, [hep-lat/0301006].
165. B. B. Brandt, A. Francis, H. B. Meyer, and H. Wittig, *Thermal Correlators in the ρ channel of two-flavor QCD*, *JHEP* **1303** (2013) 100, [arXiv:1212.4200].
166. G. Aarts, C. Allton, A. Amato, P. Giudice, S. Hands, et al., *Electrical conductivity and charge diffusion in thermal QCD from the lattice*, arXiv:1412.6411.
167. A. Amato, G. Aarts, C. Allton, P. Giudice, S. Hands, et al., *Electrical conductivity of the quark-gluon plasma across the deconfinement transition*, *Phys.Rev.Lett.* **111** (2013) 172001, [arXiv:1307.6763].
168. D. Fernandez-Fraile and A. Gomez Nicola, *The Electrical conductivity of a pion gas*, *Phys.Rev.* **D73** (2006) 045025, [hep-ph/0512283].
169. **PHENIX** Collaboration, A. Adare et al., *Energy Loss and Flow of Heavy Quarks in Au+Au Collisions at s(NN)**(1/2) = 200-GeV*, *Phys.Rev.Lett.* **98** (2007) 172301, [nucl-ex/0611018].
170. **STAR** Collaboration, B. Abelev et al., *Erratum: Transverse momentum and centrality dependence of high-p_T non-photonic electron suppression in Au+Au collisions at $\sqrt{s_{NN}} = 200$ GeV*, *Phys.Rev.Lett.* **98** (2007) 192301, [nucl-ex/0607012].
171. **ALICE** Collaboration, B. Abelev et al., *Suppression of high transverse momentum D mesons in central Pb-Pb collisions at $\sqrt{s_{NN}} = 2.76$ TeV*, *JHEP* **1209** (2012) 112, [arXiv:1203.2160].
172. M. He, R. J. Fries, and R. Rapp, *Modifications of Heavy-Flavor Spectra in $\sqrt{s_{\rm NN}} = 62.4$ GeV Au-Au Collisions*, arXiv:1409.4539.
173. S. Cao, Y. Huang, G.-Y. Qin, and S. A. Bass, *The Influence of Initial State Fluctuations on Heavy Quark Energy Loss in Relativistic Heavy-ion Collisions*, arXiv:1404.3139.
174. H. Ding, A. Francis, O. Kaczmarek, F. Karsch, H. Satz, et al., *Heavy Quark diffusion from lattice QCD spectral functions*, *J.Phys.* **G38** (2011) 124070, [arXiv:1107.0311].
175. S. Caron-Huot and G. D. Moore, *Heavy quark diffusion in perturbative QCD at next-to-leading order*, *Phys.Rev.Lett.* **100** (2008) 052301, [arXiv:0708.4232].
176. P. Kovtun, D. T. Son, and A. O. Starinets, *Holography and hydrodynamics: Diffusion on stretched horizons*, *JHEP* **0310** (2003) 064, [hep-th/0309213].
177. O. Kaczmarek, *Continuum estimate of the heavy quark momentum diffusion coefficient κ*, arXiv:1409.3724.
178. D. Banerjee, S. Datta, R. Gavai, and P. Majumdar, *Heavy Quark Momentum Diffusion Coefficient from Lattice QCD*, *Phys.Rev.* **D85** (2012) 014510, [arXiv:1109.5738].
179. S. Caron-Huot, M. Laine, and G. D. Moore, *A Way to estimate the heavy quark thermalization rate from the lattice*, *JHEP* **0904** (2009) 053, [arXiv:0901.1195].
180. J. Casalderrey-Solana and D. Teaney, *Heavy quark diffusion in strongly coupled N=4 Yang-Mills*, *Phys.Rev.* **D74** (2006) 085012, [hep-ph/0605199].
181. H. B. Meyer, *A Calculation of the shear viscosity in SU(3) gluodynamics*, *Phys.Rev.* **D76** (2007) 101701, [arXiv:0704.1801].

182. M. Luscher and P. Weisz, *Locality and exponential error reduction in numerical lattice gauge theory*, *JHEP* **0109** (2001) 010, [hep-lat/0108014].
183. G. Parisi, R. Petronzio, and F. Rapuano, *A Measurement of the String Tension Near the Continuum Limit*, *Phys.Lett.* **B128** (1983) 418.
184. P. De Forcrand and C. Roiesnel, *REFINED METHODS FOR MEASURING LARGE DISTANCE CORRELATIONS*, *Phys.Lett.* **B151** (1985) 77–80.
185. G. D. Moore and D. Teaney, *How much do heavy quarks thermalize in a heavy ion collision?*, *Phys.Rev.* **C71** (2005) 064904, [hep-ph/0412346].
186. F. Karsch and H. Wyld, *Thermal Green's Functions and Transport Coefficients on the Lattice*, *Phys.Rev.* **D35** (1987) 2518.
187. H. B. Meyer, *The Yang-Mills spectrum from a two level algorithm*, *JHEP* **0401** (2004) 030, [hep-lat/0312034].
188. A. Nakamura and S. Sakai, *Transport coefficients of gluon plasma*, *Phys.Rev.Lett.* **94** (2005) 072305, [hep-lat/0406009].
189. H. B. Meyer, *A Calculation of the bulk viscosity in SU(3) gluodynamics*, *Phys.Rev.Lett.* **100** (2008) 162001, [arXiv:0710.3717].
190. F. Karsch, D. Kharzeev, and K. Tuchin, *Universal properties of bulk viscosity near the QCD phase transition*, *Phys.Lett.* **B663** (2008) 217–221, [arXiv:0711.0914].
191. D. Kharzeev and K. Tuchin, *Bulk viscosity of QCD matter near the critical temperature*, *JHEP* **0809** (2008) 093, [arXiv:0705.4280].
192. P. Romatschke and D. T. Son, *Spectral sum rules for the quark-gluon plasma*, *Phys.Rev.* **D80** (2009) 065021, [arXiv:0903.3946].
193. P. Romatschke, *Relativistic Viscous Fluid Dynamics and Non-Equilibrium Entropy*, *Class.Quant.Grav.* **27** (2010) 025006, [arXiv:0906.4787].
194. G. D. Moore and K. A. Sohrabi, *Kubo Formulae for Second-Order Hydrodynamic Coefficients*, *Phys.Rev.Lett.* **106** (2011) 122302, [arXiv:1007.5333].
195. G. D. Moore and K. A. Sohrabi, *Thermodynamical second-order hydrodynamic coefficients*, *JHEP* **1211** (2012) 148, [arXiv:1210.3340].
196. G. Denicol, H. Niemi, E. Molnar, and D. Rischke, *Derivation of transient relativistic fluid dynamics from the Boltzmann equation*, *Phys.Rev.* **D85** (2012) 114047, [arXiv:1202.4551].
197. R. Baier, P. Romatschke, D. T. Son, A. O. Starinets, and M. A. Stephanov, *Relativistic viscous hydrodynamics, conformal invariance, and holography*, *JHEP* **0804** (2008) 100, [arXiv:0712.2451].
198. Y. Kohno, M. Asakawa, and M. Kitazawa, *Shear viscosity to relaxation time ratio in SU(3) lattice gauge theory*, *Phys.Rev.* **D89** (2014) 054508, [arXiv:1112.1508].
199. O. Philipsen and C. Schäfer, *The second order hydrodynamic transport coefficient κ for the gluon plasma from the lattice*, *JHEP* **1402** (2014) 003, [arXiv:1311.6618].
200. P. Romatschke, *New Developments in Relativistic Viscous Hydrodynamics*, *Int.J.Mod.Phys.* **E19** (2010) 1–53, [arXiv:0902.3663].
201. A. Adil and I. Vitev, *Collisional dissociation of heavy mesons in dense QCD matter*, *Phys.Lett.* **B649** (2007) 139–146, [hep-ph/0611109].
202. R. Sharma, I. Vitev, and B.-W. Zhang, *Light-cone wave function approach to open heavy flavor dynamics in QCD matter*, *Phys.Rev.* **C80** (2009) 054902, [arXiv:0904.0032].
203. M. He, R. J. Fries, and R. Rapp, *Heavy-Quark Diffusion and Hadronization in Quark-Gluon Plasma*, *Phys.Rev.* **C86** (2012) 014903, [arXiv:1106.6006].
204. D. Ebert, R. Faustov, and V. Galkin, *Heavy-light meson spectroscopy and Regge trajectories in the relativistic quark model*, *Eur.Phys.J.* **C66** (2010) 197–206, [arXiv:0910.5612].

205. D. Ebert, R. Faustov, and V. Galkin, *Spectroscopy and Regge trajectories of heavy baryons in the relativistic quark-diquark picture*, *Phys.Rev.* **D84** (2011) 014025, [arXiv:1105.0583].
206. A. Mocsy, P. Petreczky, and M. Strickland, *Quarkonia in the Quark Gluon Plasma*, *Int.J.Mod.Phys.* **A28** (2013) 1340012, [arXiv:1302.2180].
207. A. Bazavov, P. Petreczky, and A. Velytsky, *Quarkonium at Finite Temperature*, arXiv:0904.1748.
208. N. Brambilla, S. Eidelman, B. Heltsley, R. Vogt, G. Bodwin, et al., *Heavy quarkonium: progress, puzzles, and opportunities*, *Eur.Phys.J.* **C71** (2011) 1534, [arXiv:1010.5827].
209. E. Eichten, K. Gottfried, T. Kinoshita, K. Lane, and T.-M. Yan, *Charmonium: The Model*, *Phys.Rev.* **D17** (1978) 3090.
210. E. Eichten, K. Gottfried, T. Kinoshita, K. Lane, and T.-M. Yan, *Charmonium: Comparison with Experiment*, *Phys.Rev.* **D21** (1980) 203.
211. A. Mocsy, *Potential Models for Quarkonia*, *Eur.Phys.J.* **C61** (2009) 705–710, [arXiv:0811.0337].
212. M. Laine, O. Philipsen, P. Romatschke, and M. Tassler, *Real-time static potential in hot QCD*, *JHEP* **0703** (2007) 054, [hep-ph/0611300].
213. A. Beraudo, J.-P. Blaizot, and C. Ratti, *Real and imaginary-time Q anti-Q correlators in a thermal medium*, *Nucl.Phys.* **A806** (2008) 312–338, [arXiv:0712.4394].
214. N. Brambilla, J. Ghiglieri, A. Vairo, and P. Petreczky, *Static quark-antiquark pairs at finite temperature*, *Phys.Rev.* **D78** (2008) 014017, [arXiv:0804.0993].
215. W. Caswell and G. Lepage, *Effective Lagrangians for Bound State Problems in QED, QCD, and Other Field Theories*, *Phys.Lett.* **B167** (1986) 437.
216. G. T. Bodwin, E. Braaten, and G. P. Lepage, *Rigorous QCD analysis of inclusive annihilation and production of heavy quarkonium*, *Phys.Rev.* **D51** (1995) 1125–1171, [hep-ph/9407339].
217. N. Brambilla, A. Pineda, J. Soto, and A. Vairo, *Potential NRQCD: An Effective theory for heavy quarkonium*, *Nucl.Phys.* **B566** (2000) 275, [hep-ph/9907240].
218. A. Rothkopf, T. Hatsuda, and S. Sasaki, *Complex Heavy-Quark Potential at Finite Temperature from Lattice QCD*, *Phys.Rev.Lett.* **108** (2012) 162001, [arXiv:1108.1579].
219. Y. Burnier and A. Rothkopf, *Disentangling the timescales behind the non-perturbative heavy quark potential*, *Phys.Rev.* **D86** (2012) 051503, [arXiv:1208.1899].
220. Y. Burnier and A. Rothkopf, *A hard thermal loop benchmark for the extraction of the nonperturbative $Q\bar{Q}$ potential*, *Phys.Rev.* **D87** (2013) 114019, [arXiv:1304.4154].
221. Y. Burnier, O. Kaczmarek, and A. Rothkopf, *Static quark-antiquark potential in the quark-gluon plasma from lattice QCD*, arXiv:1410.2546.
222. S. Nadkarni, *Nonabelian Debye Screening. 2. The Singlet Potential*, *Phys.Rev.* **D34** (1986) 3904.
223. A. Bazavov, Y. Burnier, and P. Petreczky, *Lattice calculation of the heavy quark potential at non-zero temperature*, arXiv:1404.4267.
224. A. Rothkopf, *Improved Maximum Entropy Analysis with an Extended Search Space*, *J.Comput.Phys.* **238** (2013) 106–114, [arXiv:1110.6285].
225. A. Rothkopf, *Improved Maximum Entropy Method with an Extended Search Space*, *PoS* **LATTICE2012** (2012) 100, [arXiv:1208.5162].
226. Y. Burnier and A. Rothkopf, *Bayesian Approach to Spectral Function*

Reconstruction for Euclidean Quantum Field Theories, *Phys.Rev.Lett.* **111** (2013) 182003, [arXiv:1307.6106].
227. H. Ding, A. Francis, O. Kaczmarek, F. Karsch, H. Satz, et al., *Charmonium properties in hot quenched lattice QCD*, *Phys.Rev.* **D86** (2012) 014509, [arXiv:1204.4945].
228. M. Asakawa and T. Hatsuda, *J / psi and eta(c) in the deconfined plasma from lattice QCD*, *Phys.Rev.Lett.* **92** (2004) 012001, [hep-lat/0308034].
229. S. Datta, F. Karsch, P. Petreczky, and I. Wetzorke, *Behavior of charmonium systems after deconfinement*, *Phys.Rev.* **D69** (2004) 094507, [hep-lat/0312037].
230. A. Jakovac, P. Petreczky, K. Petrov, and A. Velytsky, *Quarkonium correlators and spectral functions at zero and finite temperature*, *Phys.Rev.* **D75** (2007) 014506, [hep-lat/0611017].
231. H. Iida, T. Doi, N. Ishii, H. Suganuma, and K. Tsumura, *Charmonium properties in deconfinement phase in anisotropic lattice QCD*, *Phys.Rev.* **D74** (2006) 074502, [hep-lat/0602008].
232. **WHOT-QCD** Collaboration, H. Ohno et al., *Charmonium spectral functions with the variational method in zero and finite temperature lattice QCD*, *Phys.Rev.* **D84** (2011) 094504, [arXiv:1104.3384].
233. G. Aarts, C. Allton, M. B. Oktay, M. Peardon, and J.-I. Skullerud, *Charmonium at high temperature in two-flavor QCD*, *Phys.Rev.* **D76** (2007) 094513, [arXiv:0705.2198].
234. S. Borsanyi, S. Dürr, Z. Fodor, C. Hoelbling, S. D. Katz, et al., *Charmonium spectral functions from 2+1 flavour lattice QCD*, *JHEP* **1404** (2014) 132, [arXiv:1401.5940].
235. G. Aarts, C. Allton, T. Harris, S. Kim, M. P. Lombardo, et al., *The bottomonium spectrum at finite temperature from $N_f = 2 + 1$ lattice QCD*, *JHEP* **1407** (2014) 097, [arXiv:1402.6210].
236. H. Ohno, H. T. Ding, and O. Kaczmarek, *Quark mass dependence of quarkonium properties at finite temperature*, arXiv:1412.6594.
237. B. Thacker and G. P. Lepage, *Heavy quark bound states in lattice QCD*, *Phys.Rev.* **D43** (1991) 196–208.
238. G. P. Lepage, L. Magnea, C. Nakhleh, U. Magnea, and K. Hornbostel, *Improved nonrelativistic QCD for heavy quark physics*, *Phys.Rev.* **D46** (1992) 4052–4067, [hep-lat/9205007].
239. G. Aarts, S. Kim, M. Lombardo, M. Oktay, S. Ryan, et al., *Bottomonium above deconfinement in lattice nonrelativistic QCD*, *Phys.Rev.Lett.* **106** (2011) 061602, [arXiv:1010.3725].
240. G. Aarts, C. Allton, S. Kim, M. Lombardo, S. Ryan, et al., *Melting of P wave bottomonium states in the quark-gluon plasma from lattice NRQCD*, *JHEP* **1312** (2013) 064, [arXiv:1310.5467].
241. G. Aarts, C. Allton, S. Kim, M. P. Lombardo, M. B. Oktay, et al., *S wave bottomonium states moving in a quark-gluon plasma from lattice NRQCD*, *JHEP* **1303** (2013) 084, [arXiv:1210.2903].
242. G. Aarts, C. Allton, S. Kim, M. Lombardo, M. Oktay, et al., *What happens to the Υ and η_b in the quark-gluon plasma? Bottomonium spectral functions from lattice QCD*, *JHEP* **1111** (2011) 103, [arXiv:1109.4496].
243. S. Kim, P. Petreczky, and A. Rothkopf, *Lattice NRQCD study of S- and P-wave bottomonium states in a thermal medium with $N_f = 2 + 1$ light flavors*, arXiv:1409.3630.
244. W. Florkowski and B. L. Friman, *Spatial dependence of the finite temperature*

meson correlation function, *Z.Phys.* **A347** (1994) 271–276.
245. A. Bazavov, F. Karsch, Y. Maezawa, S. Mukherjee, and P. Petreczky, *In-medium modifications of open and hidden strange-charm mesons from spatial correlation functions*, arXiv:1411.3018.
246. F. Karsch, E. Laermann, S. Mukherjee, and P. Petreczky, *Signatures of charmonium modification in spatial correlation functions*, *Phys.Rev.* **D85** (2012) 114501, [arXiv:1203.3770].
247. M. D'Elia, *Lattice QCD Simulations in External Background Fields*, *Lect.Notes Phys.* (2013) [arXiv:1209.0374].
248. A. Yamamoto, *Chiral Magnetic Effect on the Lattice*, *Lect.Notes Phys.* **871** (2013) 387–397, [arXiv:1207.0375].
249. G. Endrodi, *QCD in magnetic fields: from Hofstadter's butterfly to the phase diagram*, arXiv:1410.8028.
250. M. D'Elia, *Lattice QCD with purely imaginary sources at zero and non-zero temperature*, arXiv:1502.0604.
251. M. D'Elia, S. Mukherjee, and F. Sanfilippo, *QCD Phase Transition in a Strong Magnetic Background*, *Phys.Rev.* **D82** (2010) 051501, [arXiv:1005.5365].
252. E.-M. Ilgenfritz, M. Kalinowski, M. Muller-Preussker, B. Petersson, and A. Schreiber, *Two-color QCD with staggered fermions at finite temperature under the influence of a magnetic field*, *Phys.Rev.* **D85** (2012) 114504, [arXiv:1203.3360].
253. G. Bali, F. Bruckmann, G. Endrodi, Z. Fodor, S. Katz, et al., *The QCD phase diagram for external magnetic fields*, *JHEP* **1202** (2012) 044, [arXiv:1111.4956].
254. V. Bornyakov, P. Buividovich, N. Cundy, O. Kochetkov, and A. Schäfer, *Deconfinement transition in two-flavor lattice QCD with dynamical overlap fermions in an external magnetic field*, *Phys.Rev.* **D90** (2014) 034501, [arXiv:1312.5628].
255. E. M. Ilgenfritz, M. Muller-Preussker, B. Petersson, and A. Schreiber, *Magnetic catalysis (and inverse catalysis) at finite temperature in two-color lattice QCD*, *Phys.Rev.* **D89** (2014) 054512, [arXiv:1310.7876].
256. M. D'Elia and F. Negro, *Chiral Properties of Strong Interactions in a Magnetic Background*, *Phys.Rev.* **D83** (2011) 114028, [arXiv:1103.2080].
257. G. Bali, F. Bruckmann, G. Endrodi, Z. Fodor, S. Katz, et al., *QCD quark condensate in external magnetic fields*, *Phys.Rev.* **D86** (2012) 071502, [arXiv:1206.4205].
258. G. Bali, F. Bruckmann, G. Endrődi, S. Katz, and A. Schäfer, *The QCD equation of state in background magnetic fields*, *JHEP* **1408** (2014) 177, [arXiv:1406.0269].
259. C. Bonati, M. D'Elia, M. Mariti, F. Negro, and F. Sanfilippo, *Magnetic Susceptibility of Strongly Interacting Matter across the Deconfinement Transition*, *Phys.Rev.Lett.* **111** (2013) 182001, [arXiv:1307.8063].
260. C. Bonati, M. D'Elia, M. Mariti, F. Negro, and F. Sanfilippo, *Magnetic susceptibility and equation of state of $N_f = 2 + 1$ QCD with physical quark masses*, *Phys.Rev.* **D89** (2014) 054506, [arXiv:1310.8656].
261. G. Bali, F. Bruckmann, G. Endrodi, F. Gruber, and A. Schaefer, *Magnetic field-induced gluonic (inverse) catalysis and pressure (an)isotropy in QCD*, *JHEP* **1304** (2013) 130, [arXiv:1303.1328].
262. G. Bali, F. Bruckmann, G. Endrodi, and A. Schafer, *Paramagnetic squeezing of QCD matter*, *Phys.Rev.Lett.* **112** (2014) 042301, [arXiv:1311.2559].
263. L. Levkova and C. DeTar, *Quark-gluon plasma in an external magnetic field*, *Phys.Rev.Lett.* **112** (2014) 012002, [arXiv:1309.1142].
264. G. Endrődi, *QCD equation of state at nonzero magnetic fields in the Hadron Resonance Gas model*, *JHEP* **1304** (2013) 023, [arXiv:1301.1307].

265. M. Abramczyk, T. Blum, G. Petropoulos, and R. Zhou, *Chiral magnetic effect in 2+1 flavor QCD+QED*, *PoS* **LAT2009** (2009) 181, [arXiv:0911.1348].
266. P. Buividovich, M. Chernodub, E. Luschevskaya, and M. Polikarpov, *Numerical evidence of chiral magnetic effect in lattice gauge theory*, *Phys.Rev.* **D80** (2009) 054503, [arXiv:0907.0494].
267. G. Bali, F. Bruckmann, G. Endrődi, Z. Fodor, S. Katz, et al., *Local CP-violation and electric charge separation by magnetic fields from lattice QCD*, *JHEP* **1404** (2014) 129, [arXiv:1401.4141].